Master's thesis

NTNU
Norwegian University of Science and Technology
Faculty of Engineering
Department of Marine Technology

Vegard Njøten Fagerbakke

Enabling intelligent multi-modular concept for solar energy harvest by local control of connectors.

Master's thesis in Marine Technology
Supervisor: Professor Dong Trong Nguyen
Co-supervisor: Trine Aas-Hansen
June 2023

NTNU
Norwegian University of
Science and Technology

Vegard Njøten Fagerbakke

Enabling intelligent multi-modular concept for solar energy harvest by local control of connectors.

Master's thesis in Marine Technology
Supervisor: Professor Dong Trong Nguyen
Co-supervisor: Trine Aas-Hansen
June 2023

Norwegian University of Science and Technology
Faculty of Engineering
Department of Marine Technology

NTNU
Norwegian University of
Science and Technology

NTNU
Kunnskap for en bedre verden

Department of Marine Technology

TMR4930 - Marine Technology, Master Thesis

Enabling intelligent multi-modular concept for solar energy harvest by local control of connectors.

Author:
Vegard Njøten Fagerbakke

NTNU Trondheim
Norwegian University of Science and Technology
Department of Marine Technology

MASTER OF TECHNOLOGY THESIS DEFINITION (30 SP)

Name of the candidate: Vegard Njøten Fagerbakke
Field of study: Marine Cybernetics
Thesis title (Norwegian): Muliggjør intelligent multi-modulært konsept for høsting av solenergi ved lokal kontroll av hengsler.
Thesis title (English): Enabling intelligent multi-modular concept for solar energy harvest by local control of connectors.

Background

There is a need for alternative energy sources which are sustainable, accessible, and affordable to the entire world's population. Solar has become one of the cheapest renewable energies in the world and will play an important role in the energy transition in the next thirty years. The focus of this thesis will limit the scope to the solar energy harvest using a multi-modular concept as a cost-effective platform. Two main concerns are high internal loads in the connections / joints and large relative motion between connected modules. The objective of this thesis is to investigate the feasibility of employing adaptive connectors within the multi-modular concept to mitigate excessive module motion and reduce load on the connectors. This investigation will be accomplished through simulation studies and subsequent model-scaled experiments conducted at Lilletanken. The outcomes of this research will serve as an initial step towards developing a control strategy for intelligent multi-modular structures, with the ultimate aim of optimizing their performance and efficiency.

Work description

1. Perform a background and literature review to provide information and relevant references on:
    a. Multi-modular floating structures
    b. Simulation methods
    c. Connections between modules: types, application, control aspect
    d. Report the results of the literature review conducted during Fall 2022 into the master thesis document.
2. Write a list with abbreviations and definitions of terms and symbols, relevant to the literature study and project report.
3. Further develop the simulator that was created in the Project Thesis during Fall 2022.
    a. Include the rotation matrix.
    b. Expand number of connection points between each module from one to two.
4. Expand the simulator from two connected modules to multiple connected modules with 6DOF motion (surge, sway, heave, roll, pitch and yaw).
5. Use the simulator as a basis to plan the model test.
6. Perform model-scaled experiments at Lilletanken. The control at connection points can be modelled by different springs to imitate different connection stiffnesses.
7. Discuss the simulation and experiment results.
    a. Results of interest are motion of modules and forces in connections between modules.
    b. Validate the simulator with experiment results.
    c. Evaluate assumptions and simplifications made in simulator.
8. Suggest a control strategy to regulate stiffness according to sea conditions. Validate the effect of active control based on the simulator developed in 3. and 4.
9. Conclude the master thesis and propose further work.

Specifications

The student shall at startup provide a maximum 2-page week plan of work for the entire project period, with main activities and milestones. This should be updated on a monthly basis in agreement with supervisor.

Every weekend throughout the project period, the candidate shall send a status email to the supervisor and co-advisors, providing two brief bulleted lists: 1) work done recent week, and 2) work planned to be done next week.

The scope of work may prove to be larger than initially anticipated. By the approval from the supervisor, described topics may be deleted or reduced in extent without consequences with regard to grading.

The candidate shall present personal contribution to the resolution of problems within the scope of work. Theories and conclusions should be based on mathematical derivations and logic reasoning identifying the steps in the deduction.

The report shall be organized in a logical structure to give a clear exposition of background, problem/research statement, design/method, analysis, and results. The text should be brief and to the point, with a clear language. Rigorous mathematical deductions and illustrating figures are preferred over lengthy textual descriptions. The report shall have font size 11 pts., and it is not expected to be longer than 70 A4-pages, 100 B5-pages, from introduction to conclusion, unless otherwise agreed. It shall be written in English (preferably US) and contain the elements: Title page, project definition, preface (incl. description of help, resources, and internal and external factors that have affected the project process), acknowledgement, abstract, list of symbols and acronyms, table of contents, introduction (project background/motivation, objectives, scope and delimitations, and contributions), technical background and literature review, problem formulation or research question(s), method/design/development, results and analysis, conclusions with recommendations for further work, references, and optional appendices. Figures, tables, and equations shall be numerated. The contribution of the candidate shall be clearly and explicitly described, and material taken from other sources shall be clearly identified. Work from other sources shall be properly acknowledged using quotations and a Harvard citation style (e.g. natbib Latex package). The work is expected to be conducted in an honest and ethical manner, without any sort of plagiarism and misconduct, which is taken very seriously by the university and will result in consequences. NTNU can use the results freely in research and teaching by proper referencing, unless otherwise agreed.

The thesis shall be submitted with an electronic copy to the main supervisor and department according to NTNU administrative procedures. The final revised version of this thesis definition shall be included after the title page. Computer code, pictures, videos, data, etc., shall be included electronically with the report.

Start date: 16 January, 2023 **Due date:** 26 June, 2023

Supervisor: Dong Trong Nguyen
Co-advisor(s): Trine Aas-Hansen

Signatures:

Digitally signed by
Dong Trong
Nguyen
Date: 2023.06.23
12:06:55 +02'00'

Preface

This thesis is the final work of my Master of Science degree in Marine Cybernetics in Marine Technology at the Department of Marine Technology (IMT) at the Norwegian Univesity of Science and Technology (NTNU) in Trondheim, Norway.

This last semester has been an interesting and very long one. The challenges of working with this thesis have been complex, but they have given me satisfaction when overcome. From developing the numerical model in Python, where theories from the previous years have been implemented, to performing a model test of small-scaled structure. Small and large challenges have appeared, mostly when they were not expected. With great help along the way, most of them were solved.

I would therefore thank the employees at Lilletanken, especially Trond Innset, Ole Erik Vinje, Robert Opland and Terje Rosten for all the help related to any problems in the lab. I would like to give a special thanks to my lab partner and co-supervisor on this thesis, Trine Aas-Hansen. She has been extremely helpful and an important sparring partner discussing any problems that has occured. Professor Dong Trong Nguyen deserves also a large appreciation, for the support and guidance he has given during the semester.

Finally, I would like to thank my friends and classmates in the southern wing at the B-block. Espically my friends at B375 for giving joy and good academic discussions,

Trondheim
June 25, 2022

Vegard Njøten Fagerbakke
Department of Marine Technology

Abstract

The use of Floating Multi-Modular structures has the potential to significantly contribute towards achieving net zero emissions. However, these structures are still in their initial stages and require further research. This thesis explores the feasibility of an adaptive controller that can reduce connector loads and prevent excessive module movements by altering the connector stiffness. Numerical simulations and experiments on scaled-down structures with different connector stiffness have been conducted to investigate this. Four different cases have been looked into to observe the stiffness effect. The first case is with only one moored module, the second with two moored modules, the third with three modules where two were moored, and lastly, five modules with two moored modules. The first and last module was moored in the third and fourth cases.

The experiment was performed in Lilletanken, NTNU facilities at Tyholt. Here the modules were tested in regular waves with three different wave steepness. As connectors, extension springs were used. Through conducting the experiment, it is possible to observe the behavior of the module when varying levels of stiffness are applied to the connector. The results would also be compared with the simulations of the numerical model.

The numerical model obtains the hydrodynamic coefficients from WADAM based on potential flow theory and linear wave theory. Each module is defined individually, but the forces in the connectors are calculated based on the motion of the modules in a time domain simulation.

The results presented in this thesis include how the different stiffness affects the motion in surge, heave, and pitch and a comparison between the results of the simulations and the experiment. The results from the simulations overestimated the results from the experiment. But the trends are found to be good enough so adaptive controllers could be implemented in the model. Based on the experiment's results, a switching logic has been suggested. This logic will utilize the response amplitude in the frequency domain to select the most suitable stiffness for a specific wave period to minimize surge motions. A simulation visualizing the effect of the switching logic has been conducted.

During the fourth test, it was observed that the modules collided, which posed a significant issue for the two last modules when facing higher wave periods. To prevent such collisions, it is advised to conduct a thorough analysis to determine the minimum stiffness required to avoid collisions. Furthermore, including extensive damping into the numerical model is recommended. It is also suggested to perform new experiments with new connections, decreasing errors when the springs are changed.

Sammendrag

Bruken av flytende multi-modulære strukturer har potensial til å bidra betydelig til å oppnå netto nullutslipp. Imidlertid er disse strukturene fortsatt i en tidlig utviklings fase og det kreves ytterligere forskning. Denne avhandlingen utforsker gjennomførbarheten av en adaptiv kontroller som kan redusere kreftene i koblinger mellom modulene, samt forhindre overdreven bevegelse av modulen ved å endre stivheten i koblingen. For å undersøke om dette er gjennomførbart, er numeriske simuleringer og eksperimenter på skalerte strukturer utført. Fire ulike tilfeller er undersøkt for å observere effekten forskjellige stivheter har. Det første tilfellet er med bare én fortøyd modul, det andre med to fortøyde moduler, det tredje med tre moduler, der to er fortøyd, og til slutt fem moduler med to fortøyde moduler. Hvor den første og siste modulen er fortøyd i det tredje og fjerde tilfellet.

Eksperimentet ble utført i Lilletanken, ved NTNU sine fasiliteter på Tyholt. Her ble modulene testet i regulære bølger med tre ulike bølgebrattheter. I lab ble strekkfjærer som koblinger mellom modulene. Ved å utføre eksperimentet kunne man sammenligne modulenes bevegelse for de forskjellige stivheten. Resultatene skulle også brukes som til å sammenligne med simuleringene av den numeriske modellen.

Den numeriske modellen henter hydrodynamiske koeffisienter fra WADAM, som er baserer seg på potensiell strømningsteori og lineær bølgeteori. Hver modul er definert individuelt, men kreftene i koblingene beregnes basert på bevegelsen til modulene i en simulering it tidsdomenet.

Resultatene presentert i denne avhandlingen inkluderer hvordan ulik stivhet påvirker bevegelsen i jag, hiv og stamp, samt en sammenligning mellom resultatene fra simuleringene og eksperimentet. Resultatene fra simuleringene overestimerte resultatene fra eksperimentet. Men trendene er funnet å være tilstrekkelig gode til at adaptive kontrollere kan implementeres i modellen. Basert på resultatene fra eksperimentet er det foreslått en algoritme. Denne algoritmen vil bruke responsamplituden i frekvensdomenet til å velge den mest passende stivheten for en spesifikk bølgeperiode, for å minimere fremoverbevegelser. Det er gjennomført en simulering som visualiserer effekten av algoritmen.

Under den fjerde testen ble det observert at modulene kolliderte, noe som utgjorde et betydelig problem for de to siste modulene når de ble utsatt for høyere bølgeperioder. For å unngå slike kollisjoner, anbefales det å gjennomføre en grundig analyse for å bestemme den nødvendige stivheten for å unngå kollisjoner. Videre anbefales det å inkludere demping i den numeriske modellen. Videre foreslås det å utføre nye eksperimenter med en forbedret kobling.

Nomenclature

Abbreviations

AD	Amplitude Death
BVP	Boundary Value Problem
$CDPR$	Cable-Driven Parallel Robots
CO	Coordinate Origin
COG	Center of Gravity
DOF	Degrees of Freedom
F_N	Froude Number
$FMFC$	Flexible Module and Flexible Connector
$FMRC$	Flexible Module and Rigid Connector
ODE	Ordinary Differential Equation
PV	Photovoltaic
PVC	Polyvinyl chloride
RAO	Response Amplitude Operator
RK	Runge-Kutta
$RMFC$	Rigid Module and Flexible Connector
$RMFC$	Rigid Module and Rigid Connector
VCG	Vertical Center of Gravity
FFT	Fast Fourier Transform

Symbols

$\boldsymbol{A}$	Added mass matrix
$\boldsymbol{B}$	Damping matrix
$\boldsymbol{C}$	Restoring matrix
$\boldsymbol{M}$	Rigid body mass matrix
ϵ	Wave steepness
η_j	Motion in mode j
η_{j_a}	Motion amplitude in mode j
λ	Wave length

ν_j	Velocity in mode j
ν_{j_a}	Velocity amplitude in mode j
ω	Wave frequency
ω_n	Eigenfrequency
ρ	Water density
θ	Phase difference
φ	Velocity potential
ζ	Wave elevation
F_j^{exc}	Excitation force in mode j
k	Wave number
T	Wave period
T_n	Eigenperiod

Table of Contents

List of Figures

List of Tables

Chapter 1

Introduction

1.1 Motiovation and Background

Over the past six decades, the maritime industry has experienced significant growth. The construction of oil platforms, floating cities, and wind turbines on water has become increasingly important and relevant to the world. Given the rising population, energy demand, and excessive CO_2 emissions, expanding the capacity for renewable energy production has become imperative. An approach to solve these problems is creating floating modules and placing them in the ocean. By connecting multiple modules to create a floating island, enormous areas can be created for storage or energy production. The concept might be defined as Multi-Module structures. However, the idea is not new. Already in the 1920s, the idea of building a floating station in the Atlantics was formed by Lincoln & Armstrong (1934). Later in the 1940s, the US Military started showing interest in these constructions and developed a floating pontoon deck. It consisted of multiple pontoons connected with hinges, totaling 552 meters.Despite being situated in sheltered waters and utilized for numerous takeoffs and landings, the object ceased operation in the 1960s due to safety concerns related to the takeoffs and landings (Suzuki et al. 2007). Later, in the 1970s, the ideas of floating islands and floating land areas blossomed in Japan. With the lack of land areas, the idea of building the Kansai International Airport as a floating airport was proposed in 1973. The idea was again inspired in Japan, and the Technological Research Association of Megafloat (TRAM) was formed in 1995. During their active period from 1995 to 2001, they studied on the *MegaFloat*, which they even tested with a 1000 meter long model(Suzuki 2005). The MegaFloat is designed as a rectangular pontoon structure, where they have a small draft compared to the length. Due to their simple design, high stability, and cheap maintenance, they are easy to produce. However, the design makes them suitable for calm water areas like lakes and inshore waters(Lamas Pardo et al. 2015).

At the same time the MegaFloat was developed and researched on in Japan, the US Navy developed the This concept is inspired by semi-submersibles that are used for oil and gas operations. However, instead of one large, multiple large semi-submersibles are connected. These semi-submersibles were later called modules, and they could have a length and width of 220-500 meters and 120 - 170 meters. By creating the modules separately, they could be separated under transit and relocated easier. While under operation they could be connected, creating a large structure (Lamas Pardo et al. 2015). By creating multiple modules, it will also a reduced bending moment and shear stresses acting in connections between the modules. Further, as an opposite to the MegaFloat, the MOB could be placed in offshore conditions (Lamas Pardo et al. 2015).

Even though the VLFS might be defined as structures over 1000 meters, the idea of connected modules is frequently developed in a smaller scale, which can be referred to as Multi-Modules. The idea is the same as for the MOB. Connecting stiff floaters in matrices creates a floating island. An industry that could benefit of the Multi-Module is the solar industry. By placing photovoltaic (PV) , more commonly known as solar panels, on the ocean, large land areas can be available. In recent years, the concept of floating solar has been taken up by multiple companies. Many existing floating solar plants are placed on lakes or water dams, giving little to no waves. So now it is being looked into moving these plants offshore. A company suggesting this is Moss Maritime, which, together with Equinor, has an idea about a Multi-Module Float Solar Island. Combining multiple modules into a large floating island can attain hydrodynamic flexibility and structural strength while handling relatively rough sea states (Onsrud 2019). A pilot plant for this concept was planned outside Frøya, Norway, in 2022. However, after being postponed, it was canceled in 2023. However, during the summer of 2022, the Dutch-Norwegian company SolarDuck performed a successful model test Offshore-Energy (n.d.). Later in 2022, they could inform that they were awarded a contract to build the first offshore floating solar demonstrator in Tokyo Bay.

With the increased focus on Multi-Module structures and the opportunities it gives. Obtaining knowledge about how a Multi-Modular structure behaves together and how it can be utilized for a new project is an important step to take further. With the help of numerical simulation programs that can replicate the behavior, it will be easier to figure out how to solve problems related to these concepts. As full-scale test sites might be expensive and, in some cases, be large failures, creating the tools to help develop to avoid these scenarios will be important.

1.2 Literature Review

A literature review was conducted to understand what problems related to Multi-Modules exist. In this chapter, a further understanding of how modules act together as a floating island is investigated by looking at the *Network Modelling* methodology. Further, different methods to connect the modules are examined. Here the problems with the different approaches will be presented, and different suggestions for solutions. Lastly, by obtaining the best connection stiffness between modules, a phenomenon called amplitude death (AD) state be attained. The last part will not be further explained or examined in the master thesis, but it could be interesting in further work to figure out the AD state of the system which will be presented later in this thesis.

1.2.1 Network Modelling

Since the start of the VLFS there have been some developments in the method of how to model the systems that include VLFS. There are various ways to model the module and the connector when dividing a VLFS into multiple modules and connecting them with connectors. By either stating that the module is rigid or flexible, and if the connectors are rigid or flexible, opens for four different models: *Rigid Module and Flexible Connector* (RMFC), *Rigid Module and Rigid Connector* (RMRC), *Flexible Module and Rigid Connector* (FMRC) , and *Flexible Module and Flexible Connector* (FMFC) . The assumption of a rigid module means that any arbitrary point on the module does not move relative to each other. However, if the module is assumed flexible, relative motion can arise (Fu et al. 2007). In the case where RMFC is used, it is assumed that the deformations occur in the connectors due to the much higher flexibility. If the FMFC approach should be used, the module's stiffness should be included in the calculations. The approach of using RMFC has been widely used due to its usefulness in the study of motions and connector forces.

Two methods have been discovered that can be used to calculate the motion of connected models. The first was introduced in a parametric study by Riggs et al. (1999) and is known as the *hydro-elastic method.* The study explored the impact of stiffness on the response of five MOBs. The RMFC method is utilized to model the system, wherein the connectors are represented as linear translation springs. The second method is called *network modeling method* and was introduced by Xu et al. (2014). The method compares the modules and connectors with nodes and links in a network model, as seen in **??**. Where connector forces in the hydro-elastic method are linear, and the springs are modeled as zero-length springs. This assumes the module's dimension is much larger than the dimensions of the connector. As opposed to this, the network method accounts for the non-linearities that could occur from the geometrical deformation of the connector or the elastic materials used in the connector. Xu et al. (2015) presented an analysis where the linear results from the hydro-elastic method underestimate the actual results. This is due to the non-linearities in the system that are ignored. The geometrical effects could be expected to have increasing importance for the system when the modules have smaller dimensions.

Both methods have a mutual advantage as they require only one hydrodynamic analysis of the modules. Such analysis would provide the excitation force, added mass, damping, and hydrostatic stiffness. In the study of the five MOBs, each module can be defined by 6 DOFs. Where 30 DOFs can define the five modules, the system is defined as one system using the deformation between two modules' centers of gravity and a stiffness matrix to calculate the connector force. With the network method, each module can be looked at individually and the couplings are defined through a topological matrix. Through the topology matrix, the floating island can be defined in every possible way, and modules that are connected can easily be redefined.

1.2.2 Connectors

With the approach of connecting multiple modules, much of it relays on the connectors. The connectors should not only be able to restrain the forces applied but also withstand corrosion and fatigue and easily attach to other modules. This chapter will focus on what types of connectors are tested, their differences, and when the different types are most beneficial.

In general, there exist multiple different types of connectors, which can be combined to restrict motion in different degrees of freedom (DOF) . They depend on what type of VLFS they are using since the connector could affect the relative motion response of the modules. For some structures, it is necessary to restrict relative motion in certain directions; in other cases, it is not as important. Further, it is possible to divide the connector systems into systems with a *gap* or *No gap* between the modules. In the cases with No gap, it can again be divided into three categories: rigid, semi-rigid, and hinge. In the case of a rigid system, the connector restricts the module from moving in the wanted DOFs. Semi-rigid is not so much different but is generally assumed to have less stiffness. However, large moments could occur in severe sea conditions with rigid connectors. The moments will not be transmitted if hinges are used in the connectors instead. The axial and shear forces inside these connectors would still be present and must be accounted for. One type of hinge connector is exemplified in Figure 1.1b.

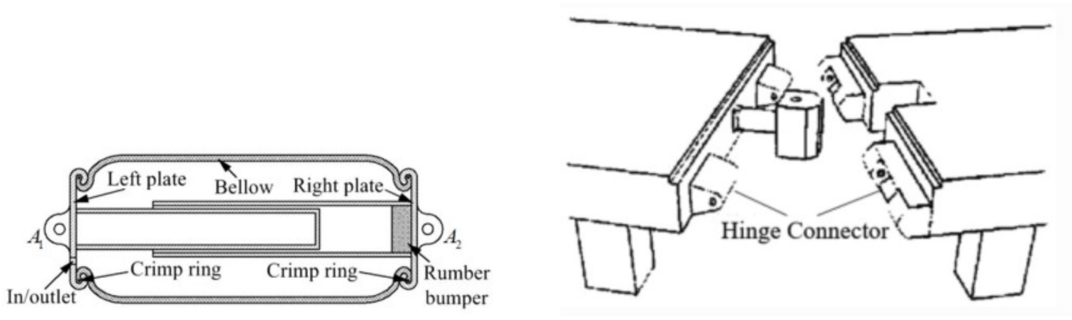

(a) An air-spring connector. *Source:* Xia et al. (2016)

(b) An example of a hinge connector configuration. *Source:* Chen et al. (2020).

Figure 1.1: Examples of a flexible connector and a hinge connector

In the other case, a gap between the modules can be divided into four categories: rigid, vertical-free, hinge, and flexible connectors. Rigid and hinge are much alike as for the case with no gap. Vertical-free, can on the other hand, prevent surge and sway motions, and also either restrict or allow rotations. However, the flexible connectors will be looked into further here. From Jiang et al. (2021), the flexible connectors are applicable when the modules are moored, or other relative motions are allowed. Depending on the flexible connector, it would limit the moment and shear force acting in the connections. An example of this is presented in Zhang et al. (2014), where a rubber-cable connector is used. The rubber's purpose is to limit the motion between two modules when compression forces occur, and the cable should limit the tension forces.

A topic that is of interest is adjusting the stiffness of the connectors. By using flexible connectors, it will be possible to balance load and motion response. By adjusting the connector stiffness, the dynamics of the modules could be influenced when a change in the sea states happens. However, this demands that the stiffness could change depending on the sea state. Xia et al. (2016) proposed to use air-springs to keep the modules in a weak oscillatory state, as seen in Figure 1.1a. The connector stiffness could be adjusted along with changing sea states by adjusting the pressure inside the air spring. In the figure, rubber bumpers are also included to reduce the impact in extreme conditions. However, to be functional, it demands that the sensor signals are correct in all conditions, which could become a problem.

The same author proposed in Xia et al. (2022) another connector that could deal with varying sea states. A stiffness-adjustable connector consisting of a passive spring with an active hydraulic actuator inside could provide time-dependent adaptive control forces. The spring provides constant stiffness in the translational directions, while the actuator provides an additional control force. This connector's sketch is shown in Figure 1.2. While changing the hydraulic pressure in the actuator, an axial force is produced, which, combined with the spring, produces a stiffness that could suppress the motions. The actuators are controlled by a feedback control scheme that uses the floating bodies response, where Sequential Quadratic Programming determines the feedback gains. The study compared the actuator with a hinge and flexible connector. Compared to the hinge they were able to reduce the connector loads, however they obtained a slightly larger peak load compared to the flexible connector. However, they were able to reduce the response of the modules compared with the flexible connector.

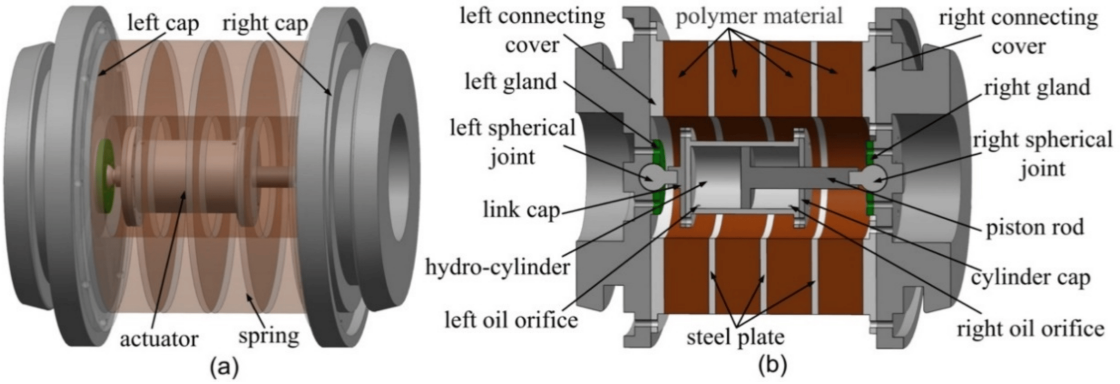

Figure 1.2: Sketches of the stiffness-adjustable connector proposed by Xia et al. (2022).

These two connectors presented are only proposed and tested numerical, meaning there lacks validiation of the results. There are in the matter of fact little experimental testing on VLFS with flexible connectors. However, two cases have done some experimental testing. Shi et al. (2018) proposed a connector for an experiment for floating platforms. The connector is presented in Figure 1.3. It consists of five elastic components, all with a stiffness of 10E5 N/m. The mounting plate is further placed on each of the modules. There will be two components in the x- and z-direction, with one in the y-direction. With this connector, obtaining the same distance between the modules in still water will be possible. The paper compares experimental test results with the network modeling method by (Xu et al. 2015) and the hydro-elastic method by Riggs et al. (1999). In addition, a linearized approximation of the network modeling method was developed. However, the results indicated that the network modeling method agrees well with the experiment. Of the three numerical methods, the linearized network method was the better.

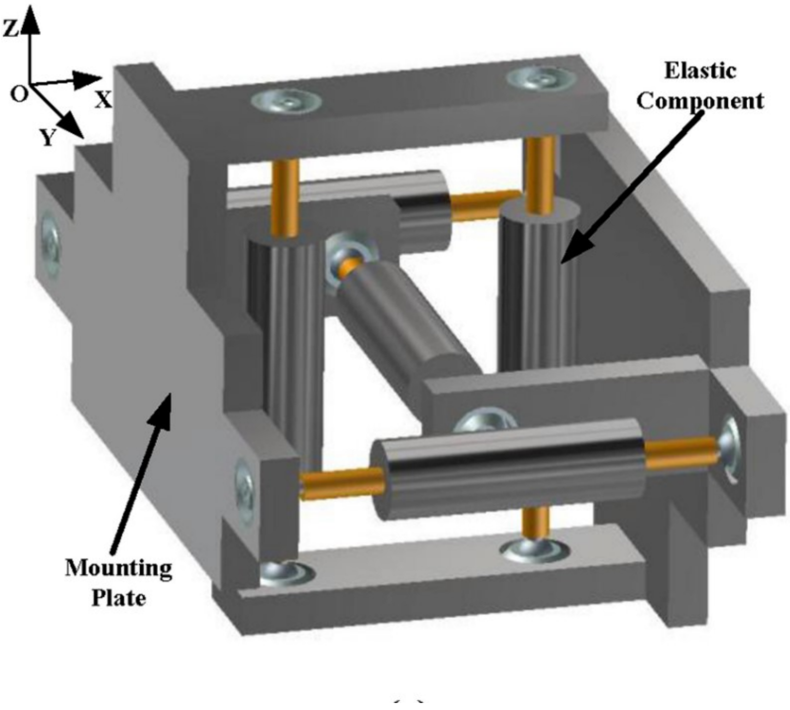

Figure 1.3: An example of a connector used in experimental testing for floating modules. (Shi et al. 2018)

In an article by Ding et al. (2022), they examined the effect of different connector configurations. Three different configurations were created, as seen in Figure 1.4. They are defined from left to right as type I, II, and III. Between the two plates, extension springs are used. A spring of an initial length of 0.04 meters is used in the longitudinal direction. For type III, a spring with an initial length of 0.025 meters is added in the vertical direction. In the experiment, they used two of each type between modules, giving two connection points between them. Type I, the extension springs, are supposed to provide elastic constraint in the longitudinal direction. While type II should provide a constraint in longitudinal and pitch. Type III has extra beams at the top, middle, and bottom to support the vertical springs. Hence, it should be able to provide elastic constraints in the longitudinal, vertical, and pitch directions. Further was their goal to investigate the effect of the different configurations on the stability of the multi-module floating structure. To handle compression, the longitudinal springs were stretched to 0.08 meters. They

Figure 1.4: The three different connector configuration proposed by Ding et al. (2022)

The concluding remarks were that type II affected the system's dynamics less than type I. Type III improved the system's stability compared to the other types. However, as these two experimental connector configurations could provide important information regarding multi-module behavior, there are still some steps in recreating the numerical connectors. To the author's knowledge, experimental validation with adaptive stiffness control has not been conducted. By obtaining an adaptive stiffness control in the model scale, it would, amongst other things, be possible to validate the theory about the amplitude death (AD) state.

1.2.3 Amplitude death

The phenomenon of AD was first discovered Bar-Eli (1984) while exploring chemical oscillators. The findings were that the oscillations could suddenly be suppressed to low amplitudes in coupled systems. This state has been a topic of interest for some researchers in the marine field. In Zhang et al. (2015), a numerical study on a multi-module floating airport was conducted. Looking at an array of floating modules, they performed simulations with different connector stiffness between them. They were able to present that indeed by changing the stiffness they could attain the AD state for different sea states. To maintain the AD state, this demands that the connector stiffness must be able to change accordingly Xia et al. (2016). Otherwise, the motion of the modules and the forces in the connectors could destroy the modules. Developing and creating a connector that could change the stiffness of the connector during experimental testing would help further understand a system consisting of multiple modules.

1.3 Research Gap

From the literature review that has been conducted, a few research gaps have been spotted. There have been published many research articles about multi-modular arranged in a row configuration but there are limited articles about multi-modular structures in both longitudinal and lateral directions. There are also, to the author's knowledge no adaptive connectors that have been tested on model-scale structures. This could be an important step, as it will validate the effect different stiffness has on the connector.

1.4 Objectives and Scope

The objective of this thesis is to study the effect of adaptive connectors that can change their characteristics on the performance of a whole multi-modular island in varying sea states. By achieving this, the operational window of the island can be extended, enabling its placement further offshore, hence reducing conflict with nearshore value-creation activities, such as shipping, aquaculture, etc. To address this objective, the research questions are as follows:

- What are the main issues of a multi-modular island in terms of dynamic response? How to model effectively these main dynamics and how to validate these models?
- Can the use of adaptive connectors improve the overall performance of a multi-modular structure?

To answer these questions, this thesis will contribute in the following ways:

- Development of a simulator, which serves as an initial version of the digital twin. Building upon the simulator developed during the project thesis, the following enhancements will be made:
  - Take account of larger angles by implementing a rotation matrix
  - Include the drag term for the Morison equation
  - Expand the number of connections between two modules from one to two
- Validation of the proposed simulator through experimental study with a scaled model of multi-modular structure. This validation process aims to assess the simulator's accuracy in representing the real-world behavior of the multi-modular structure.
- Proposal of a control logic that can facilitate the change of the connector's characteristics with the particular focus on stiffness

1.5 Master Thesis Outline

Chapter 2 the theory relevant to this thesis will be introduced. It is mainly related to the simulator, which is explained later. In Chapter 3, an explanation of the module used in the experimental and numerical parts is defined.

In Chapter 4, the numerical model, or simulator, is explained. The chapter contains an explanation of how the simulator is built. The code is not described in detail, but the basic setup is given.

In Chapter 5, the experiment is presented. A summary of which errors could affect the outcome of the results is also presented.

In Chapter 5, the results from the experiment are presented. A comparison between the simulator and the experiment follows.

In Chapter 7 conclusion and further work are presented.

Chapter 2

Theory

The theory sections is mainly from the project report, some new theory has been added. However, the theory is presented to give a background of the theory that has been used in the numerical model.

2.1 Potential Flow Theory

As this thesis will work around the wave-induced forces and motions on floating modules, an introduction to the potential flow theory seems necessary. The theory is used to simplify reality, such that the interaction between floating objects and surface waves can be modeled. With potential flow theory, the velocity potential φ is introduced, and it is related to the fluid velocity through the assumption that the flow is irrotational. An irrotational flow can be expressed as $\nabla \times \mathbf{u} = 0$, where $\mathbf{u} = \nabla\varphi$. ∇ is a vector of the partial derivatives, such as $\nabla = [\partial/\partial x, \partial/\partial y, \partial/\partial z]$. In addition, it is assumed that the fluid is inviscid and the flow is incompressible. Assuming inviscid fluid leads to no vortices being present. Potential flow theory may not be an adequate approximation in certain scenarios because of its inviscid assumption, such as when flow separation is significant.

Further, the Bernoulli equation can be derived from the Navier-Stokes equation when introducing the velocity potential. A further explanation can be viewed in Bachynski et al. (2019). However, the Bernoulli equation can be written as

$$\frac{\partial\varphi}{\partial t} + \frac{1}{2}\nabla\varphi \cdot \nabla\varphi + gz + \frac{p}{\rho} = 0 \tag{2.1}$$

This can further be rewritten so it is possible to find the pressure

$$p = -\rho g z - \rho\frac{\partial\varphi}{\partial t} - \frac{1}{2}|\nabla\varphi \cdot \nabla\varphi|. \tag{2.2}$$

The last term will at least be of second order, regardless of what order the velocity potential is. The second term will, on the other hand, depend on the order of the velocity potential, which can be given as seen in (2.4a). By second order, it is meant that the terms are either linear or proportional to the square of the wave amplitude.

2.2 Linear Wave Theory

It is still necessary to find the velocity potential. To this, the boundary value problem (BVP) must be solved. To solve the BVP some requirements have to be fulfilled. The problem is that the BVP is nonlinear, so a linearization of the problem BVP is done to proceed. However, it is assumed that the velocity potential can be represented as a power series, where a small parameter ε is introduced. Here, $\varepsilon = H/\lambda$, which represents the wave steepness. Further is the wave number,$k = 2\pi/\lambda$, and H is the wave height. It is then possible to approximate the velocity potential and the wave amplitude as the following series

$$\begin{aligned} \varphi &= \varphi_1(O(\varepsilon)) + \varphi_2(O(\varepsilon)^2) + \varphi_3(O(\varepsilon)^3)... \\ \zeta &= \zeta_1(O(\varepsilon)) + \zeta_2(O(\varepsilon)^2) + \zeta_3(O(\varepsilon)^3)... \end{aligned} \tag{2.3}$$

When solving the linearized BVP, only the first order terms are used, hence the solution will be linear. The final solutions from solving the BVP are the first order velocity potential, wave propagation, and the dispersion relationship.

$$\varphi = \frac{g\zeta_a}{\omega}\frac{\cosh\left(k(z+h)\right)}{\cosh\left(kh\right)}\cos(\omega t - kx) \tag{2.4a}$$

$$\zeta = \zeta_a \cos\left(kx - \omega t\right) \tag{2.4b}$$

$$\omega^2 = kg\tanh\left(kh\right) \tag{2.4c}$$

Here ζ_a is the wave amplitude, k is the wave number and ω is the wave frequency. The wave frequency, ω, can be given as $\frac{2\pi}{T}$, where T is the wave period. A propagating wave as expressed in $(2.4b)$, will propagate in positive x-direction. Further, when the waves have a constant amplitude, wavelength, and period they are said to be regular waves.

When the velocity potential is found, it can be used to find the fluid velocity and acceleration. The fluid velocity in x- and z-direction is presented in (2.5), while the respective acceleration is presented in (2.6).

$$u = \omega\zeta_a\frac{\cosh\left(k(z+h)\right)}{\sinh\left(kh\right)}\sin(\omega t - kx) \tag{2.5a}$$

$$w = \omega\zeta_a\frac{\sinh\left(k(z+h)\right)}{\sinh\left(kh\right)}\cos(\omega t - kx) \tag{2.5b}$$

$$a_1 = \omega^2\zeta_a\frac{\cosh\left(k(z+h)\right)}{\sinh\left(kh\right)}\cos(\omega t - kx) \tag{2.6a}$$

$$a_3 = -\omega^2\zeta_a\frac{\sinh\left(k(z+h)\right)}{\sinh\left(kh\right)}\sin(\omega t - kx) \tag{2.6b}$$

In (2.5) and (2.6), the wave propagates from right to left in the positive x-direction. This can be more generalized, so it is possible to account for the direction the wave propagates from. In (2.7), the generalized velocity and acceleration is presented(Pettersen (2020)).

$$u = \omega\zeta_a\frac{\cosh k(z+h)}{\sinh kh}\sin(\omega t - kx\cos\beta - ky\sin\beta) \tag{2.7a}$$

$$a = \omega^2\zeta_a\frac{\cosh k(z+h)}{\sinh kh}\cos(\omega t - kx\cos\beta - ky\sin\beta) \tag{2.7b}$$

Second-order

As mentioned earlier, it is possible to keep the second-order terms in (2.2). This will include some new effects that were neglected by only assuming linear wave theory. Some important second-order effects that will appear are mean, difference, and sum frequencies. For an incident wave with a first-order velocity potential, the third term on the right-hand side in (2.2) will be nonlinear. With the velocity potential given as

$$\varphi_1 = \frac{g\zeta_a}{\omega} e^{kz} \sin(\omega t - kx + \varepsilon_1) \tag{2.8}$$

With respect to x, a further derivation can be given on the $\nabla\varphi \cdot \nabla\varphi$ term as follows,

$$\begin{aligned} (\frac{\partial \varphi}{\partial x})^2 &= (-\zeta_a e^{kz} \cos(\omega t - kx + \varepsilon_1))^2 = A^2 cos^2(\omega t - kx + \varepsilon_1) \\ &= A^2 \frac{1 + \cos(2\omega t + \varepsilon)}{2} = \frac{A^2}{2} + \frac{A^2 \cos(2\omega t + \varepsilon)}{2} \end{aligned} \tag{2.9}$$

As seen from (2.9), even for an incident wave oscillation with one frequency, ω, it will originate nonlinear effects. In this case, there are mean and sum-frequency. The mean frequency is the constant term in (2.9), while the sum-frequency is the term that depends on 2ω.

2.2.1 Reference frame

In this thesis, two reference frames will be of interest: the body-fixed reference frame and the Earth-fixed reference frame. Referring to Figure 2.1, the body-fixed reference frame is fixed to the vessel. The $X_E Y_E Z_E$-frame denotes the Earth-fixed reference frame, and here the vessel's position is defined relative to a set origin. The $X_b Y_b Z_b$-frame denotes the body-fixed reference frame or body frame. In a body-fixed frame, the origin is assumed at the still water plane (Sørensen 2018). In common marine cybernetics, it is customary to orient the z-axis downwards.

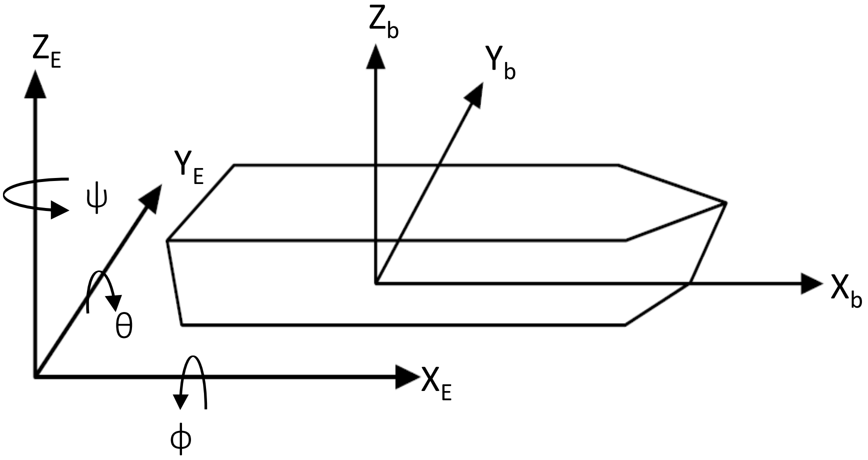

Figure 2.1: Reference frame for a marine vessel

The Euler angles ϕ, θ, and ψ are respectively rotations about the Earth-fixed axis X_E, Y_E, and Z_E. When the body-fixed reference frame rotates relative to the Earth-fixed reference frame, it can be translated back with the Euler angles. A rotation matrix, **R**, can translate values from the body-fixed frame to the Earth-fixed reference frame for the linear motions. This can be exemplified by finding the Earth-fixed reference frames' velocity, $\dot{\eta}_1$, from the body-fixed reference frames' velocity ν_1

$$\dot{\eta}_1 = \mathbf{R}\nu_1. \tag{2.10}$$

The rotation matrix is presented in (2.11).

$$\mathbf{R} = \begin{bmatrix} cos\psi cos\theta & -sin\psi cos\theta + cos\psi sin\theta sin\phi & sin\theta sin\phi + cos\psi cos\phi sin\theta \\ sin\psi cos\theta & cos\psi cos\theta + sin\psi sin\theta sin\phi & -cos\theta sin\phi + sin\psi sin\phi cos\theta \\ -sin\theta & cos\theta sin\phi & cos\theta cos\phi \end{bmatrix} \tag{2.11}$$

When there is a six DOF system, the angles in the body-fixed system also need to be translated. This is done through a transformation matrix denoted as **T**, shown in (2.12).

$$\mathbf{T} = \begin{bmatrix} 1 & sin\phi tan\theta & cos\phi tan\theta \\ 0 & cos\phi & -sin\phi \\ 0 & sin\phi/cos\theta & cos\phi/cos\theta \end{bmatrix} \tag{2.12}$$

These can be combined to a 6x6 matrix, **J**, which then can be used to translate all six dofs between the two different reference frames.

$$\mathbf{J} = \begin{bmatrix} \mathbf{R} & 0_{3x3} \\ 0_{3x3} & \mathbf{T} \end{bmatrix} \tag{2.13}$$

2.2.2 The Equation of Motion

To calculate the motions of the module, Newton's second law applies. With a rigid body mass matrix, $\boldsymbol{M} \in \mathbb{R}^{6x6}$, its possible to start with

$$\boldsymbol{M}\ddot{\boldsymbol{\eta}}_{\boldsymbol{j}} = \boldsymbol{F}_j \quad for \quad j = 1, 2, ..., 6 \tag{2.14}$$

Here $\ddot{\boldsymbol{\eta}}_{\boldsymbol{j}}$ is the acceleration, and $\boldsymbol{F_j}$ is the force acting in direction j. In order to calculate velocities and motions, it is necessary to integrate (2.14) in time. Since the equation is a second-order ordinary differential equation, two initial conditions are needed for each DOF. One for the initial position $\boldsymbol{\eta_0} = \boldsymbol{\eta(0)}$, and one for initial velocity $\dot{\boldsymbol{\eta}}_{\boldsymbol{0}} = \dot{\boldsymbol{\eta}}\boldsymbol{(0)}$. As the module floats in water, the force $\boldsymbol{F_j}$ can be replaced by the hydrodynamic loads, which are found in Chapter 2.2.2.

$$\boldsymbol{F_j} = \boldsymbol{F_j^{exc}} - \boldsymbol{A}\ddot{\boldsymbol{\eta}}_{\boldsymbol{j}} - \dot{\boldsymbol{\eta}}_{\boldsymbol{j}} - \boldsymbol{C}\boldsymbol{\eta_j} \quad for \quad j = 1, 2, ..., 6 \tag{2.15}$$

Inserting (2.15) into (2.14), Newton's second law for the module can be rewritten as

$$\boldsymbol{M}\ddot{\boldsymbol{\eta}}_{\boldsymbol{j}} = \boldsymbol{F_j^{exc}} - \boldsymbol{A}\ddot{\boldsymbol{\eta}}_{\boldsymbol{j}} - \boldsymbol{B}\dot{\boldsymbol{\eta}}_{\boldsymbol{j}} - \boldsymbol{C}\boldsymbol{\eta_j} \quad for \quad j = 1, 2, ..., 6 \tag{2.16}$$

By rearranging (2.16), the more traditional equation of motion for a floating body can be obtained

$$(\boldsymbol{M} + \boldsymbol{A})\ddot{\boldsymbol{\eta}}_{\boldsymbol{j}} + \boldsymbol{B}\dot{\boldsymbol{\eta}}_{\boldsymbol{j}} + \boldsymbol{C}\boldsymbol{\eta_j} = \boldsymbol{F_j^{exc}} \quad for \quad j = 1, 2, ..., 6 \tag{2.17}$$

Where $\boldsymbol{A} \in \mathbb{R}^{6x6}$ is the added mass matrix, while $\boldsymbol{B} \in \mathbb{R}^{6x6}$ and $\boldsymbol{C} \in \mathbb{R}^{6x6}$ are the damping and hydrostatic stiffness matrices. $\boldsymbol{F_j^{exc}}$ is the excitation forces. These coefficients and excitation force can be found by potential theory and will be presented in the following chapter.

Linear hydrodynamic loads

Because of the assumptions above with linear wave theory and potential theory, the hydrodynamic loads acting on the module can be calculated by solving two sub-problems; the diffraction and radiation problems. The velocity potential can be divided into eight auxillary velocity potentials, one for the diffracted wave,φ_7, one for the incident wave, φ_0, and one for each of the six DOF body motions, $\varphi_i, i = 1, 2, ..., 6$. When looking at the diffraction problem, it is assumed that the module is restrained from moving, making it possible to calculate forces and moments induced by incident regular waves. These forces and moments consist of a Froude-Kriloff and diffraction part and are called wave excitation loads. The excitation loads can be calculated by solving (2.18), where the velocity potentials ϕ_0 and ϕ_7 are solved over the wetted body surface S_{OB}.

$$F_j^{exc} = F_j^{FK} + F_j^{diff} = \int_{S_{OB}} \rho \frac{\partial \phi_0}{\partial t} n_j dS + \int_{S_{OB}} \frac{\partial \phi_7}{\partial t} n_j dS \tag{2.18}$$

Furthermore, when solving the radiation problem, added mass, A_{jk}, damping, B_{jk}, and restoring, C_{jk}, terms can be obtained. This indicates that the motion in mode k produces a load in mode j, which is indicated by (2.19). In the radiation problem, the module is forced to oscillate with the wave frequency ω. Since the module has six degrees of freedom, the added mass and damping can be expressed by two 6x6 matrices.

$$F_{jk}^{hd} = -A(\omega)_{jk}\ddot{\eta}_j - B(\omega)_{jk}\dot{\eta}_j \tag{2.19}$$

From (2.19) it is also indicated that the added mass and damping are frequency dependent. This is because they are found by using the velocity potential, which depends on the incoming wave frequency, ω. In addition to the diffraction and radiation problem, the hydrostatic restoring forces must be calculated. This force depends on the change in hydrostatic pressure acting on the module, which will change when the buoyancy changes. The restoring loads can be written as

$$F_{rj} = -C_{jk}\eta_j \tag{2.20}$$

Here C_{jk} is the restoring coefficient, while $\boldsymbol{\eta}$ is the motion. When the module is floating in still water it will obtain an equilibrium position, and a change in either heave, roll, or pitch, will create a change in volume displacement. This will not be the case in surge, sway, or yaw, hence no restoring loads in these directions. If the module is symmetric in the XZ-plane there will be several zero coefficients. Assuming the same 6 DOFs as above, the only non-zero terms in a 6x6 matrix will be C_{33}, C_{35}, C_{53}, C_{44} and C_{55}. If there in addition is symmetric properties in the YZ-plane, C_{35} and C_{53} will be zero as well.

2.3 Morison's Equation

To be able to calculate the wave loads acting on the modules, Morison's equation can be used on the cylindrical pontoons. This will also account for viscous forces when they matter, which potential flow theory disregards. Morison's equation is often used for cylindrical offshore structures, where the horizontal force, dF, is found on a strip dz of the cylinder.

$$dF = \rho\frac{\pi D^2}{4}C_M a_x dz + \frac{1}{2}C_D D u|u| dz \tag{2.21}$$

Here the u and a_x are the horizontal undisturbed fluid velocity and acceleration at the midpoint of the cylinder, while C_M and C_D are the mass and drag coefficients. These are determined empirically. The velocity and acceleration can be found by derivating the velocity potential, which is shown in (2.5) and 2.6. The total force acting on the cylinder can hence be found by summation of all the strips

In the case when the pontoon is moving, the velocity term must also take into account the velocity of the pontoon. This will give a relative velocity, which depends on both the fluid velocity and the pontoon velocity. The horizontal force, dF, can then be rewritten as

$$dF = \rho\frac{\pi D^2}{4}C_M a_x dz + \frac{1}{2}C_D D(u - \dot{\eta})|u - \dot{\eta}| dz \tag{2.22}$$

2.4 Numerical solution of ordinary differential equations

In this project thesis, a numerical integrator is used to solve ordinary differential equations(ODE), which will be used to simulate the dynamic system. The differential equation depends on an initial value that is independent of x, this is what's called an initial-value problem. It can be further be expressed as this general first-order differential equation

$$\dot{y} = f(x, y), \quad y(x_0) = y_0 \tag{2.23}$$

where $\dot{y}$ is the time derivative of y and y_0 is the initial value of y. As this is a general example, the real problem can be more complicated, and not every method to solve the equation is suited for the problem. For the different methods, there exists different approaches to how they integrate. Some methods are one-step, these methods will only approximate y_{n+1} based on y_n. A multi-step method depends on a limited number of the previous steps, y_{n-1}, y_{n-2},..., y_0. The formula for a linear multi-step approach is given by

$$y_n = \sum_{j=1}^{K_1} \alpha_j y_{n-j} + h_n \sum_{j=0}^{K_2} \beta_j f(y_{n-j}) \tag{2.24}$$

where the integers K_1 and K_2, and coefficients α_j and β_j depend on the specific method. h_n is the step size, and the subscript n indicates at which step the step size should be used. By examination of (2.24), it will become obvious that the last term depends on y_n when $j = 0$. In this case, the method is said to be implicit because the solution depends on y_n. Otherwise, the method is an explicit method since it is possible to solve y_n directly. An advantage of using implicit methods is that they are better suited for solving stiff problems. It is hard to tell if the problem is stiff or not, but if the step size has to be very small to get an accurate solution, the problem might be stiff. It is wanted that the step size is chosen so the accuracy of the simulation is as good as possible. Explicit methods would, for stiff problems, adjust the step size to keep the simulation stable, which will affect the simulation time and accuracy Pedersen & Engja (2014). This is because explicit methods are conditionally stable, meaning the area where the method is stable depends on the step size. Implicit methods, however, are said to be unconditionally stable since they do not depend on the step size Bishop (n.d.).

A commonly method thats been used to solve ODEs are *Runge-Kutta* (RK). In the next chapter,a short presentation of this method will be provided.

2.4.1 Runge-Kutta

The Runge-Kutta family has many different variants, both explicit and implicit methods. The explicit Runge-Kutta of order 5(4) (RK45) method will be presented here. It can be described as a set of single-step methods that tries to predict the next step based on the stage derivative, k. The prediction of y_n will then be a weighted sum of these stage derivatives, as seen in (2.25).

$$y_n = y_{n-1} + h \sum_{j=1}^{4} b_j k_j \tag{2.25}$$

The stage derivatives of an RK45 can further be defined as

$$\begin{aligned}
k_1 &= f(t_{n-1}, y_{n-1}) \\
k_2 &= f(t_{n-1} + c_2 h, y_{n-1} + h a_{21} k_1) \\
k_3 &= f(t_{n-1} + c_3 h, y_{n-1} + h(a_{31} k_1 + a_{32} k_2) \\
k_4 &= f(t_{n-1} c_4 h, y_{n-1} + h(a_{41} k_1 + a_{42} k_2 + a_{43} k_3)
\end{aligned} \tag{2.26}$$

The coefficients b, c, and a depend on the method. For example, for an RK45, these coefficients can be given by a Butcher Tableau Butcher (n.d.). The resulting approximation of y_n is achieved by putting the stage derivatives in (2.26) into (2.25).

$$y_n = y_{n-1} + \frac{h}{6}(k_1 + 2k_2 + 2k_3 + k_4) \tag{2.27}$$

2.5 Multiple Degree-of-Freedom Systems

Multiple degree-of-freedom systems are a way to describe the response of a system with multiple DOFs. Ships and other floating structures can move in six DOFs, which would be inaccurate only to describe one degree. For connected modules, it would be interesting to calculate the eigenvalues in surge. A review of a method calculating the eigenvalues will be presented below. However, for more details please see Bachynski et al. (2019). Assuming that two moored modules can be represented by a mass m_1 and m_2, connected through a spring with stiffness k_2. Such a system can be represented like the figures in Figure 2.2. Here k_1 and k_3 presents the mooring.

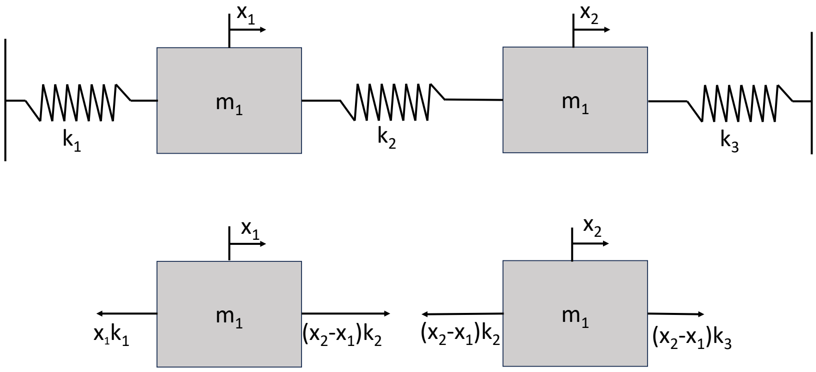

Figure 2.2: Example of system with two translational degrees of freedom, With a corresponding free body diagram, adapted from Bachynski et al. (2019).

The system is undamped and no external force acts on the modules. From the free-body diagram, the forces acting on the bodies can be found as

$$\begin{aligned}
m_1 \ddot{x}_1 &= -k_1 x_1 + k_2(x_2 - x_1) \\
m_2 \ddot{x}_2 &= -k_2(x_2 - x_1) - x_2 k_3
\end{aligned} \tag{2.28}$$

Here the equations are two coupled second-order differential equations. These can be expressed in matrix form as in (2.29). Where the mass matrix, **M**, and stiffness matrix, **K**, can be defined as in the equation.

$$\underbrace{\begin{bmatrix} m_1 & 0 \\ 0 & m_2 \end{bmatrix}}_{\mathbf{M}} \begin{bmatrix} \ddot{x}_1 \\ \ddot{x}_2 \end{bmatrix} + \underbrace{\begin{bmatrix} k_1 + k_2 & -k_2 \\ -k_2 & k_2 + k_3 \end{bmatrix}}_{\mathbf{K}} \begin{bmatrix} x_1 \\ x_2 \end{bmatrix} = \mathbf{0}_{2x2} \tag{2.29}$$

The unknowns x_1 and x_2 can be expressed as a vector, $\mathbf{x}$.

$$\mathbf{x} = \begin{bmatrix} x_1 \\ x_2 \end{bmatrix} \tag{2.30}$$

The solution of (2.29) can be assumed to be

$$\mathbf{x} = \Re\{\tilde{x}e^{i\omega t}\} \tag{2.31}$$

Here $\tilde{x}$ is a vector of unknown complex constants. It will be interesting to find the nonzero solutions for $\mathbf{x}$, which are true for all times t. This can be obtained as long as (2.32) is fulfilled, which is obtain by combining (2.29), (2.30) and (2.31).

$$\det(-\omega^2\mathbf{M} + \mathbf{K}) = 0 \tag{2.32}$$

This is called the *characteristic equation*, which can be solved for two values of ω^2. The eigenfrequency of the system is defined as ω, and is then simply the square root of the eigenvalues. For MDOF systems, the the knowledge about the eigefrequencies could give an indication on how the system will behave.

2.6 Scaling Laws

The reason for performing experimental testing is to obtain design data to verify the performance of actual marine structures, verification and calibration on theoretical methods and numerical codes, and understand the physical problem better (Steen 2014). This is done by performing model tests, where a full-scale physical model is recreated on a smaller scale. To obtain the model scale, scaling laws are applied. The scaling laws should ensure the physical model in the model scale accurately represents the behavior and performance. Therefore, three criteria must be fulfilled: geometrical, kinematic, and dynamic similarity.

The geometrical similarity should ensure that the proportions and dimensions of the model should be scaled down consistently from the full-scale model. The ratio between lengths and shapes should be the same in both sizes. Kinematic similarity requires that the velocity keeps the same ratio. Lastly, the dynamic similarity is related to the forces acting on the structure. Forces that could occur are inertia, viscous, gravitational, pressure, elastic, and surface forces. These must be scaled correctly, achieving the same ratio between the forces in the model scale and the full-scale model.

Further, dynamic similarity can be obtained by common methods in hydrodynamic modeling: Froude and Reynolds scaling. However, these methods can not be simultaneously satisfied. Froude scaling uses similarities in gravity and inertia forces to obtain the same Froude Number, F_N (), see (2.33). Reynolds scaling wants to maintain the same ratio of viscous forces by keeping the kinematic viscosity constant for both model and full-scale structures. When Reynold scaling is applied, the same Reynolds Number is wanted, as in (2.34)

$$\frac{F_i}{F_g} = \frac{\rho U^2 L^2}{\rho g L^3} = \frac{U^2}{gL} \quad \rightarrow \quad \frac{U_M}{\sqrt{gL_M}} = \frac{U_F}{\sqrt{gL_F}} = F_N \tag{2.33}$$

$$\frac{F_i}{F_v} = \frac{\rho U^2 L^2}{\mu U L} = \frac{\rho U L}{\mu} = \frac{UL}{\nu} \quad \rightarrow \quad \frac{U_M L_M}{\nu_M} = \frac{U_F L_F}{\nu_F} = Re \tag{2.34}$$

Which method is most correct depends on the problem. If the structure is heavily affected by gravity waves, gravity forces will dominate, and Froude scaling should be preferred. In another case, if Reynolds number would be preferable if the wind force dominates, which could be the case for windmills.

Chapter 3

Model definition

The upcoming chapter will explain the experiments and the numerical modeling. However, there are many similarities in these sections. It was early decided that some existing models should be used in the experiments. These were made during a previous master's thesis conducted by Onsrud (2019). Therefore, using the full scale values of these models in the simulator in this thesis was natural, which made it directly possible to compare the results from the simulator and experiment. However, this chapter will also present the different cases that are tested and simulated, how the mooring stiffness is decided, and what connector stiffness is used.

A sketch of the module is shown in Figure 3.1. The full scale and model scale dimensions and further characteristics are defined in Table 3.1. To obtain the model scale values Froude scaling is applied.

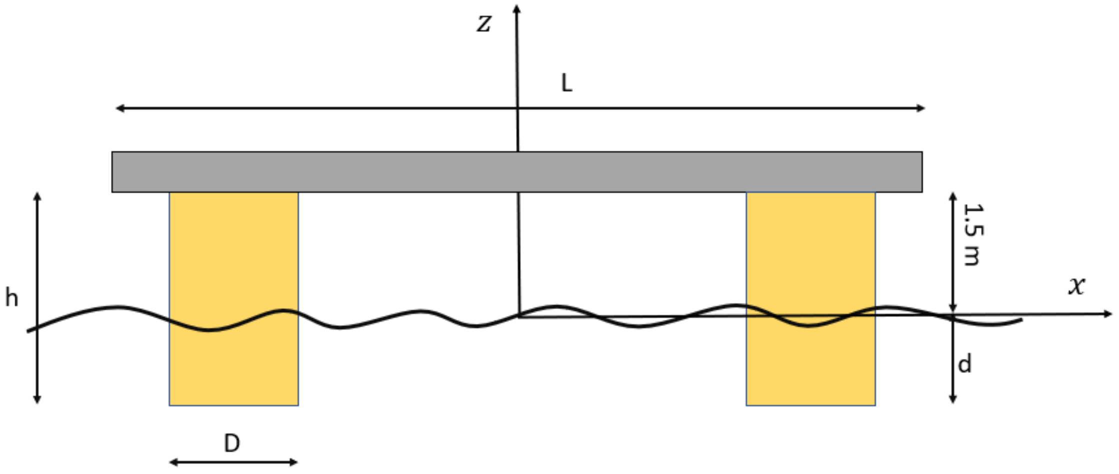

Figure 3.1: Characteristics of module

It is further important to note that the vertical center of gravity (VCG) is located 2.44 meters above the bottom of the pontoon in dry condition. While the center of gravity (COG) will be located at $z = 1.31m$, in the body-fixed coordinate system.

Table 3.1: Module dimensions for model scale

Description	**Parameter**	**Model scale**	**Full scale**
Length	L	600.0 [mm]	12 [m]
Width	B	600.0 [mm]	12 [m]
Pontoon diameter	D	80.0 [mm]	1.6 [m]
Draught	d	56.6 [mm]	1.13 [m]
Pontoon height	h	131.5 [mm]	2.63 [m]
Module mass	M	1.136 [kg]	9088 [kg]
Vertical centre of gravity	VCG	0.122 [mm]	2.44 [m]
Mooring line spring stiffness	k_s	7 [N/m]	4280 [N/m]
Distance between modules	k_s	66.4 [mm]	1 [m]

3.0.1 Test cases

Due to the number of modules available in the lab and limited free space in the wave tank, four test cases have been conducted. The limited space in the wave tank was, amongst other things, a reason to not conduct testing with modules in multiple directions. Therefore, only testing with modules in one direction is performed. In *Case 1*, only one module is observed. In *Case 2*, *Case 3*, and *Case 4*, the series of modules is expanded to two, three, and five modules. In these cases, the first and last modules are moored. Further, the modules are connected with a connector. Since there is only one line of modules in these cases, the modules are defined after their position in the line. Module 1 is defined as the module closest to the wave maker, while Module 5 is the one furthest away.

3.0.2 Mooring system

One of the cases that seemingly has a large effect on the system is the mooring system. This could be an important topic for Multi-Module Structures. However, in this thesis, some simplification was made. Before the experiments were performed, some assumptions in the simulator were defined. One was to achieve an eigenperiod in surge outside the range of wave periods. This meant that the wanted eigenperiod was 60 seconds. This would equal a mooring stiffness of 500 N/m in full scale. Further, simulations with connector stiffness in the range from 100 N/m to 10000 N/m were performed. This would help to decide in what range the stiffness should be in the experiment. However, some assumed numerical issues occurred when the stiffness was between 5000 - 10000 N/m. The surge motion is expected to oscillate about zero. However, with a connector stiffness between 10 and 20 times, the mooring stiffness moved their oscillation point. Simulations with connector stiffness between 250 - 3000 N/m produced the expected results.

Before starting the experiment, there were uncertainties about how soft springs were available. However, the softest spring was later found to be 7 N/m, which equals 2800 N/m at full scale. In the experimental setup, the mooring system was originally designed so the mooring lines were at a 45° angle to the wall. For one module, this equaled an eigenperiod of 8.7 seconds. This is problematic because waver periods frequently occur in this range. To increase the eigenperiod, the mooring line angle was lowered to 22.5°. This gave different mooring stiffness in surge and sway equaled 4280 N/m and 10348 N/m. As the motions in surge were of interest, the stiffness could be higher in sway. The eigenperiod for one module in surge became then 11.94 seconds. This is still in the range of wave periods, but because of limitations in the wave tank, the upper limit of wave periods was around 8 seconds. It was therefore concluded that the system's eigenperiod would not affect the response of the modules too much.

To decide the rotational stiffness in yaw, it was found geometrically from the experiment setup. The first thing was to measure the initial values, i.e., lengths of the mooring line from the wall tank to the module and the attacking angle of the line. In the initial state, the yaw angle is zero, and by changing the heading of the module, the mooring line and angle would differ. As previously mentioned, a spring is attached at the end of the mooring line to obtain a mooring in surge and sway and later given some pretension. Using the force from the mooring lines to calculate the moment acting on the module for different angles, it is possible to find a slope depending on these variables. The slope will then have the units [N/deg] or [N/rad] and be the stiffness in yaw. The final mooring stiffness for surge, sway, and yaw are summarized in Table 3.2.

Table 3.2: The final mooring stiffness for surge, sway and yaw used in the simulator

DOF	Stiffness	Unit
Surge	4280	[N/m]
Sway	10348	[N/m]
Yaw	15839	[N/m]

3.0.3 Connectors

An important part of the experiments is to use different types of connectors. However, obtaining the correct stiffness is the same as the mooring stiffness. The planned connector stiffness was not obtainable, meaning it was necessary to use what was found. In the experiment, the connector is represented by overstretched extension springs. The springs were stretched, so it was possible to handle both compression and tension. The process of how this was done will be explained in the experimental chapter. However, the process resulted in four different connector types. The full-scale stiffness was arranged in ascending order as follows: 6381 N/m, 14899 N/m, 26259 N/m, and 29332 N/m.

Further, there are some difference in the simulator and models in the experiment. In the simulator the connectors are one meters and placed in the corners on the modules. While on the modules, the connector is placed a bit into the plate on top of the module. This is due to the insecurities in the creation of the springs used in the experiment. This will be further commented in the experimental chapter.

Chapter 4

Methodology

The numerical model was first developed during a related Project Thesis in the Fall of 2022. The aim is to create a model that could replicate the results from the experiment. The hydrodynamic analysis of the modules is performed with WADAM. Which uses potential flow theory and linear wave theory to calculate the hydrodynamic coefficients and forces. This would make it possible to use the simulator to test instead of performing new experiments for new test scenarios, as this could be expensive and time-consuming. However, at the beginning of the master thesis, some new changes were implemented. This yields the drag term from the Morison equation, rotation matrix (2.11), and expansion from one to two connection points. In the last part of this Chapter, a method to switch the stiffness of the connectors is proposed. This is however only numerical, and not tested in the experiment.

4.1 Numerical model

4.1.1 Network Model

As defined in chapter 3, the test cases will only consist of modules in one direction. This means that except of Module 1 and the last module, the other ones will be connected to two other modules. Further, the reference frames used in the model must be defined. For each of the modules i, a local coordinate system ($x_{b,i}$,$y_{b,i}$,$z_{b,i}$) is defined with an origin in the CG at the water plane. This will coincide with the body-frame defined in Chapter 2.2.1. The global coordinate system (X, Y,Z) is defined in the origin of Module 1, with the vertical point located at the water plane. The Z-axis is defined upwards, and thence from the right-hand rule, the X-axis is defined forward, and Y-axis is defined to the port.

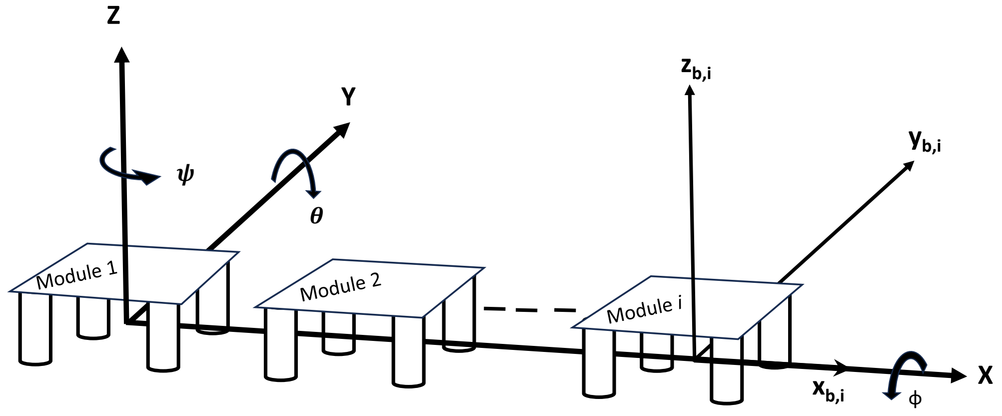

Figure 4.1: Sketch of coordinate systems

Here the translational global motions can be defined in a vector $\boldsymbol{\chi_1} = [X, Y, Z]^T$ and the angles in $\boldsymbol{\chi_2}$= $[\phi, \theta, \psi]^T$.

In general, multiple ways exist to connect the modules, defined by the modules and the configurations. Only modules in one direction are looked at for the cases in the thesis. This simplifies the modeling, but which connected modules must still be defined. A common way to present this is with a topology matrix, Φ, as in (4.1). Here Case 4 is presented. Φ_{ij} is set to 1 when two modules are connected. Otherwise, it will be set to 0.

$$\Phi = \left[\begin{array}{cccccc} & \mathbf{1.1} & \mathbf{1.2} & \mathbf{1.3} & \mathbf{1.4} & \mathbf{1.5} \\ \mathbf{1.1} & 0 & 1 & 0 & 0 & 0 \\ \mathbf{1.2} & 1 & 0 & 1 & 0 & 0 \\ \mathbf{1.3} & 0 & 1 & 0 & 1 & 0 \\ \mathbf{1.4} & 0 & 0 & 1 & 0 & 1 \\ \mathbf{1.5} & 0 & 0 & 0 & 1 & 0 \end{array}\right] \tag{4.1}$$

4.1.2 Equation of motion

An advantage of creating a large structure with multiple modules is that the hydrodynamic effects on the modules are the same. Hence, there is only necessary for hydrodynamic analysis on one module. The results can then be used in all cases of different connector stiffness. The governing equation for one module can be written as

$$(\boldsymbol{M}+\boldsymbol{A})\ddot{\eta}+\boldsymbol{B}\dot{\eta}+\boldsymbol{C}\eta = \boldsymbol{F_j^{exc}}+\boldsymbol{F_j^{mooring}}+\boldsymbol{F_j^{C}}+\boldsymbol{F_j^{drag}} \quad for \quad j=1,2,...,6 \tag{4.2}$$

The hydrodynamic coefficients added mass matrix, $\boldsymbol{A} \in \mathbb{R}^{6x6}$, damping matrix,$\boldsymbol{B} \in \mathbb{R}^{6x6}B$, hydrostatic stiffness matrix, $\boldsymbol{C} \in \mathbb{R}^{6x6}$, and the excitation loads, $\boldsymbol{F_j^{exc}}$, are retrieved from calculations performed in Chapter 4.1.3. The remaining terms on the right side are the mooring force, $\boldsymbol{F_j^{mooring}}$, connector force, $\boldsymbol{F_j^{C}}$, and drag force, $\boldsymbol{F_j^{drag}}$. These will be explained in the next chapters.

Mooring Force

Further, the mooring system that is applied to the modules will restrain them from drifting off. The mooring force depends on the motion of the modules, and the force can hence be simplified as

$$\boldsymbol{F_j^{mooring}} = -\boldsymbol{J}(\boldsymbol{\eta_2})^{\boldsymbol{T}} \boldsymbol{C_{mooring}} \eta_j \tag{4.3}$$

Here $\boldsymbol{C_{mooring}}$ is a 6x6 matrix, with stiffness applied by the mooring in surge, sway, and yaw. There is no applied mooring in roll, pitch. or heave.

Connector Force

Following the assumption that the modules are rigid bodies, the placement of the connectors will not change. However, the relative position between two modules will change, which must be accounted for when calculating the connector force. Each module has two connectors on each side. For simplification, the method of calculating forces is done with two modules, Module m and Module n.

In still water, the origin of the modules can be defined in the local reference frame as

$$\begin{aligned} \boldsymbol{X_{0m}^{b}} &= [x_{0m}^b, y_{0m}^b, z_{0m}^b]^T \\ \boldsymbol{X_{0n}^{b}} &= [x_{0n}^b, y_{0n}^b, z_{0n}^b]^T \end{aligned} \tag{4.4}$$

Here 0 indicates that still water position. It will be equivalent to Module n. Further, will each of the modules have a position in the global reference frame, given as

$$\begin{aligned} \boldsymbol{\chi_m} &= [\boldsymbol{\chi_{m,1}} + \boldsymbol{X_{0m}^{b}}, \boldsymbol{\chi_{m,2}}] \\ \boldsymbol{\chi_n} &= [\boldsymbol{\chi_{n,1}} + \boldsymbol{X_{0n}^{b}}, \boldsymbol{\chi_{n,2}}] \end{aligned} \tag{4.5}$$

As there are eight possible connection points, two on each side, Figure 4.2. When a connector is placed between Module m and Module n, as in Figure 4.3, Module m will have connection points in 2.1 and 2.2. Module n will correspondingly have connection points in 4.1 and 4.2.

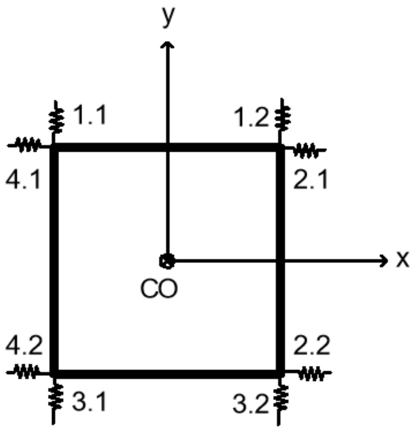

Figure 4.2: Connection points on one module

The connection points can be described at vector form and will then have the following location in the global reference frame,

$$\begin{aligned}\boldsymbol{P^g_{m,2.1}} &= \boldsymbol{\chi_{m.1}} + \boldsymbol{R}(\boldsymbol{\chi_{m.2}})\boldsymbol{P^b_{m,2.1}} & \boldsymbol{P^g_{m,2.2}} &= \boldsymbol{\chi_{m.1}} + \boldsymbol{R}(\boldsymbol{\chi_{m.2}})\boldsymbol{P^b_{m,2.2}} \\ \boldsymbol{P^g_{n,4.1}} &= \boldsymbol{\chi_{n.1}} + \boldsymbol{R}(\boldsymbol{\chi_{n.2}})\boldsymbol{P^b_{n,4.1}} & \boldsymbol{P^g_{n,4.2}} &= \boldsymbol{\chi_{n.1}} + \boldsymbol{R}(\boldsymbol{\chi_{n.2}})\boldsymbol{P^b_{n,2.2}}.\end{aligned} \tag{4.6}$$

Here the $\boldsymbol{R}()$ is the rotation matrix as from (2.11). Further, by obtaining connection points on each module, the elongation of the connector can be obtained. This is found first by finding the length of the connector in still water, and further during change. It can be obtained from

$$\begin{aligned}\boldsymbol{l_{0,1}} &= \boldsymbol{P^g_{0m,2.1}} - \boldsymbol{P^g_{0n,4.1}} & \boldsymbol{l_1} &= \boldsymbol{P^g_{m,2.1}} - \boldsymbol{P^g_{n,4.1}} \\ \boldsymbol{l_{0,2}} &= \boldsymbol{P^g_{0m,2.2}} - \boldsymbol{P^g_{0n,4.2}} & \boldsymbol{l_1} &= \boldsymbol{P^g_{m,2.2}} - \boldsymbol{P^g_{n,4.2}}\end{aligned} \tag{4.7}$$

Here the still water connection points are used to obtain the initial length of the connector. Further, the force in the connector can be obtained from Hooke's law. For connector 1 between Module m and Module n, the force is given as

$$\boldsymbol{f_{n,2.1}} = -k_C(\boldsymbol{l_1} - \boldsymbol{l_{0,1}}) \tag{4.8}$$

Where k_C is the connector stiffness. Which is put equal in all directions. The force acting on Module m must also act on Module n, but with the opposite direction, hence $f_{m,4.1}$ = -$f_{n,2.1}$. From the connector forces, a moment about the CO will be imposed. The arm from the CO of Module n to connection point 2.1 is found as

$$\boldsymbol{r_{n,2.1}} = \boldsymbol{P^g_{n,2.1}} - \boldsymbol{\chi_{n,1}}. \tag{4.9}$$

This is found in the same way for the other connection points and Module n. Further, is the moment seen as

$$\boldsymbol{m_{n,2.1}} = \boldsymbol{r_{n,2.1}} \times \boldsymbol{f_{n,2.1}} \tag{4.10}$$

For each of the module's connection points, the force and moments acting from these can be defined as $\boldsymbol{F_{n,c}} = [\boldsymbol{f_{n,c}}, \boldsymbol{m_{n,c}}]^T$. The total force acting on one module will be the sum of the force and moments from all the connectors. This is can be given as

$$\boldsymbol{F^C} = \sum_{c=1}^{8} \boldsymbol{F_c} \tag{4.11}$$

Where c represent the eight connection points. The resulting force from (4.11) is the force that is used as $\boldsymbol{F^C}$ in the equation of motion given by (4.2). If no modules are next to each other, the connector force will be zero.

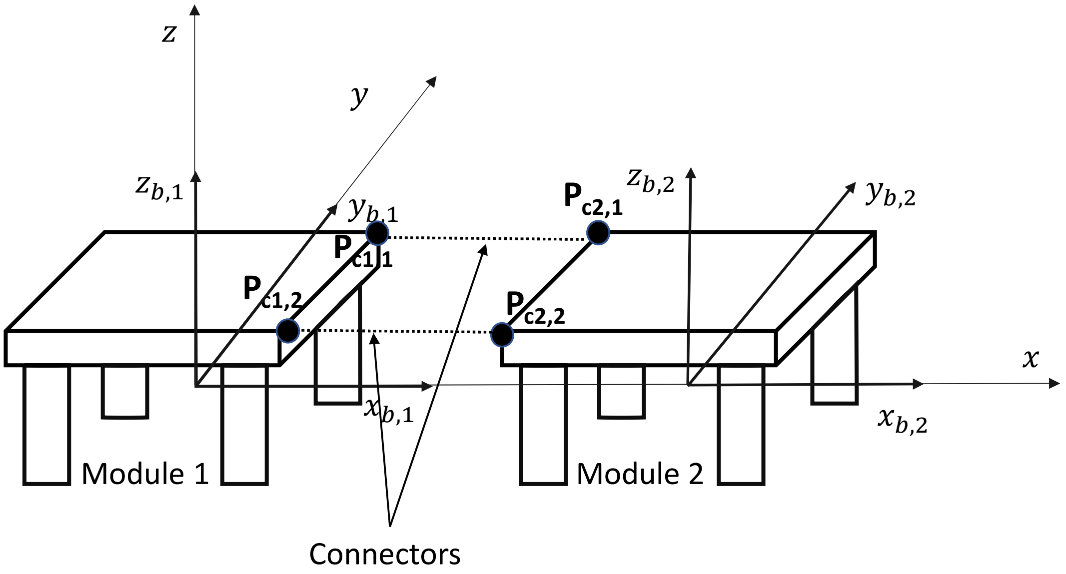

Figure 4.3: A sketch of two modules in a global coordinate system

Drag Force

The drag force is calculated using the drag term from the Morison equation. The mass terms are included in the excitation force, and hence not calculated twice. For each module, the drag force is calculated independently on each leg. The relative motion in the XY-plane is accounted for by updating the global position of the pontoons. However, the change in draught is not accounted for. The remaining part of the Morison equation will be as follows,

$$dF = \frac{1}{2} C_D D (u - \dot{\eta})|u - \dot{\eta}| dz. \tag{4.12}$$

Here, the terms are the same as defined in (2.22). In the simulator, C_D is set to be 1.

4.1.3 Sesam HydroD and Genie

The added mass, damping, hydrostatic restoring, and excitation force are obtained by solving the diffraction and radiation problems, as explained in Chapter 2.2.2. However, to solve these problems the softwares HydroD and Wadam from Sesam are used. Wadam is based on linear wave and potential flow theory, which has been earlier explained in chapter 2. It is further possible to apply second-order forces with Wadam, however, this is not been included in this thesis.

However. before the matrices could be found, the module was modeled in GeniE, another software from Sesam. Here, only the pontoons were modeled, as seen in Figure 4.4a. This is because only the pontoons of the module interact with the water surface. Further, the pontoons dimensioned after the full scale values given in Table 3.1. The CO and COG is both located at the centre of the module in the XY-plane. While the CO is placed on the still water line, the VCG is located 1.31 meters above.

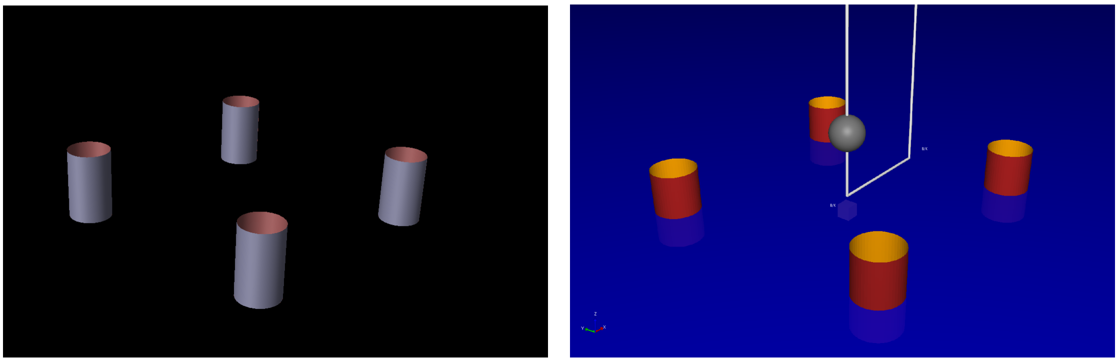

(a) Pontoons modeled in Sesam GeniE

(b) Pontoons when exported into HydroD

Figure 4.4: The modeling of the pontoons

When the analysis in Wadam was performed, the wanted coefficients and forces for different wave periods and wave headings could be obtained. The excitation force can be given either as a complex number or an amplitude, A, with the corresponding phase, θ. Here the latter method is used, hence the excitation force can be presented as

$$F_j^{exc} = A_j \cos(\omega t - kx + \theta) \tag{4.13}$$

Where ω is the angular wave frequency, k is the wave number and x is the global position of the module. Since only waves propagating in the positive x-direction are of interest in this thesis, there will be no waves propagating in the y-direction. The resulting motion from Wadam can be given as

$$\eta_j = \eta_{a_j} \cos(\omega t - kx + \theta) \tag{4.14}$$

4.1.4 ODE solver

To simulate the motion of the module over time, it is necessary to solve the equation of motion given for the system (2.17). As the equation of motion is given as a second-order differential equation, it has been reduced into two first-order ordinary differential equations(ODE). This is done by first putting the velocity, ν, as the derivative of the position, η. The second first-order ODE is given by rearranging the system's equation of motion so the acceleration can be calculated.

$$\ddot{\eta} = (\boldsymbol{M}+\boldsymbol{A})^{-1}(\boldsymbol{F_j^{exc}} + \boldsymbol{F_j^{mooring}} + \boldsymbol{F_j^{C}} - \boldsymbol{B}\dot{\eta} - \boldsymbol{C}\eta) \quad for \quad j = 1,2,...,6 \tag{4.15}$$

It was so further defined that $F = \boldsymbol{F_j^{exc}} + \boldsymbol{F_j^{mooring}} + \boldsymbol{F_j^{C}}$. The system is then defined by the two first-order ODEs given in (4.16).

$$\nu = \boldsymbol{J}(\eta_4, \eta_5, \eta_6)\dot{\eta} \tag{4.16a}$$

$$\ddot{\eta} = \dot{\nu} = \boldsymbol{M^{-1}}(\mathbf{F} - \boldsymbol{B}\nu - \boldsymbol{J}(\eta_4, \eta_5, \eta_6)^T\boldsymbol{C}\eta) \tag{4.16b}$$

Here $\eta = [\eta_1,...,\eta_i]^T$, $\nu = [\nu_1,...,\nu_i]^T$ and $\mathbf{F} = [F_1,...,F_i]^T$ for i = 1,..,6. While the matrices $\boldsymbol{M}$, $\boldsymbol{B}$, and $\boldsymbol{C} \in \mathbb{R}^{6x6}$ and is the same matrice as in (4.2). To initiate the function, a set of initial values is necessary. Since the system is 6DOF there will be twelve initial values, six related to the translations and rotations, and six to the linear and angular velocities. The initial values for the velocity, $\boldsymbol{\nu_0} = \boldsymbol{\nu(t = 0)}$ were set to be zero in all directions. This implies that the positional initial values, $\boldsymbol{\eta_0} = \boldsymbol{\eta(t = 0)}$ should be the maximum value of η_j from (4.14). This was obtained by setting t = 0.

$$\begin{aligned} \boldsymbol{\nu_0} &= [\nu_{0,1}, \nu_{0,2}, ..., \nu_{0,3}]^T \\ \boldsymbol{\eta_0} &= [\eta_{0,1}, \eta_{0,2}, ..., \eta_{0,3}]^T \end{aligned} \tag{4.17}$$

Solving these two first-order DOFs makes getting the module's motion possible. To accomplish this task, a numerical integrator was utilized. As the simulator was created using Python, the SciPy package was accessible. The SciPy packages provide different methods to solve ODEs. In this case, *solve_ivp* was chosen. It offers multiple methods to solve ODEs, including different orders of the Runge-Kutta method and BDF. This makes solving stiff and non-stiff problems solvable if the correct method is chosen during the simulation. There were no indications that the problem was stiff, so *RK45* is used during the simulations.

Multiple different simulations were performed. However, it is only necessary to simulate until a steady state. Therefore, the simulation was stopped after 600 seconds. The time step used in the simulation was 0.01 seconds.

4.2 Control Logic

The final aim of this thesis is to devise a control logic that specifies when the transition between different stiffness levels should occur. This would be beneficial to reduce the motion of the modules and the force that occurs in the connections. The high motion would not be beneficial, as it could lead to a collision between the modules and higher connection forces. If the force exceeds its limit, the construction will be destroyed. However, it is important that the switching is performed properly. Using automatic switching between different states, as it will with this logic, could lead to switching during transients and chattering (Sørensen 2018). The risk during transients might lead to instability because switching between states is performed incorrectly. In the other case, chattering occurs when the logic switches back and forth between two states. In order to achieve a stable state, it is necessary to delay the switching process. Chattering could occur when the wave period changes and a transient state arise. To avoid these problems, a delay in the switching can be implemented. Known methods are dwell-time dynamics or hysteresis, illustrated in Figure 4.5.

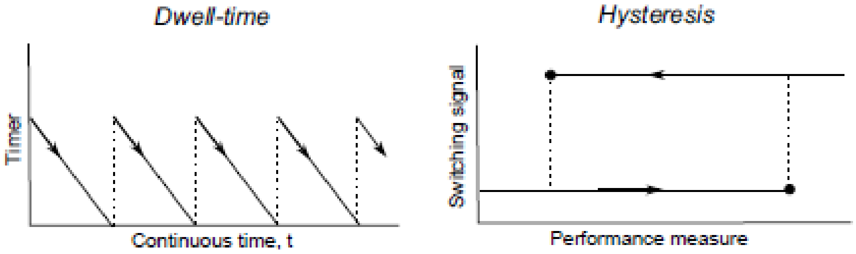

Figure 4.5: Dwell-time is illustrated to the left, and hysteresis to the right Sørensen (2018)

The dwell-time constraint is based on a prespecified timer that allows the switching between states to happen when it ends. If a change implies a switch between states, it could only happen when the timer reaches zero. This might lead to unacceptable behavior in the system before a switch is permitted (Hespanha et al. 2003). While hysteresis, the system will switch between states depending on some variable. The switch will not occur before the variable is inside some threshold.

4.2.1 Implementation in the Numerical Model

In this control logic, a variant of the hysteresis will be implemented. Assuming that the largest frequency that affects the signal retrieved from the surge motions will correspond to the wave frequency, a change in the motion frequency will indicate a change in the wave frequency. When a change in the motion frequency is detected, the frequency is stored each 25 seconds. When the last two frequences is below a threshold of 0.001, a switch will be forced. The best-suited connection stiffness can be chosen using the latest recorded motion frequency.

Chapter 5

Experiments

This chapter will detail the experiment conducted in the lab, including the post-processing of results. The study was conducted in collaboration with Ph.D. student Trine Aas-Hansen. The experiment was carried out at the end of March and throughout April of 2023 at the Department of Marine Technology Center in Trondheim Tyholt.

The experiment serves two main purposes. Firstly, it aims to observe how a flexible connector's stiffness affects the connected modules' behavior. Secondly, the results will validate those obtained from the simulator. This chapter will provide information on the lab facilities, experimental setup, instrumentation, error sources, and a discussion on the choice of connectors.

5.1 Lab facilities

The experiments were carried out in Lilletanken, one of the Marine Technology Center labs. The tank used for the experiment is 25 meters long, 2.5 meters wide, and had a water level of approximately 0.7 meters. A bird's-eye view of the tank is shown in Figure 5.1. In addition, the water density was assumed to be 1000 kg/m^3. The wavemaker is located on the right side of the tank, while a parabolic beach is placed on the opposite end to minimize wave reflections from the end wall.

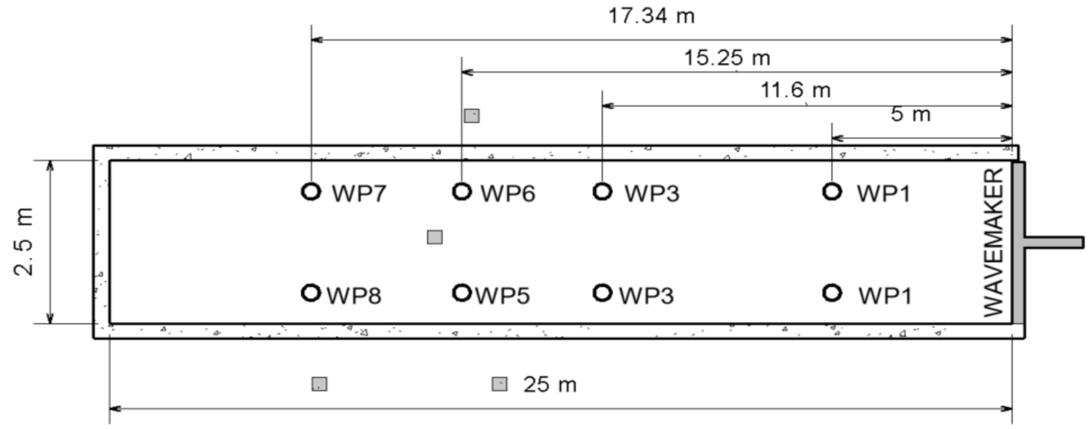

Figure 5.1: Setup and the dimension of Lilletanken without modules.

5.1.1 Instrumentations

To accurately obtain and process the results of the experiments, it is crucial to have the appropriate instruments. The instruments used in this experiment are the Qualisys Oqus, wave probes, and load cells.

Qualisys Oqus

Qualisys delivers multiple cameras type for tracking off objects. In this experiment, the Oqus cameras were used. By placing spherical reflectors on the model, the camera can follow the movement of the module. In this experiment, each module had four reflectors in different locations. It was then possible to measure the motions of the modules in six degrees of freedom. Another option could have been to track only three degrees of freedom. To begin tracking the module, the first step was to locate it. There were a total of five modules, each with its own unique local coordinate system. For accurate measurements, it was required to use a minimum of two cameras. Here, four cameras were used, and their locations are represented by the grey boxes in Figure 5.1. It is also necessary that the cameras have a clear vision of the reflectors, or else the quality of the measurements could decrease.

The residual is a factor that describes how good the measurements are, and the goal was to have it below one *mm*. If the reflector is wide in the camera angle, this could affect how well the motions could be captured. Other factors could be the number of bodies, i.e., multiple modules with reflectors close to each other, mooring piles shadowing for the camera, or water reflections. To minimize uncertainties caused by having five modules, we adjusted the camera angle during the experiment to ensure that all cameras captured the entire model.

Wave probes

Eight different wave probes were placed in the tank, with positive directions upwards. The first two wave probes, *wp1* and *wp2* were placed five meters from the wave-maker. *wp3* and *wp4* was further placed ten meters from the wave maker. Since the center of the connected modules could change on how many modules, *wp5* and *wp6* had different locations. However, they should be aligned with the geometrical center of the connected modules. The last two wave probes, *wp7* and *wp8*, were placed behind the module. The location of the wave probes is also shown in Figure 5.1.

Load cells

To measure the force in mooring lines and in the connectors, load cells was used. Here, two different types was used. A circular load cell was attached to the mooring line's end. This was low weight and could easily be attached and detached. It was located along the tank wall, after the pulley, and before the spring. A load cell formatted as a bar was used to measure the force acting in the connectors. This can be seen on the left in Figure 5.2b. With this type of load cell, only the axial forces was measured.

5.2 Scaling laws

The model scale modules are 1:20 of the full-scale models. It is further assumed that gravity-driven waves will be the governing environmental load on the modules. Hence, Froude scaling would be applicable. It is further assumed that the water densities in full-scale and model scale are equal. The scaling parameters are presented in Table 5.1.

Table 5.1: Froude scaling law parameters, where $\lambda = L_F/L_M = 20$ and ρ_M and ρ_F are fluid density for the model and full-scale objects.

Physical parameter	Unit	Multiplication Factor
Length	[m]	λ
Structural mass	[kg]	$\lambda^3 \frac{\rho_F}{\rho_M}$
Force	[N]	$\lambda^3 \frac{\rho_F}{\rho_M}$
Moment	[Nm]	$\lambda^4 \frac{\rho_F}{\rho_M}$
Stiffness	[N/m]	$\lambda^2 \frac{\rho_F}{\rho_M}$
Acceleration	[m/s^2]	$a_F = a_M$
Time	[s]	$\sqrt{\lambda}$

5.2.1 The Models and Case Definitions

The cases were roughly described in chapter 3, here a more detailed description will be given for the experiment. As mentioned, the model scale modules already existed. The floating elements are created by divynicell foam material, while the plate is made of a light honeycomb material to ensure lightweight. In the original problem, the modules were hinged together, as seen in Figure 5.2a. The purpose of these hinges was to isolate a single degree of rotation, allowing relative pitch and heave motion without any significant friction. In this experiment, the connectors have been modified. The hinges are replaced with a flexible connector, in the form of an extension spring. The extension spring, with how it is connected to the module, can be seen in Figure 5.2b. In the next chapters, a description of the different tests performed in the experiment.

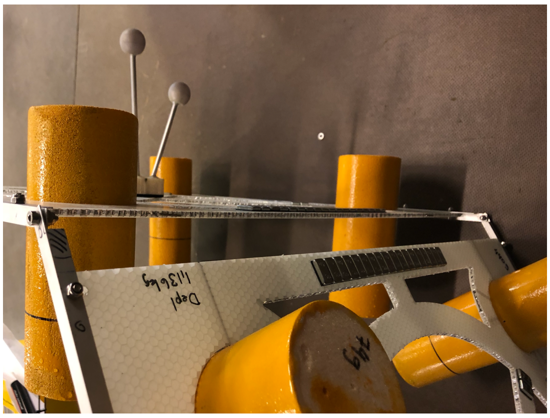

(a) Connection between modules in (Onsrud 2019)'s thesis

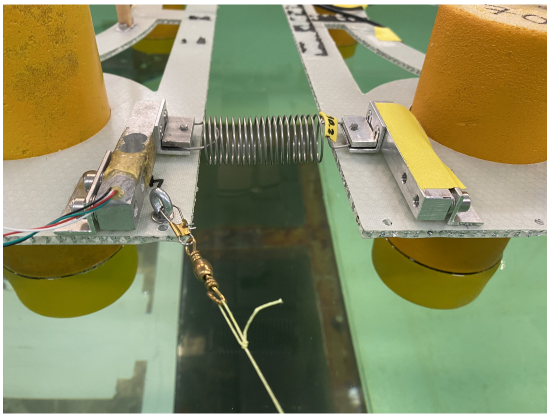

(b) Connection between modules used in this thesis.

Case 1

In the first case, where only one module was observed. The module was moored with four mooring lines, each line placed in a corner. To obtain an eigenperiod in surge that did not coincide with the incoming wave periods, the mooring lines were adjusted so each line created a 22.5° angle. The module was placed in the pit center at 15.25 m, as shown in Figure 5.3. This was to make sure that the reflecting waves would not make too much disturbance on the module during the test.

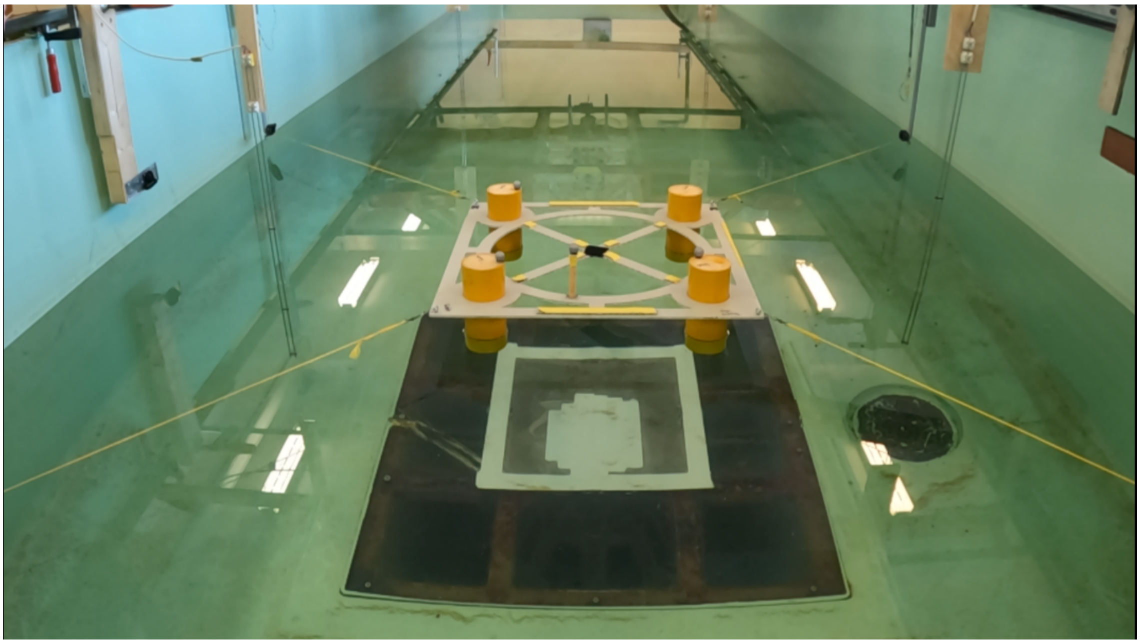

Figure 5.4: One module in Lilletanken from the front

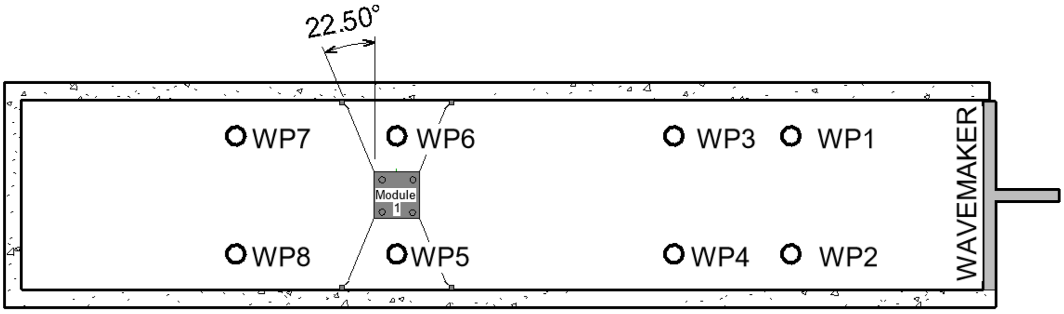

Figure 5.3: Setup in Lilletanken with one module. Not in scale.

Case 2

In the second case, a second module is connected to the first one, placed in the same location as in Case 1. Module 1 is then placed closer to the wavemaker. Here both of the modules are moored, with 22.5° angled mooring lines. This is visualized in Figure 5.5. The mooring line on the second module was attached below the plate to avoid disturbance from the two modules' mooring lines touching each other. Between the plates of the two modules, there is a gap of 66.4 mm. Further, was two load cells placed on Module 1 in the connection points. These were placed with a little gap to the plate, avoiding some forces taken up from the plate. In Figure 5.5, the finalized setup in the lab for Case 2 is shown.

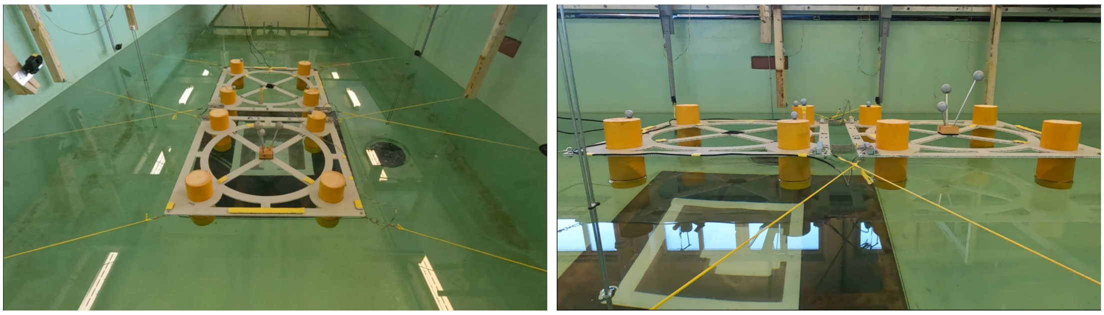

(a) The 2x1 setup from the front (b) The 2x1 setup from the side

Figure 5.5

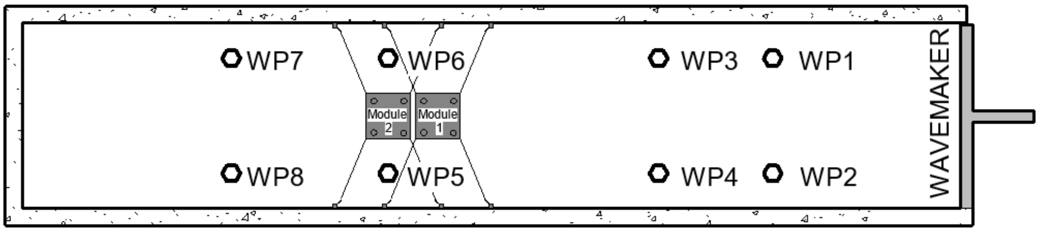

Figure 5.6: Setup in Lilletanken with two modules. Not in scale.

Case 3

In Case 3, a third module was added to Module 2, as seen from Figure 5.7. The mooring was also relocated, making Module 1 and Module 3 moored. Two new load cells were placed to track the forces in the connector between the middle and new modules. These load cells were placed on the second module. A difficulty with this setup was that two of the piles connected to the mooring lines had to be placed in the same location. However, this was solved by placing the pulleys on the same pile.

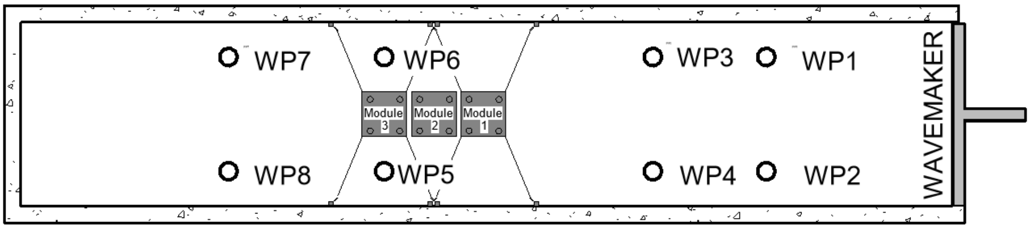

Figure 5.7: Setup in Lilletanken with three modules.

Case 4

In the last case, five modules were connected. As for Case 3, only the first and last modules are moored. In this case, the middle module will not be directly connected to any of the moored modules. This configuration can be seen in Figure 5.8. Only four load cells were available, so in this case, only one load cell was placed at the first four modules. All of them were placed on the same side, so there was no redundancy in the force measurements.

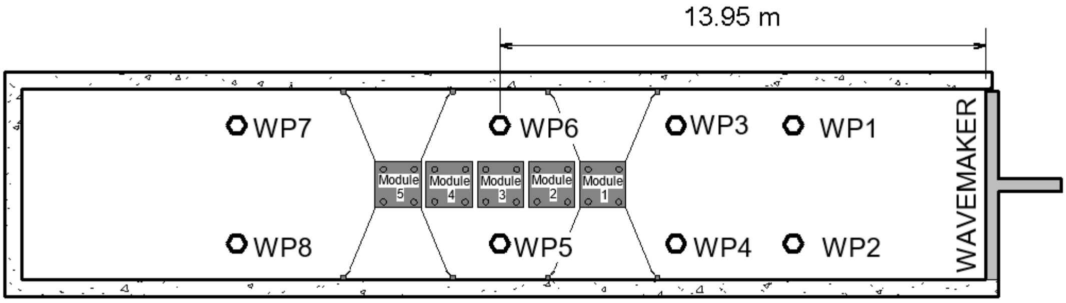

Figure 5.8: Setup in Lilletanken with five modules.

5.3 Connectors

One of the largest uncertainties in this experiment was the connector design. It was early decided that some existing modules should be modified and used in this experiment, which required that any modifications did not exceed the existing weight limit. A line was drawn on the module's pontoons, marking the water line in still water in the process of deciding upon how and what modification is necessary, meetings with the supervisor and the technical staff at Tyholt were conducted. During these meetings, several obstacles were discussed. Some of these were what kind of material should be used for the connector, what type of design, how small can the stiffness of the connector be, how can the connector be attached to the module, and is it possible to measure the force in the connectors.

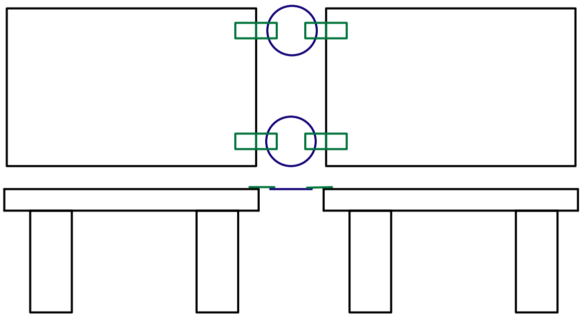

Figure 5.9: Principle Sketch of the first connection draft

The first connector design is sketched in Figure 5.9. It's a ring placed horizontally between the modules. Because of the circular form, it was expected that it was expected to have compression and tension effects. It was further suggested to either use tubes of PVC material or steel wire. Using PVC tubes and dividing them into rings would be a cheaper option and was chosen. Ideally, the ring's stiffness could be changed by the ring's wall thickness, diameter, or thickness. It was planned to use piano hinges to attach the ring to the module. These were lightly weighted and permitted pitch motions. This connector was planned to be used before starting the lab. There were still some unanswered questions, like how to measure the force and the stiffness. During the first week at the lab, measurements of the rings were performed. The softest rings made of PVC ring had a stiffness above $1200N/m$. This would equal a full-scale stiffness of $480000N/m$, much larger than the calculated stiffness provided in the numerical model.

Because of the large stiffness, using PVC as a material was impossible. Instead, a 1mm steel wire was used to create the ring. The ring felt softer, and a wave test was conducted. During the test, it was observed that it was too stiff. Instead of compressing the ring, it forces the modules out of the water, as seen from Figure 5.10. This led to the second connector design, based on extension springs. Initially, the spring would have tension capabilities and would work well as the modules moved in opposite direction. However, there would be lack of restoring effects when the modules moved together. To obtain the compression ability, the spring was stretched so much it obtained a new form. The original spring would look like Figure 5.11a, while after it was stretched it would look like Figure 5.11b. However, by stretching it, the characteristics of the springs would change. The most important change was the increased stiffness. The second design is the one used in the experiment, as shown in and the process of how the spring was created will follow.

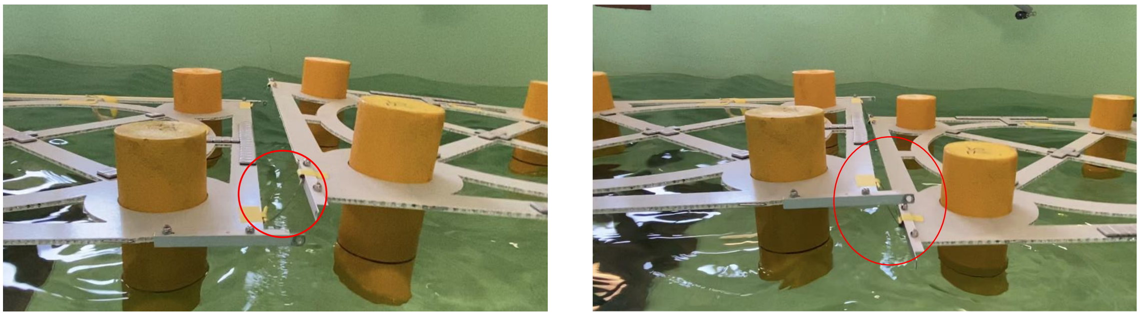

Figure 5.10: Images illustrating the problem when using the to stiff rings as connectors. They would not compress, and the other module would be lifted from the water.

Some of the springs were created with help of Sintef. To obtain the same stiffness for the same type of spring, it was recommended to create one long spring and divide it. Since creating to identical springs could be impossible for hand. The next step was then to stretch the spring. This was done by attaching a hook in the one end, and a load cell in the other. By carefully pulling the hook, the applied force could be measured by the load cell. To check if the springs characteristics had changed, the force was releaved. The last step was to divide the springs into equal pieces. As measurment, one spring was measured to be 6 cm. This would make it possible to create loops at both ends. The coils in the new spring was counted, and the new springs were divided after the number of coils. This was to ensure that the stiffness was more or less equal.

(a) Example spring before stretched

(b) Example of spring after stretched

The final connector design is shown in Figure 5.12. To measure the force acting in the spring, one load cell is placed on a module while a dummy load cell is placed on the other. The spring loop is then tightened between two plates, and a screw prevents it from being pulled out. The load cell is attached to the plate with a small gap to ensure that the force is measured by the load cell and not the plate.

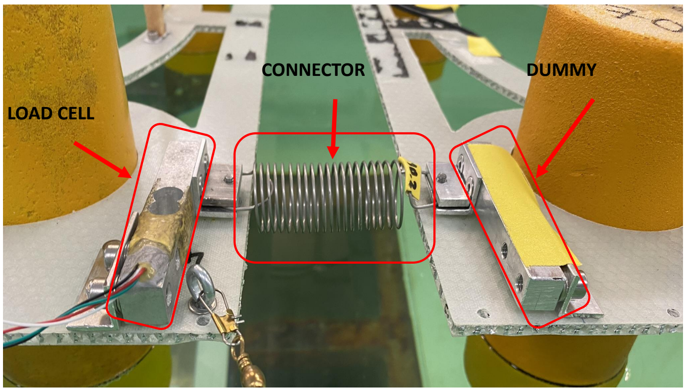

Figure 5.12: Connection between two modules, here presented with an S2 spring in between.

5.3.1 Resulting connector

Four different springs were created, one of each type is presented in Figure 5.13. At most, eight springs were used in the experiment during the wave test. Each of the different springs' tension stiffness and length is presented in Table 5.2. The tension stiffness was measured with equipment at Sintef. The compression stiffness is roughly estimated by measuring the compression with the weight applied and is presented in a full table of all the springs in Table 1. In the rest of the thesis, the springs will be referred to as *S1, S2, S3* and *S4*, corresponding to each type's average tension stiffness.

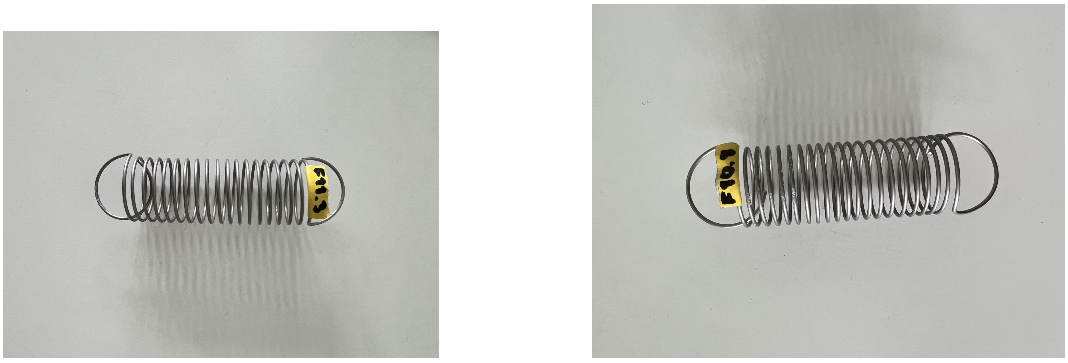

(a) Spring S1 (b) Spring S2

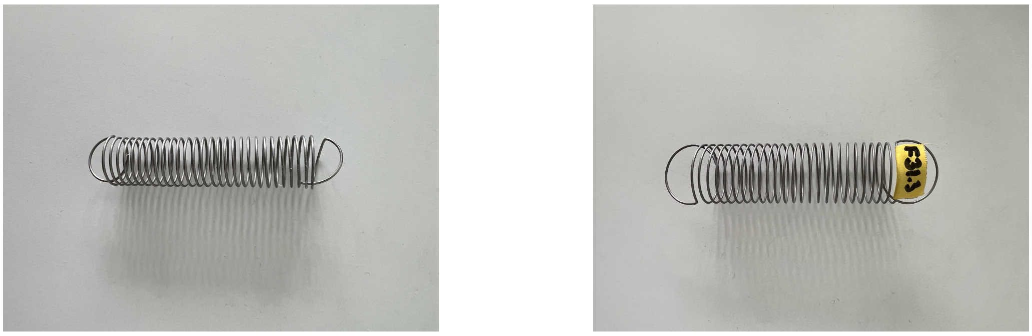

(c) Spring S3 (d) Spring S4

Figure 5.13: Examples of the four different springs used as connectors in the experiment.

Table 5.2: The resulting springs used in the experiment is presented in this table. Position is indicating where on the module and between which modules the spring was used.

Spring type	**Model scale stiffness tension [N/m]**	**Full scale stiffness tension [N/m]**	**Length [mm]**	**Position**
S1.1	71.65	28660	68.8	Left: 1 and 2
S1.2	72.07	28828	61.9	Left: 4 and 5
S1.3	76.2	30480	67.3	Left: 3 and 4
S1.4	74.09	29636	63.0	Right: 3 and 4
S1.5	72.31	28924	68.6	Right: 1 and 2
S1.6	73.09	29236	65.4	Right: 2 and 3
S1.7	73.77	29508	63.3	Left: 2 and 3
S1.8	73.45	29380	69.3	Right: 4 and 5
Average S1	**73.33**	**29332**	**66.0**	
S2.1	66.31	26524	60.1	Left: 1 and 2
S2.2	66.32	26528	60.3	Right: 1 and 2
S2.3	65.53	26212	58.5	Left: 2 and 3
S2.4	65.7	26280	60.6	Right: 2 and 3
S2.5	65.91	26364	62.2	Left: 3 and 4
S2.6	66.13	26452	61.2	Right: 3 and 4
S2.7	63.87	25548	63.4	Left: 4 and 5
S2.8	65.4	26160	63.7	Right: 4 and 5
Average S2	**65.65**	**26259**	**61.3**	
S3.1	37.19	14876	67.0	Right: 2 and 3
S3.2	37.39	14956	61.7	Left: 4 and 5
S3.3	37.41	14964	63.1	Right: 1 and 2
S3.4	37.46	14984	63.1	Left: 1 and 2
S3.5	37.55	15020	67.0	Left: 2 and 3
S3.6	37.78	15112	65.0	Right: 4 and 5
S3.7	36.42	14568	68.3	Right: 3 and 4
S3.8	36.77	14708	67.0	Left: 3 and 4
Average S3	**37.25**	**14899**	**65.3**	
S4.2	15.66	6264	67.3	Right: 1 and 2
S4.4	15.61	6244	67.8	Left: 1 and 2
S4.6	16.07	6428	63.5	Right: 2 and 3
S4.7	16.21	6484	65.0	Left: 2 and 3
S4.8	16.36	6544	62.2	Left: 4 and 5
S4.9	16.79	6716	61.0	Right: 4 and 5
S4.10	15.73	6292	61.9	Right: 3 and 4
S4.11	15.37	6148	67.0	Left: 3 and 4
Average S4	**15.95**	**6381**	**65.2**	

5.4 Regular waves

The model was exposed for different combinations of wave period, T $= 2\pi/\omega$ and wave steepness $\epsilon = H/\lambda$. For each steepness a series of waves with different periods created. Each wave had a ramp up and ramp down, where the wave was repeated 60 times in between. This was to ensure a steady state area. Between each wave there was a delay of five minutes to ensure calm water. The test conditions all the cases was exposed to are presented in Table 5.3. Here each blue peak is a unique combination of the wave period and wave steepness. For Case 2, 3, and 4, some extended combinations of wave periods and wave steepness were performed. These are presented in Table 5.4. Some of the wavelengths, λ, equalled the length of one, two,three, four, or five modules. Which could expose some interesting behaviors.

Table 5.3: Conditions for the regular waves in full scale for all cases

T [s]	λ [m]	H/λ = 1/80 H [m]	H/λ = 1/60 H [m]	H/λ = 1/40 H [m]
2	6.2452	0.0781	0.1041	0.2082
2.5	9.7582	0.1220	0.1626	0.3253
3	14.0518	0.1756	0.2342	0.4684
3.5	19.1260	0.2391	0.3188	0.6375
4	24.9810	0.3123	0.4163	0.8327
4.5	31.6165	0.3952	0.5269	1.0539
5	39.0327	0.4879	0.6505	1.3011
5.5	47.2296	0.5904	0.7872	1.5743
6	56.2072	0.7026	0.9368	1.8736
6.5	65.9653	0.8246	1.0994	2.1988
7	76.5042	0.9563	1.2751	2.5501
7.5	87.8237	1.0978	1.4637	2.9275
8	99.9238	1.2490	1.6654	3.3308

The wave files were formatted the same for all cases except for some particular cases. To create a simple system to differentiate between wave steepness, $H/\lambda = 1/80$ equaled 1. While $H/\lambda = 1/60$ and $H/\lambda = 1/40$ were respectively set as 2 and 3. These are visualized in Figure 5.14. The particular test scenarios were set as 4, but contained three wave steepness and explicit wave periods. However, this made it easier to understand in which order the wave steepness occurs during the time series.

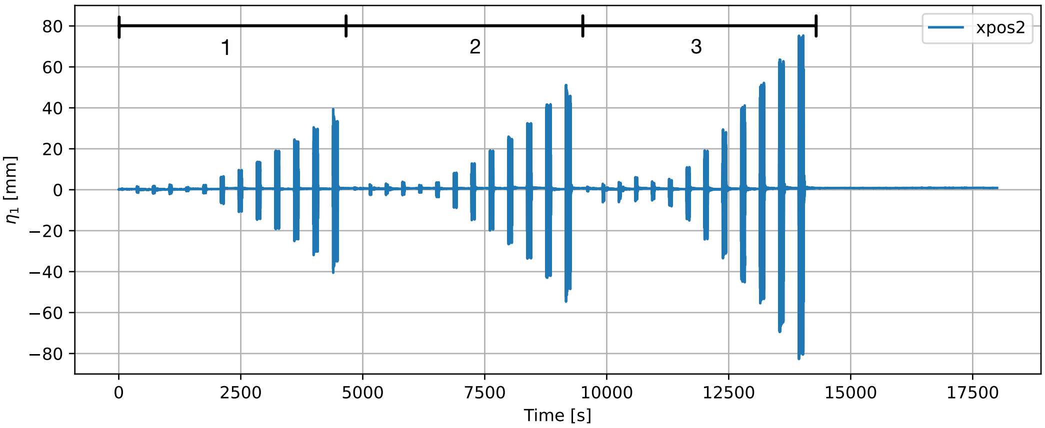

Figure 5.14: The areas with different wave steepness sectioned with the 1,2 and 3.

Table 5.4: Special test scenarios for cases 2, 3, and 4.

T [s]	λ [m]	H/λ = 1/80 H [m]	H/λ = 1/60 H [m]	H/λ = 1/40 H [m]
Case 2, 3 and 4				
2.7723	12	0.15	0.2	0.15
3.3954	18	0.225	0.3	0.225
4.0015	25	0.3125	0.4167	0.3125
Case 3 and 4				
4.4559	31	0.3875	0.5167	0.3875
4.9334	38	0.475	0.6333	0.475
Case 4				
5.3086	44	0.55	0.7333	0.55
5.7153	51	0.6375	0.8500	0.6375
6.0422	57	0.7125	0.9500	0.7125
6.4024	64	0.8	1.0667	0.8

5.5 Post-processing

The post-processing work is done in regards to reading the different time series retrieved during the experiments. During the experiment the time series was stored on different channels, i.e. motion in surge was stored in *xpos*, and the different wave probes had their own channels.

Since only regular wave tests have been performed, all the results are formatted similarly. The instruments used in the experiments create a time series, before each run, zero measurements were taken on all the tests. The length of each run differs depending on the test case. Due to the large amount of data obtained, a simple Python script was created to visualize the results. This was to reduce the time spent individually checking each period in a larger time series. The GUI is shown in Figure 5.15, where the individual period is visualized in the upper window. The whole time series obtained from the wave test is shown in the lower window. Keep in mind that this is just for one channel.

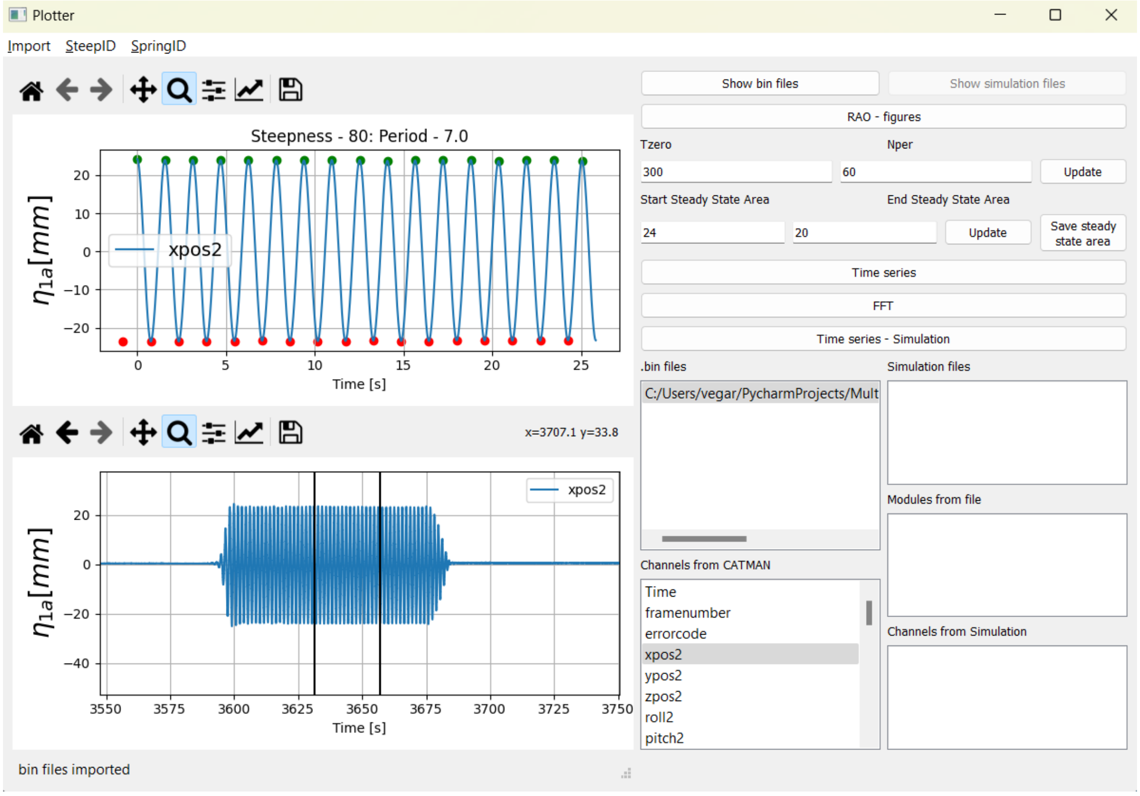

Tzero: 300

Nper: 60

Start Steady State Area: 24

End Steady State Area: 20

C:/Users/vegar/PycharmProjects/Mult

bin files imported

Figure 5.15: A snapshot of the GUI, where steady state area is in the top plot, and the whole time series is at the bottom.

5.5.1 Data Processing

Before the data retrieved from the channels were used, a series of actions were performed. When the explicit wave is retrieved, the mean of the data of the relevant channel is taken. Further, the DC offset removal could be performed to ensure the data series oscillates about zero. In the next step a band-pass filtering using a Fast Fourier Transform (FFT) is performed. The band-pass is limited from 0.2ω to 4ω, including higher-order harmonic responses. On the filtered data, the peaks and troughs are found. A predefined area that excludes the ramps decides in which area the peaks and troughs should be found. This area can be adjusted, and with the GUI, the steady state area can be adjusted for the individual waves. An example of this steady state area is shown in Figure 5.16. When the steady state area is found, the average of the peaks and troughs is used to obtain the response amplitude of the channel.

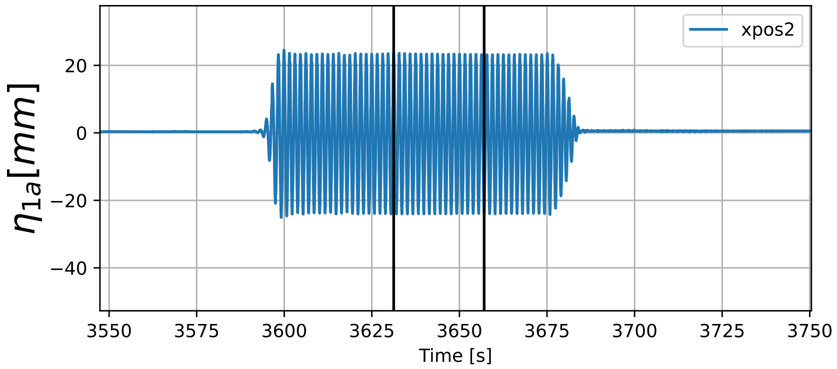

Figure 5.16: Time series for *xpos2* for Module to in Case 2 with a wave period of 7.0 seconds and a wave steepness $\epsilon = 1/80$.

5.5.2 RAO

To compare the response obtained from the different motions, a response amplitude operator (RAO) is created. RAO is known to be a transfer function that gives the ratio between a response and the incident waves. For response in surge, sway, and heave, the transfer function is given by (5.1).

$$H_j(T) = \frac{\eta_{ja}}{\zeta_a} \tag{5.1}$$

Here η_{ja} is the response in mode j, and ζ_a represents the incident wave amplitude. Since the wavemaker is approximately 15 meters from the modules, the *wp1* and *wp2* is not used to represent the incident waves. On the other hand, are *wp7* and *wp8* too close to the end of the tank and will be affected by the radiated waves. The ideal choice would have been *wp5* and *wp6*, but here it was recorded too much noise and a large difference at the same periods. Therefore, *wp3* and *wp4* represent the incident wave for the RAOs. For the last three modes, roll, pitch, and yaw, (5.2) is applied.

$$H_j(T) = \frac{\eta_{ja}}{k\zeta_a} \tag{5.2}$$

Here the expression from earlier is divided on the wave number k.

5.5.3 Check of signals

Before the lab started, it was uncertain whether it was possible to track five different modules simultaneously with the OQUS system. Previously maximum of two models had been tested at once. However, there were some worries that lag would occur in the system with five modules. Normally, the system sampled with a 50Hz sampling frequency. A simple test was performed to check that the system did not lag or that any delays occurred in Case 4. Since Module 5 was utilized with a load cell in the connection, it would instantly respond to any motion. The OQUS system and the load cell should respond with a simple push. In Figure 5.17, the response from the load cell is presented by the red line, while the blue line presents the surge motion. After five seconds, the load cell and the OQUS system respond to a push in a positive surge direction. The load cell responds faster to the change since the module does not start moving initially with the push. However, the result is acceptable.

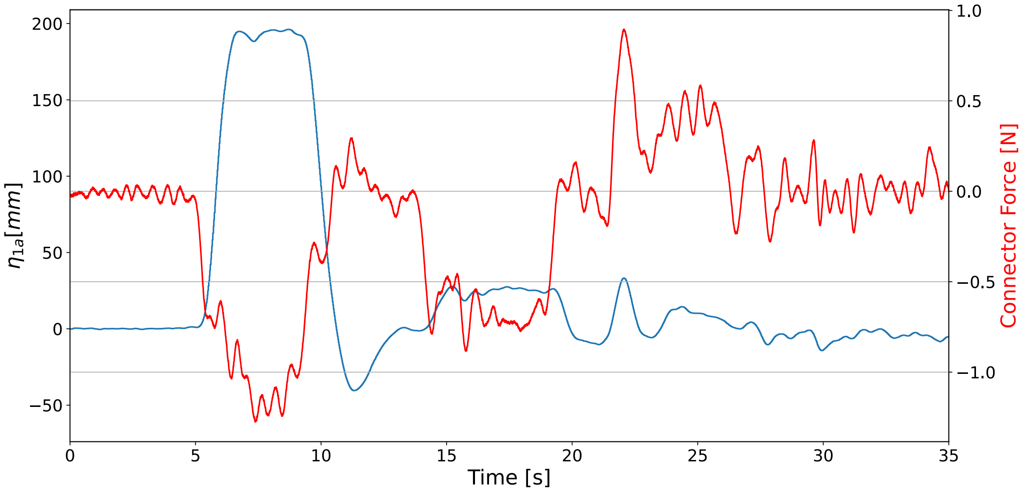

Figure 5.17: Check if there is a delay in the OQUS system by comparing surge motion with force response at Module 1.

5.6 Error Sources

During this experiment, there were some errors. For the models used in the experiment, the weight distribution, symmetry, or geometry are not guaranteed to be correct. Because of the weight, small masses could affect the mass distribution and hence affect the motion. Therefore, to balance the module, small weights have been used to adjust the weight. As the springs used has different lengths, it is also assumed they have different weights. Between the changes, the weight distribution has been controlled by checking the water line is correct.

The waves created by the wave maker have some limitations. When controlling the waves when arriving *wp5* and *wp6*, they had lower heights than expected. To compensate for this, the wanted steepness was adjusted to achieve the original wave height. Even though this was better, getting the correct wave height for every period and steepness was hard. It could also have been an error in the sensors, but it was known that the wavemaker did not always create the specified waves.

The wave tank had some limitations, which could have affected the results. One is the tank wall effect, where waves would reflect on the walls and create sideways waves. These are hard to account for, except for ensuring the waves have reached still conditions between the runs. Another problem is the sunshine that reflects the water. As the Oqus system uses reflectors to measure the module's motions, reflections from the light could create false reflectors and create a disturbance. T For the smallest waves, it was observed that they almost died out at the time they arrived to the module.

The springs were measured and adjusted between the different test scenarios. However, when the modules were aligned, it was not guaranteed that the springs would perfectly align with the module. This would create a small angle on the spring, inducing more motion in the y-direction. Another problem that was discovered was related to the mooring of the modules. In the post-processing, it was seen that forces were mostly noise and had a very small value. It was discovered that approximately 1/10 of the force acting in the mooring line disappeared through the block before the load cell. It is unclear how much impact the friction caused by the block would have on the module.

Another uncertainty was the diameter of the springs. The springs S1, S2, and S4 had more or less the same diameter. S3 had a smaller diameter. Visually in the lab, it looked like the spring would easily break through the y-axis. In contrast, it took more to do the same for the others. Therefore, the spring may bend instead of compress if there is some tilt on the spring, and then return the wrong motion.

Chapter 6

Results

This chapter will present the experimental and simulation results described in this thesis. Not all results will be included, but focusing on the main findings related to the connection stiffness will be prioritized. Except for the first case, as defined in Chapter 5.2.1, the results will not include other steepness than $\epsilon = 1/80$. This is mainly due to relatively similar behavior when looking at the different steepness.

Firstly, the results from the experiments will be presented. Here, the findings regarding responses in surge, heave, pitch and forces in the connections are mainly focused on. The results are presented as RAOs, where the surge, heave, and pitch responses are made non-dimensional and plotted against the wave period. The equivalent results for sway, roll, and yaw is added to Appendix 7.2.2. The forces are presented in Newtons and plotted against the wave period. The second part of the results will compare the simulation results with the results obtained from the experimental part.

The last results will utilize the control logic presented in Chapter 4.2 to obtain results from the simulator. Here a comparison with and without the logic will be presented for a 2x1 network.

6.1 Experimental

In the results section, the plots where the motion of any module is presented, the motion of the single module in Case 1 is also presented. This will always be visualized with a solid line so that the response can be comparable across different plots.

6.1.1 Response of Surge Motions

First Module Response

To present the RAOs of the surge motions, each module is compared with an equal module in the different test cases. The first module in each case is presented in Figure 6.1. Each of the four plots visualizes the response in the different cases for the four different stiffnesses.

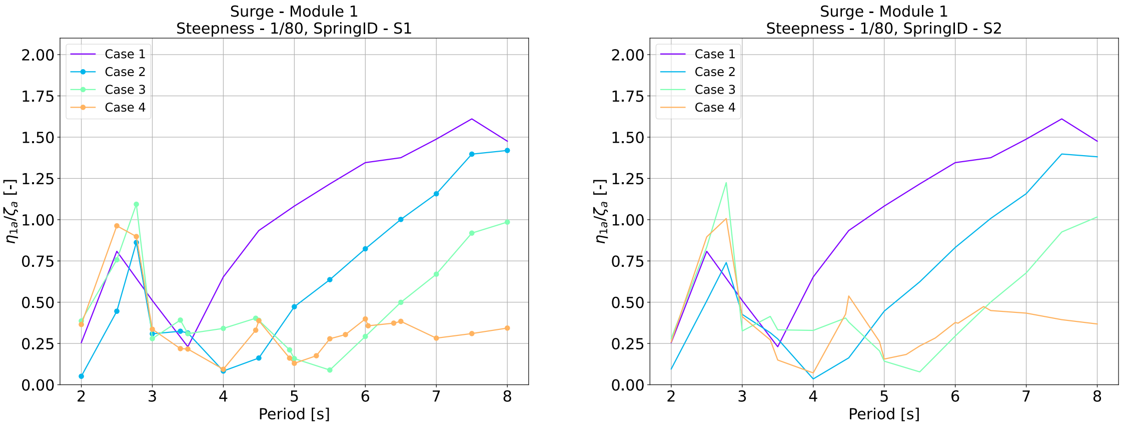

(a) RAO in surge for Module 1 with wave steepness $\epsilon = 1/80$, SpringID S1 for all cases, except Case 1.

(b) RAO in surge for Module 1 with wave steepness $\epsilon = 1/80$, SpringID S2 for all cases, except Case 1.

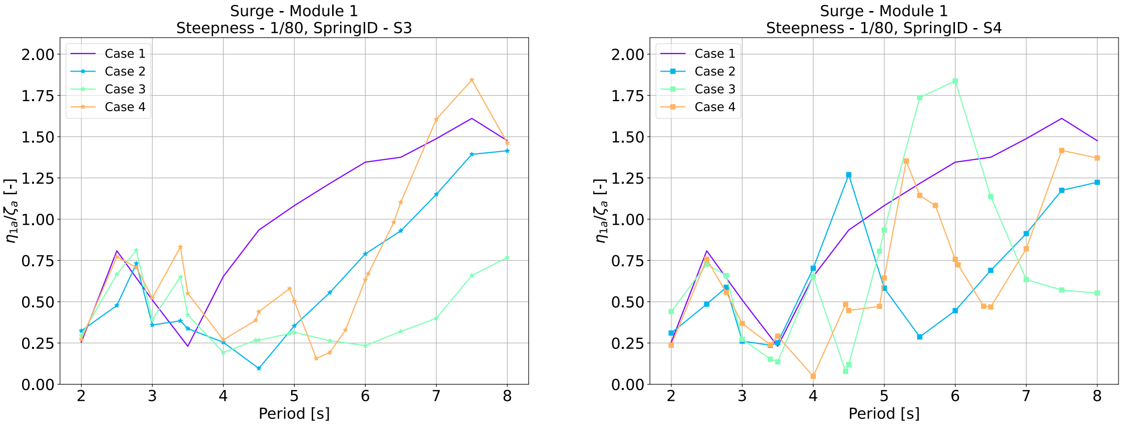

(c) RAO in surge for Module 1 with wave steepness $\epsilon = 1/80$, SpringID S3 for all cases, except Case 1.

(d) RAO in surge for Module 1 with wave steepness $\epsilon = 1/80$, SpringID S4 for all cases, except Case 1.

Figure 6.1: RAO in Surge

From Figure 6.1a and 6.1b, it is observed that the response in Case 4 decreases for increasing wave periods. It is also seen that the increasing number of modules decreases the response for higher wave periods. For the softer springs, S3 and S4, the stiffness affects the module's motion more uncertainly at higher wave periods. In Figure 6.1c, Module 1's response in Case 4 achieves a higher response than Case 1 for higher wave periods. Case 3 does, on the other hand, obtain a lower response for higher periods with S3. The softest spring decreases the amplitude at the lowest wave periods. This is especially for the cases 3 and 4 at a wave period of 2.8 seconds.

Middle Module Response

In cases 3 and 4, there are one and three modules between the moored modules. Along with the single module from Case 1, these are presented in Figure 6.2. Since Case 2 has no module between, it is not presented.

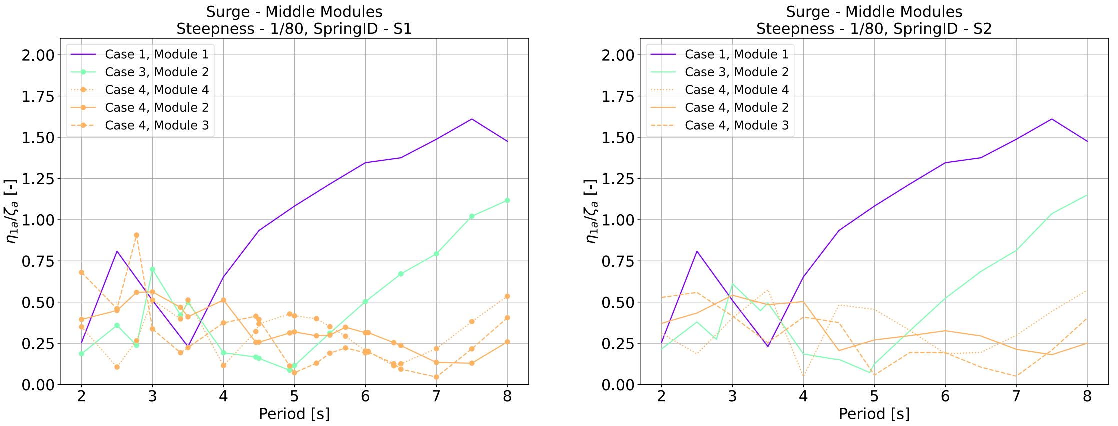

(a) RAO in surge for the middle modules with wave steepness $\epsilon = 1/80$, SpringID S1 for all cases, except Case 1

(b) RAO in surge for the middle modules with wave steepness $\epsilon = 1/80$, SpringID S2 for all cases, except Case 1

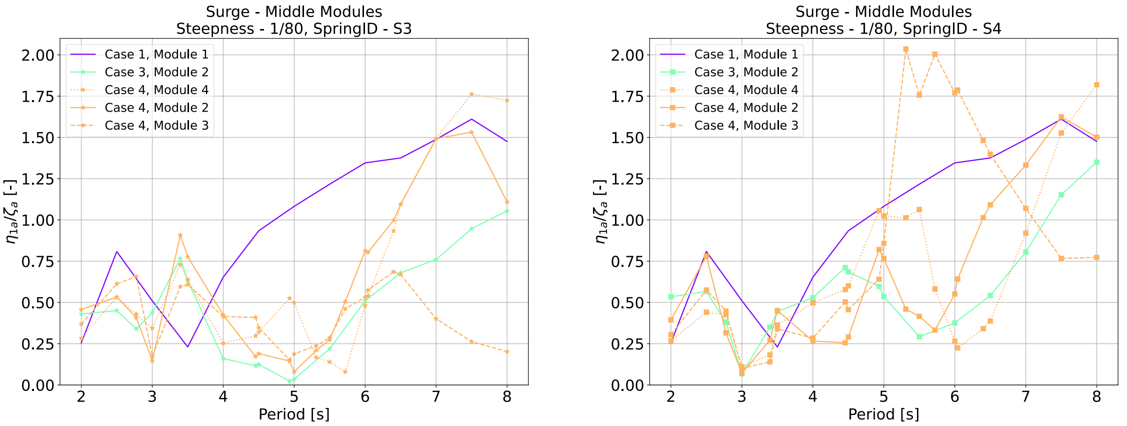

(c) RAO in surge for the middle modules with wave steepness $\epsilon = 1/80$, SpringID S3 for all cases, except Case 1

(d) RAO in surge for the middle modules with wave steepness $\epsilon = 1/80$, SpringID S4 for all cases, except Case 1

Figure 6.2: RAO in surge for the middle modules

As for the first module, the middle modules in Case 4 reduced their movements for longer wave periods when springs S1 and S2 are utilized. Despite some differences, the three modules mostly behave similarly regarding wave period. The selection of stiffness does not significantly influence the response at lower periods as it did for the first modules. This is evident in cases 3 and 4, where augmented stiffness at certain wave periods leads to decreased motion.

With the S3 spring, a cancellation for Case 4 can be observed at a wave period of 3 seconds. Similarly, when the S4 spring is used, cancellations are also observed in Case 3. When the S4 spring is used, this cancellation also appears for Case 3. As for Module 3 in Case 4, there is a larger peak between the wave periods of 5 and 6 seconds. However, modules 2 and 4 have a lower response at the same periods before the response increases again.

Last Module Response

The last module in each test case is presented in Figure 6.3. The response is observed to be very similar to the first module's response, which might be largely affected by the mooring. There are, however, observed that the response is larger for Case 3 and Case 4. Case 2 for S1, S2, and S3, have a similar response as the first module. A difference for the cases with multiple modules is the behavior with spring S4. While Case 3 achieves a peak at a wave period of 6 seconds, and it decreases again for the following wave periods. This is similar to whats been noticed in the first module. A peak is obtained for cases 2 and 4, but the response does not decrease as severely. In Case 4, the response does in fact, keep increasing with increasing wave periods. However, the slope is less than between wave periods 4.5 and 5.4.

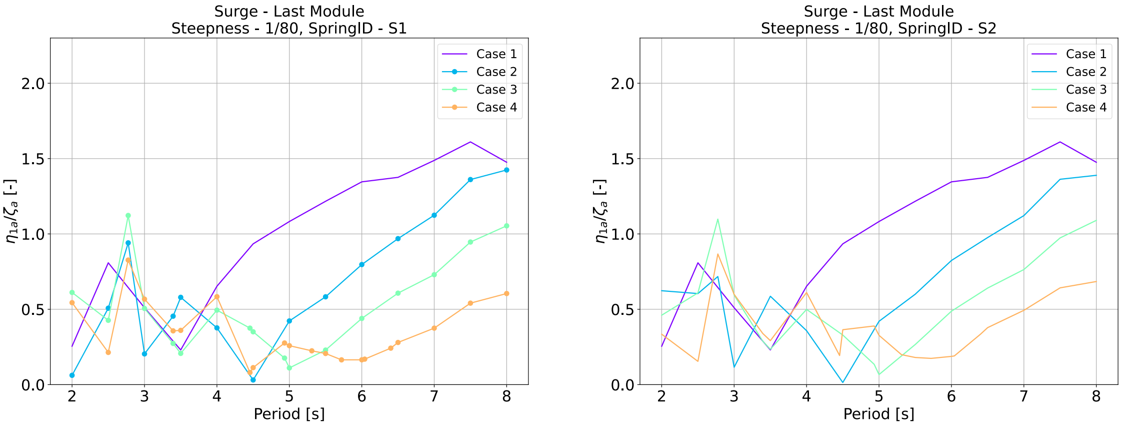

(a) RAO in surge for the last module with wave steepness $\epsilon = 1/80$, SpringID S1 for all cases, except Case 1

(b) RAO in surge for the last module with wave steepness $\epsilon = 1/80$, SpringID S1 for all cases, except Case 1

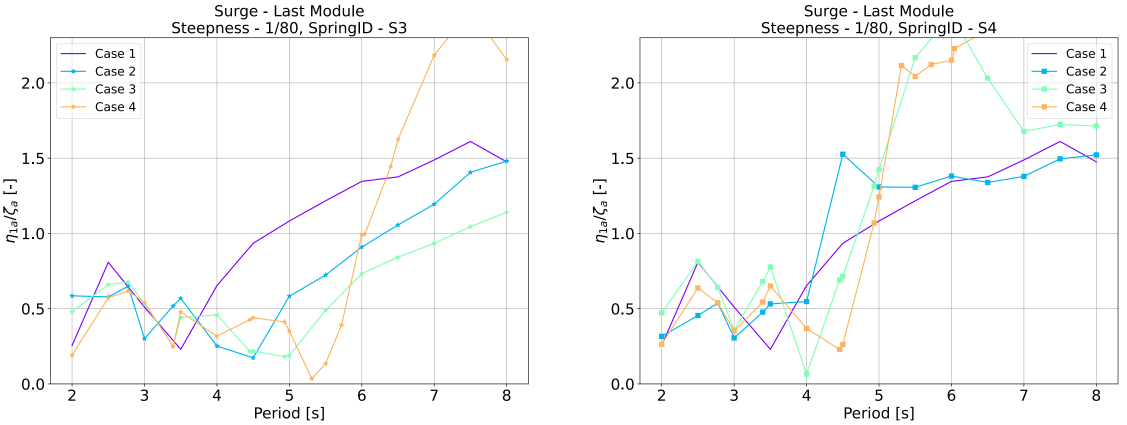

(c) RAO in surge for the last module with wave steepness $\epsilon = 1/80$, SpringID S1 for all cases, except Case 1

(d) RAO in surge for the last module with wave steepness $\epsilon = 1/80$, SpringID S1 for all cases, except Case 1

Figure 6.3: RAO in surge for the last module

For Case 4, during the experiment, it was observed that the modules collided with the softest spring. Indicating that this spring is too soft. An example is visualized with images in Figure 6.4. Here are three consecutive frames from a video capturing the collisions. Because of a wave steepness $\epsilon = 1/80$, the modules do not overlap each other, instead, the spring folds and induces sway motions. With steeper waves, it was observed that the modules to the right in Figure 6.4 overlapped each other.

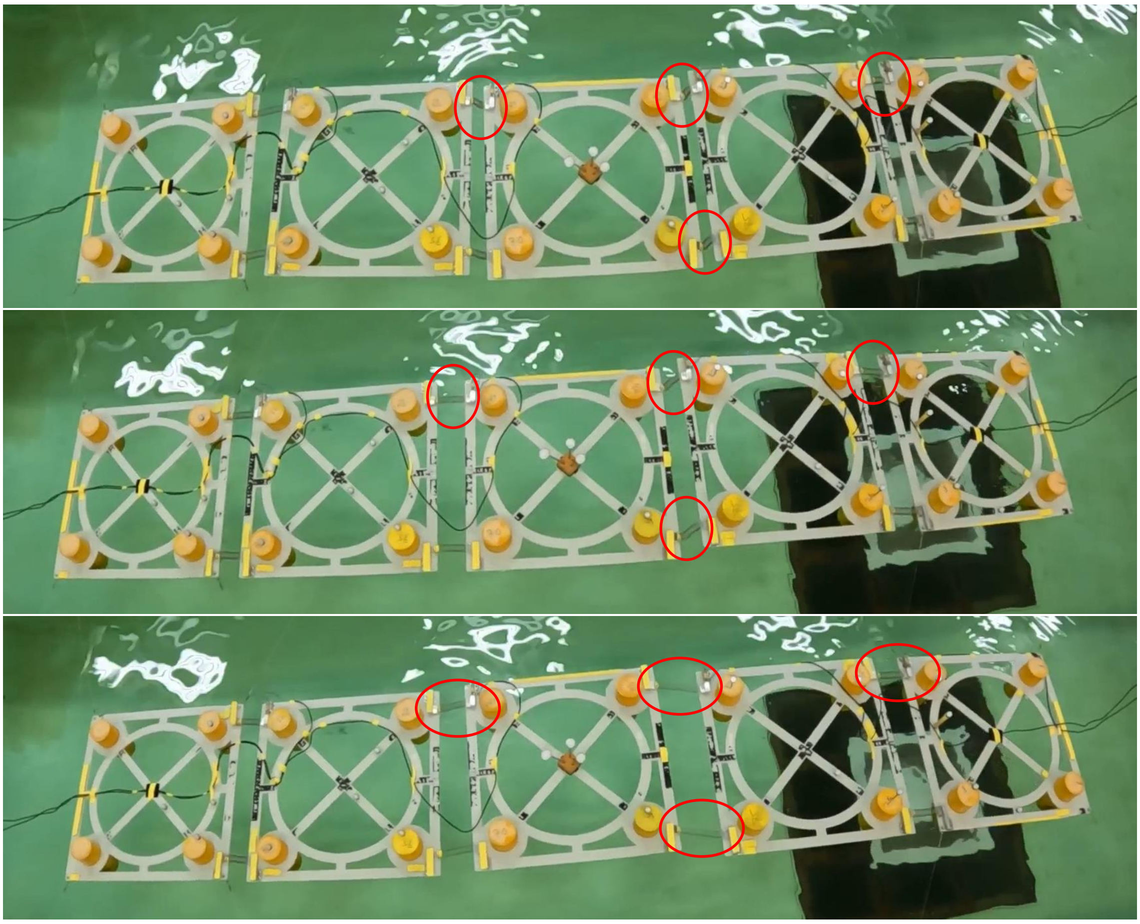

Figure 6.4: Modules in Case 4 seen from bird perspective when S4 was used in between, with $\epsilon = 1/80$ and wave period of 8 seconds.

6.2 Heave and Pitch Response

The results for heave pitch had only small difference for different stiffness. Therefore, only the results where S1 and S4 are used are presented and discussed. The remaining results are added in Chapter 7.2.2.

6.2.1 First Module Response

The heave and pitch response for the first module is presented in Figure 4. For the heave response, there is a clear indication that one module has a larger response than multiple connected modules. The response for Case 2, with two modules, behaves very similarly to a single module before the cancellation at a wave period of 3.5 seconds. Interestingly, the observed peak at a wave period of 2.5 seconds shows that Case 3 responds less than Case 4. However, after the cancellation, the modules behave similarly for increasing wave periods, independent of the spring. With S4, there is an advantage of less amplitude at the resonance in all cases.

Comparing the pitch response in Figure 6.5b and 6.5d, it becomes apparent that the stiffness has a minor impact on the response. This is not surprising since no vertical springs are present in the connector. At higher pitch angles, the horizontal spring might have a small vertical component, which is likely negligible.

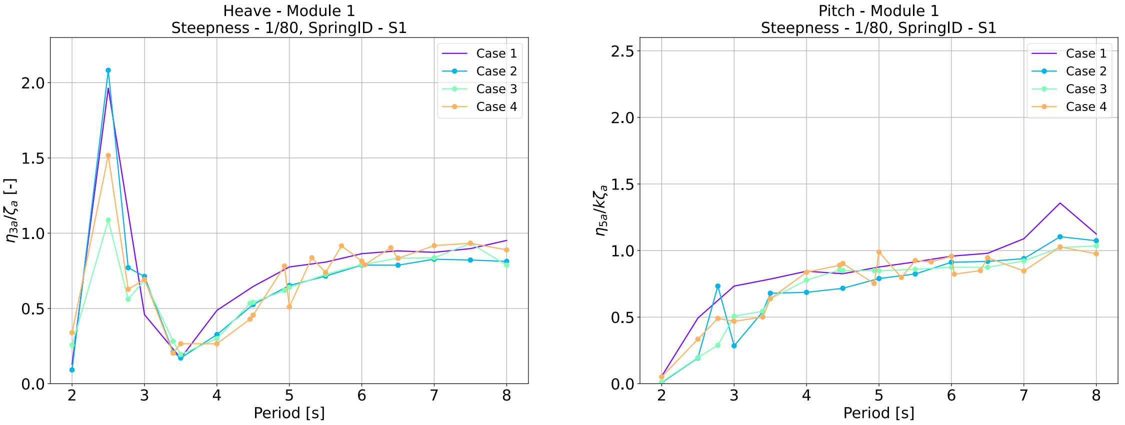

(a) RAO in heave for the first module with wave steepness $\epsilon = 1/80$, SpringID S1 for all cases, except Case 1

(b) RAO in pitch for the first module with wave steepness $\epsilon = 1/80$, SpringID S1 for all cases, except Case 1

Figure 6.5: RAO in Heave

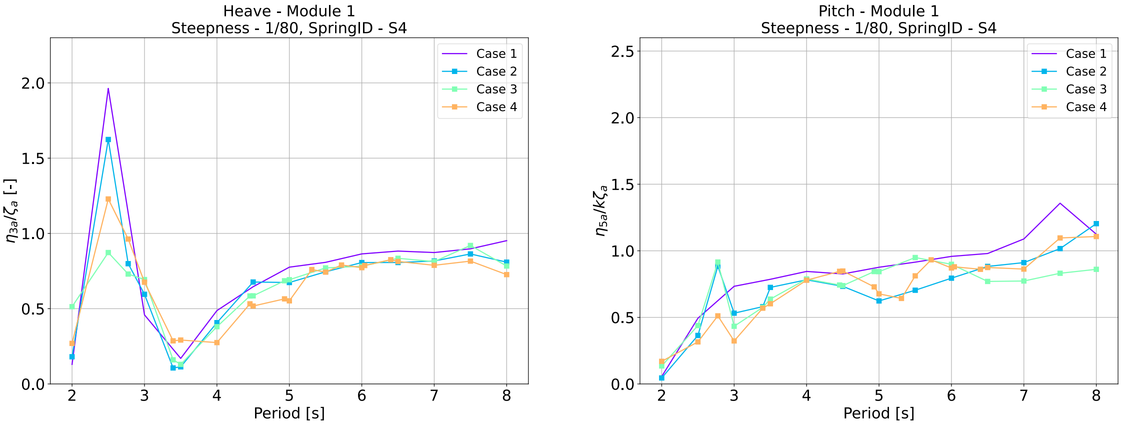

(c) RAO in heave for the first module with wave steepness $\epsilon = 1/80$, SpringID S4 for all cases, except Case 1

(d) RAO in pitch for the first module with wave steepness $\epsilon = 1/80$, SpringID S4 for all cases, except Case 1

Figure 6.5: RAO in pitch and heave

Middle Module Response

The response in heave and pitch at the middle modules are presented in Figure 5. Compared to the first module, the resonance response is lower in the heave for the central modules. Depending on the specific module, cases 3 and 4 have similar responses. Furthermore, the cancellation period is different for S1 and S4, as it seems it has been increased with half a period for S1. This seems also to affect the motion of the module for higher periods, as the response with S4 is higher. Upon examining the pitch movements, it appears that they are quite alike. However, compared to the first module, the motions are larger.

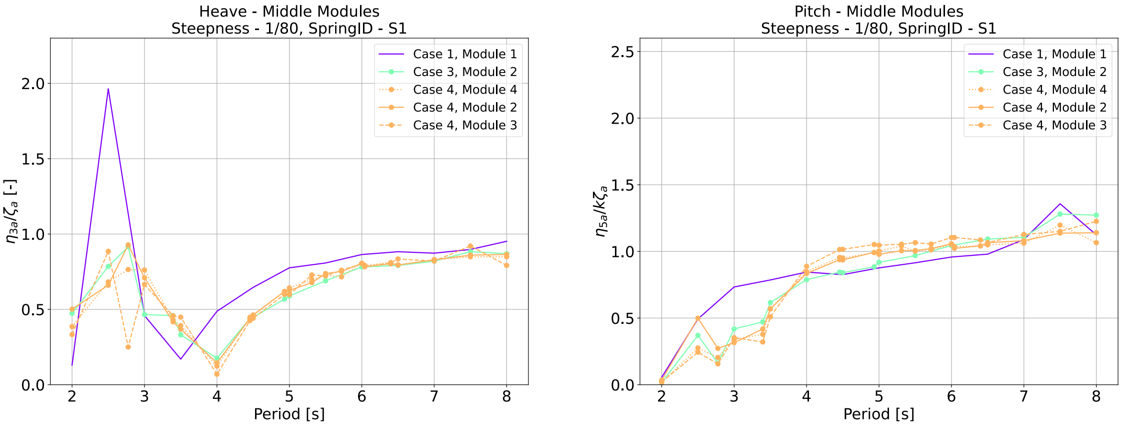

(a) RAO in heave for the middle modules with wave steepness $\epsilon = 1/80$, SpringID S1 for all cases, except Case 1

(b) RAO in pitch for the middle modules with wave steepness $\epsilon = 1/80$, SpringID S1 for all cases, except Case 1

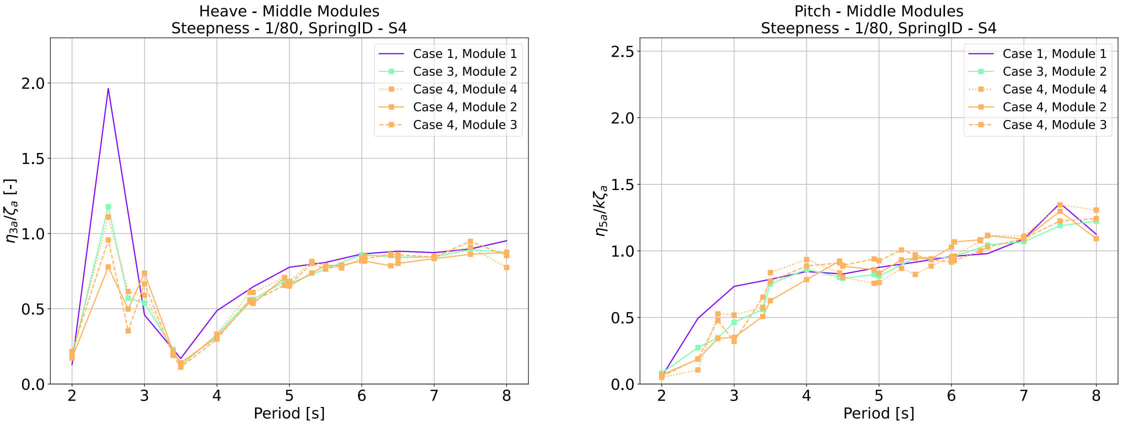

(c) RAO in heave for the middle modules with wave steepness $\epsilon = 1/80$, SpringID S4 for all cases, except Case 1

(d) RAO in pitch for the middle modules with wave steepness $\epsilon = 1/80$, SpringID S4 for all cases, except Case 1

Figure 6.6: RAO in Heave

Last Module Response

The results for the last module is presented in Figure 6. The response is similar to the first module, with the peak and cancellation at the same wave periods. The last module has a larger response at resonance with S1 for Case 4. It can also be observed that the cancellation is greater at the last module with S4.

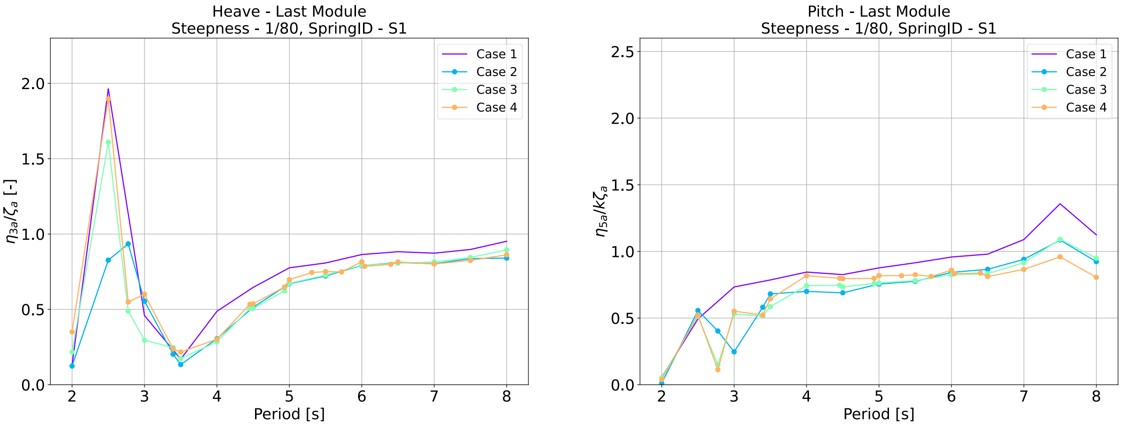

(a) RAO in heave for the last module with wave steepness $\epsilon = 1/80$, SpringID S1 for all cases, except Case 1.

(b) RAO in pitch for the last module with wave steepness $\epsilon = 1/80$, SpringID S1 for all cases, except Case 1.

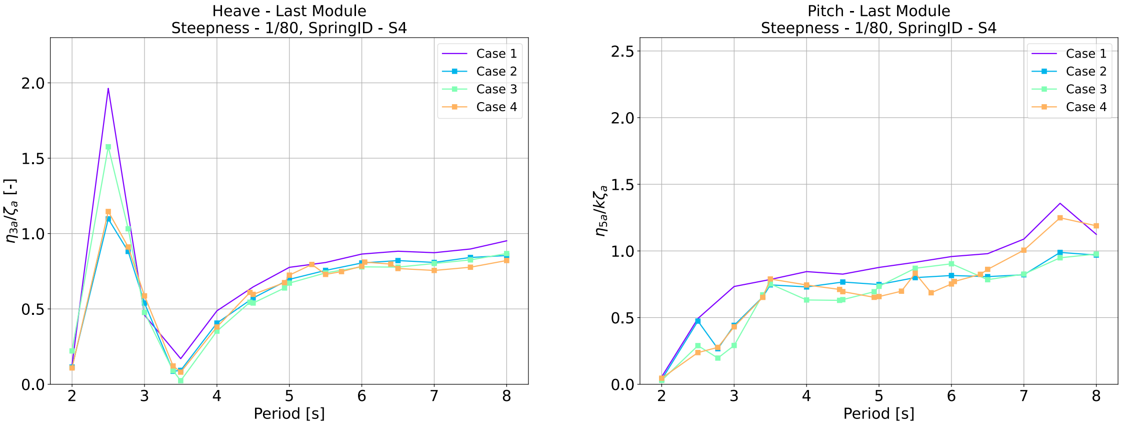

(c) RAO in heave for the middle modules with wave steepness $\epsilon = 1/80$, SpringID S4 for all cases, except Case 1.

(d) RAO in pitch for the last module with wave steepness $\epsilon = 1/80$, SpringID S4 for all cases, except Case 1.

Figure 6.7: RAO in Heave

6.2.2 Connector Force

The connector forces are presented as an RAO in Figure 6.8. All the connectors for the different cases are presented for each of the different springs used.

In the area between the wave periods of 2 and 4 seconds, there are several peaks for S1, S2, and S3. When S4 is used, the forces are smaller, and now larger peaks appear. Giving reason for low stiffness reduced the connection force at lower wave periods. However, from a wave period of 4 seconds and further, the largest force appears with spring S4. When the springs S1, S2, and, S3 are used, there is a stable increasing force with increasing wave periods. Where the force obtains its maximum at a wave period of 7.5 seconds. The chaotic RAO when S4 is used, is probably related to the collision behavior.

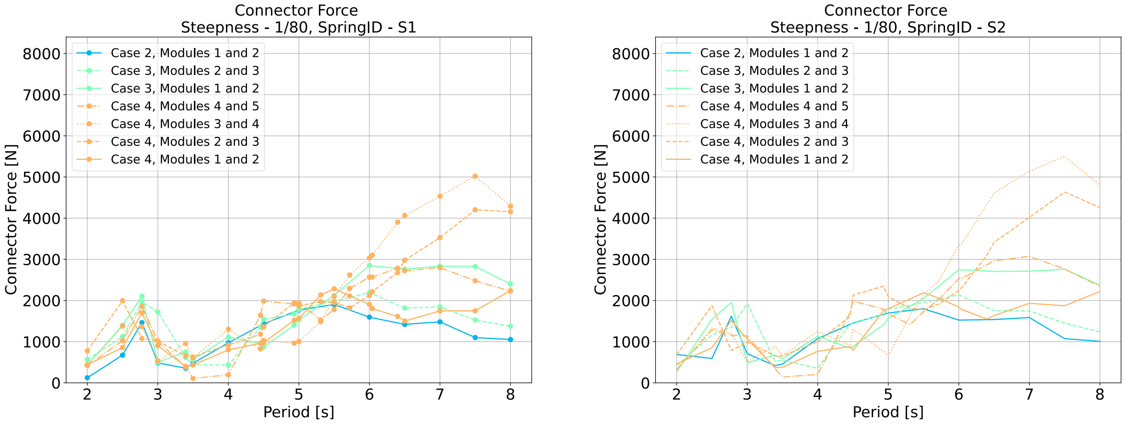

(a) RAO of the connector forces from the different test cases with $\epsilon = 1/80$ and SpringID = S1

(b) RAO of the connector forces from the different test cases with $\epsilon = 1/80$ and SpringID = S2

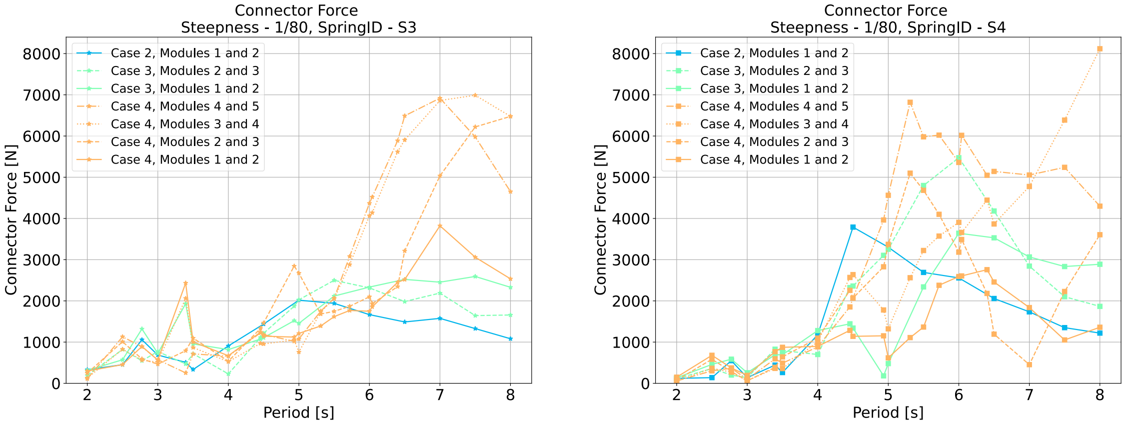

(c) RAO of the connector forces from the different test cases with $\epsilon = 1/80$ and SpringID = S3

(d) RAO of the connector forces from the different test cases with $\epsilon = 1/80$ and SpringID = S4

Figure 6.8: RAO of the force in the connectors

6.2.3 Summary of the Experimental Results

After reviewing the results for the modules in different cases, there are some takeaways. When S1 and S2 are used, the high stiffness makes the modules move together in higher periods. However, the force between the modules increases with the higher wave periods. With softer connectors, the response increases severely for higher wave periods. Module 3 in Case 4 is an exception, with a decreasing response after obtaining a peak between 5.4 and 6.5 wave periods, as seen in Figure 6.2d. The results show that different connector stiffness could effectively influence the motion of the modules.

A combination of different stiffnesses between the modules should be studied to improve the total response to a whole floating island. Because, as observed, two neighbor modules can have large separations in their responses in some scenarios.

6.3 Validation of Case 1

In the first case, only one moored module was placed in the tank. The simulated results are compared with the experimental results to validate the simulator for basic hydrodynamics. In Figure 6.9, an RAO of the surge motions compares the simulator and the experiment. In these results, no modifications are made in the numerical model based on observed behaviors from the experiment. The results for different wave steepness are presented. Notable observations are that the simulator underestimates the peak response at the wave period of 2.5 seconds. In the experiment, the module has a cancellation at a wave period of 3.5 seconds. The simulation does cover the cancellations, but not at the same wave period.

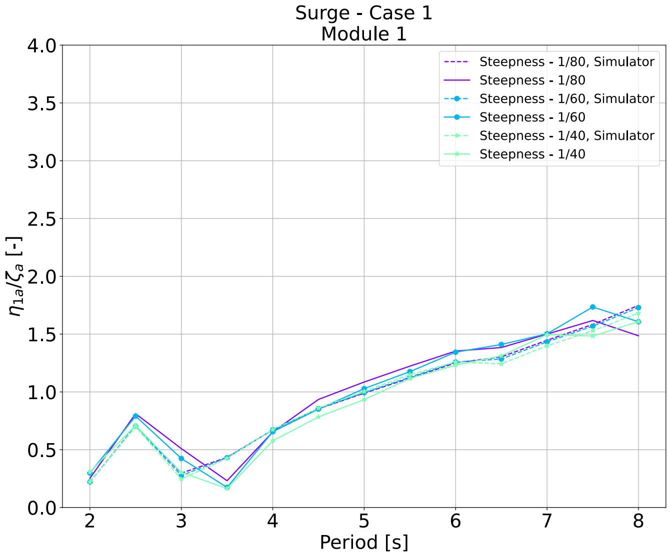

Figure 6.9: Comparison between the surge RAO for simulation and experimental for Case 1.

The heave and pitch RAO are presented in Figure 6.10a and 6.10b. The heave response is well covered in the simulations but slightly overestimated when the wave periods increase. On the other hand, the pitch response estimates a peak at a wave period of 3 seconds. This could be due to the lack of damping in the system, which is a consequence of the potential flow theory. At the highest periods in the comparison, the simulated and experimental responses coincide.

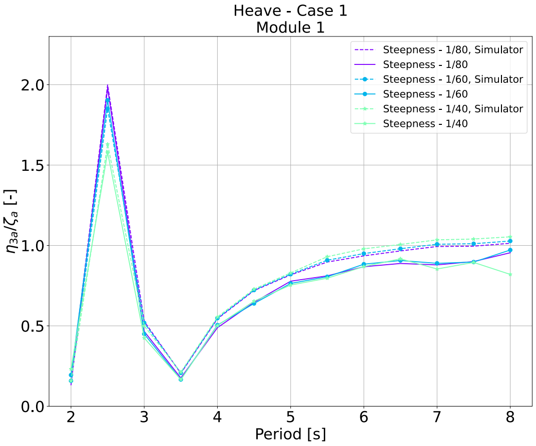

(a) Comparison between the heave RAO for simulation and experimental for Case 1.

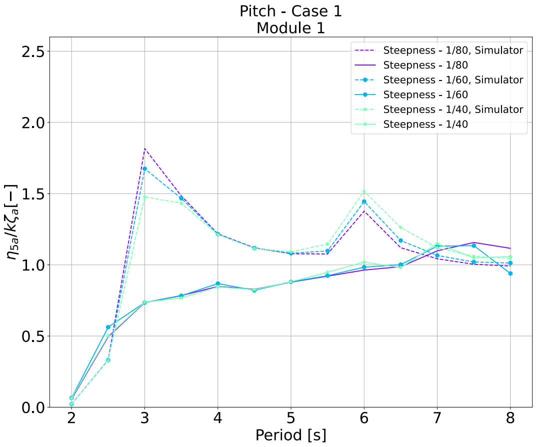

(b) Comparison between the pitch RAO for simulation and experimental for Case 1.

6.4 Validation of Case 2

In Figure 6.12, the responses in surge from the simulations and the experiments are compared for Case 2. Compared to the response for Case 1, multiple peaks can be observed for the different springs. Both simulation and experimental results follow the same trends. The peak responses are overestimated in the simulated results compared to the experimental results. Based on the response of Module 1 and Module 2, it looks like the overestimation is larger for the softer springs, S3 and S4.

The heave responses in Figure 6.12a and 6.12b, show that the results from the experiment and simulation coincide well. The wave period for the peaks differs between the results. In the numerical model, the connector has equal stiffness in the x-, y-, and z-directions. Because of this implementation, the simulated results will have a connector force vertically as well. Which is expected to affect the heave and pitch response. This can explain why Module 2 gets a larger response with the simulated results than the experimental. At the same time, Module 1 underestimates the response at the peak. The pitch response, presented in Figure 6.13, shows an overestimated response for the simulated results. However, for both heave and pitch, the experimental and simulated results follow the same trends. By tuning the simulator, more accurate results can be generated.

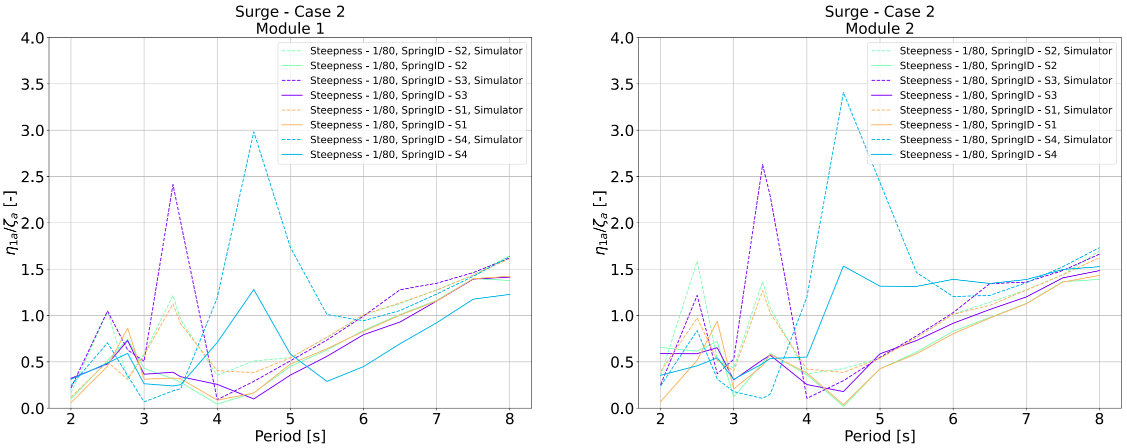

(a) RAO in surge for Module 1

(b) RAO in surge for Module 2

Figure 6.11: RAO in surge for Module 1 and Module 2 in Case 2

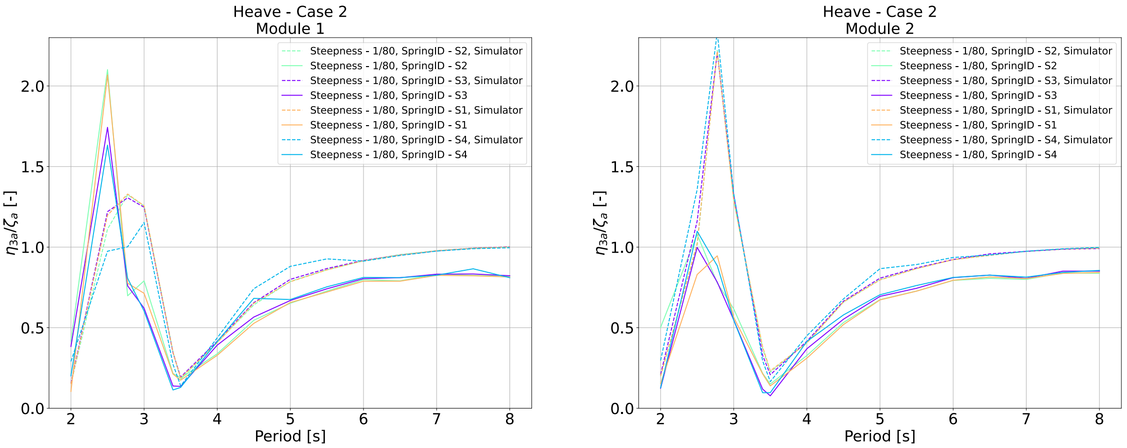

(a) RAO in heave for Module 1

(b) RAO in heave for Module 2

Figure 6.12: RAO in heave for Module 1 and Module 2 in Case 2

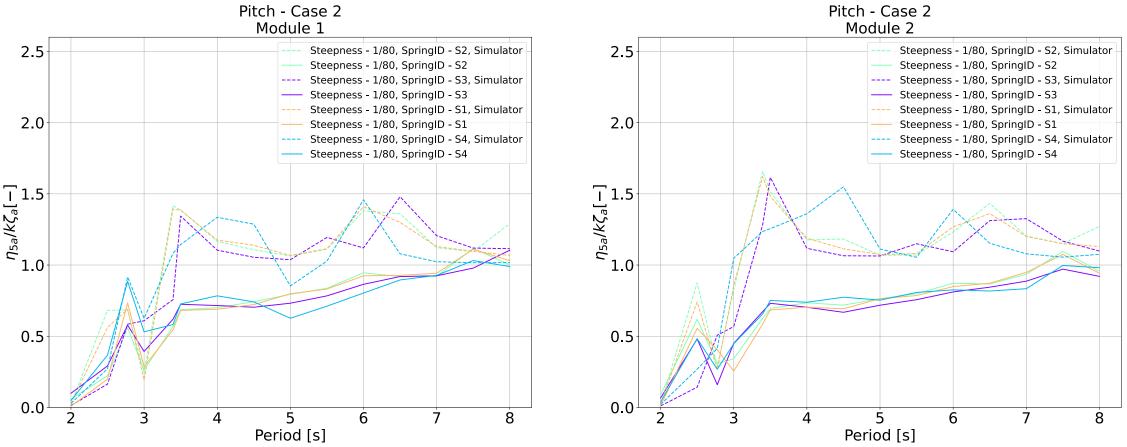

(a) RAO in pitch for Module 1

(b) RAO in pitch for Module 2

Figure 6.13: RAO in pitch for Module 1 and Module 2 in Case 2

The forces that occur in the connector between Module 1 and Module 2 in case 2 are presented in Figure 6.14. Here the forces from the simulator are presented as dotted lines, while the experimental results are sold lines. However, with the F31 connector, the results follow the same trend. For the largest peak at the wave period of 4.5 seconds, the simulator overestimates the force by more than double.

When F10 and F11 are used, the results in the simulator follow each other closely, and also the lab results. However, there are some deviations between the simulator and the experiment for these two connectors. While the experimental results have a peak at a wave period of 2.8 seconds. The numerical results obtain a peak at wave periods of 2.5 and 3.4 seconds.

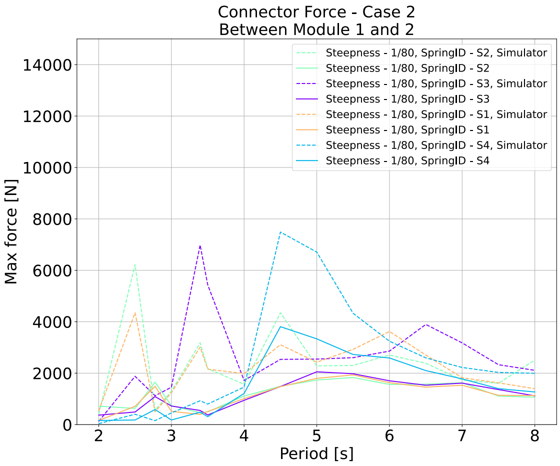

Figure 6.14: Connector force between Module 1 and 2 in Case 2.

6.5 Validation of Case 3

The pitch results were not included for this case, as there was no significant difference compared to Case 2. The results are added to the appendix.

The surge RAO comparing the simulations and the experiments are presented in Figure 6.15. They appear to have the same trends, but the simulator overestimates the response. For the cases where S3 has been used in the simulator, there are places where it contradicts the response from the experiment. The peak at a wave period of 4.5 seconds could be the response in the experimental data at a wave period of 5 seconds. For the higher springs, S1 and S2, the results are very good for wave periods above 5 seconds for all Modules.

The heave response is presented in Figure 6.16c. Where the methods generally have the same results. There is still a mismatch in the wave period for the peaks that occur for the lower wave periods. For Module 2, there is also a difference in what wave period the cancellation occurs. The connector forces are presented in Figure 6.17. With the springs S1 and S2, the experiment and simulations fits well in the beginning. A deviation occurs after a wave period of 3 seconds, which seems to be more or less constant for the rest of the wave periods. It appears that this deviation is also present with S3 and S4, suggesting that fine-tuning the simulator could improve the resulting forces.

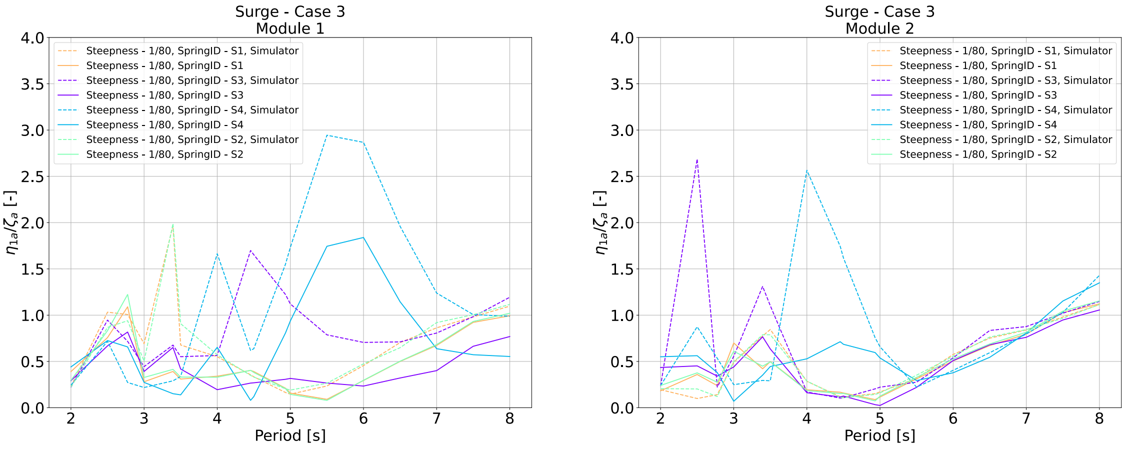

(a) RAO in surge for Module 1 (b) RAO in surge for Module 2

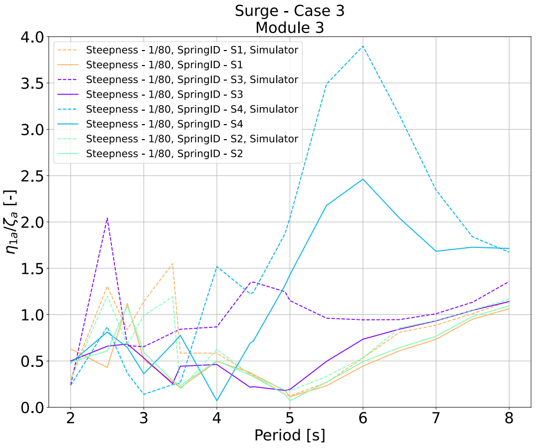

(c) RAO in surge for Module 3

Figure 6.15: RAO in surge in Case 3

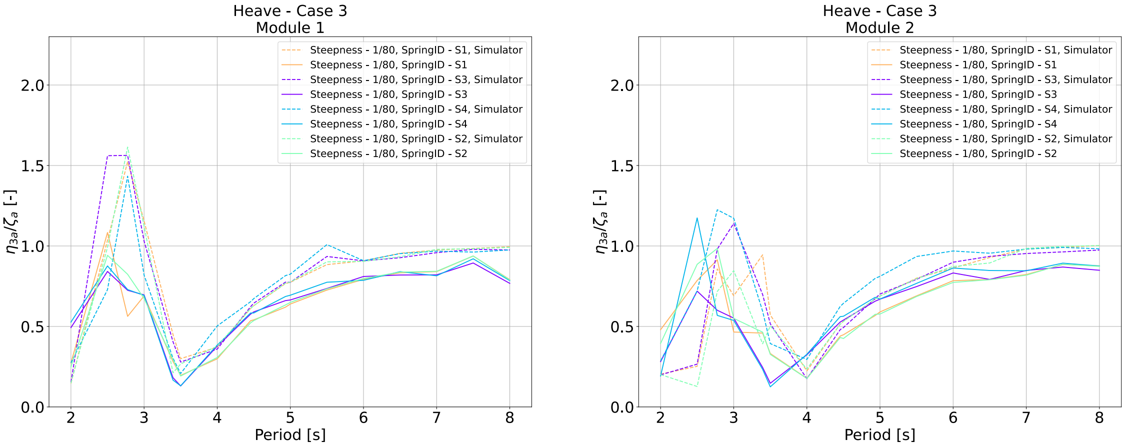

(a) RAO in heave for Module 3 (b) RAO in heave for Module 2

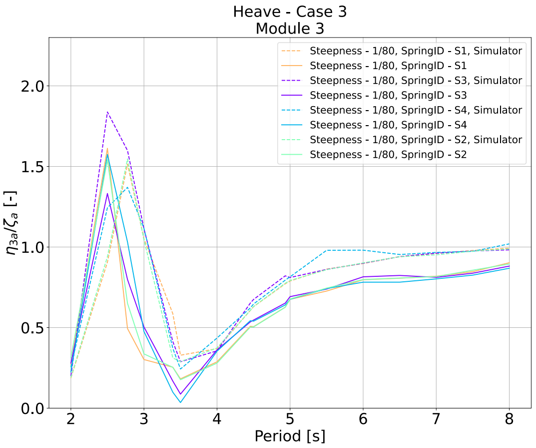

(c) RAO in heave for Module 3

Figure 6.16: RAO in heave in Case 3

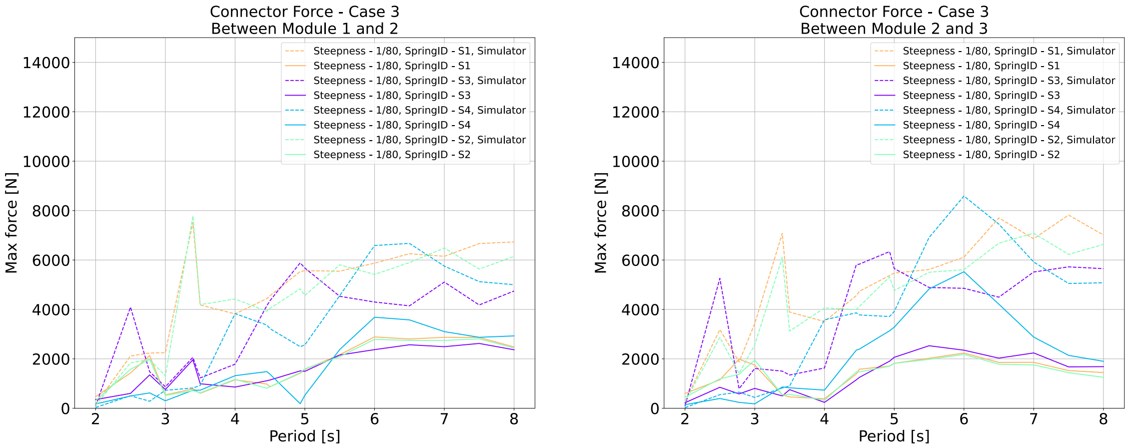

(a) Force between Module 1 and Module 2

(b) Force between Module 2 and Module 3

Figure 6.17: Connection forces in Case 3

6.6 Validation of Case 4

The motion results for surge from the simulation and experiment for Case 4 are presented in Figure 6.18. In this case, the simulations are also capable of keeping the same trend as the experimental results. This shows that the simulator can replicate the behavior for multiple connected modules. However, there are some peaks where the simulator overestimates, which has been seen previously. For the results in heave, all the RAOs except for Module 3 are similar to the already seen response. However, for Module 3 in Figure 6.19c, two relatively large peaks are observed at 2.5 and 3 seconds. Except for spring S4, the simulator is capable of detecting this response. As for Case 3, the pitch RAO is added to the appendix.

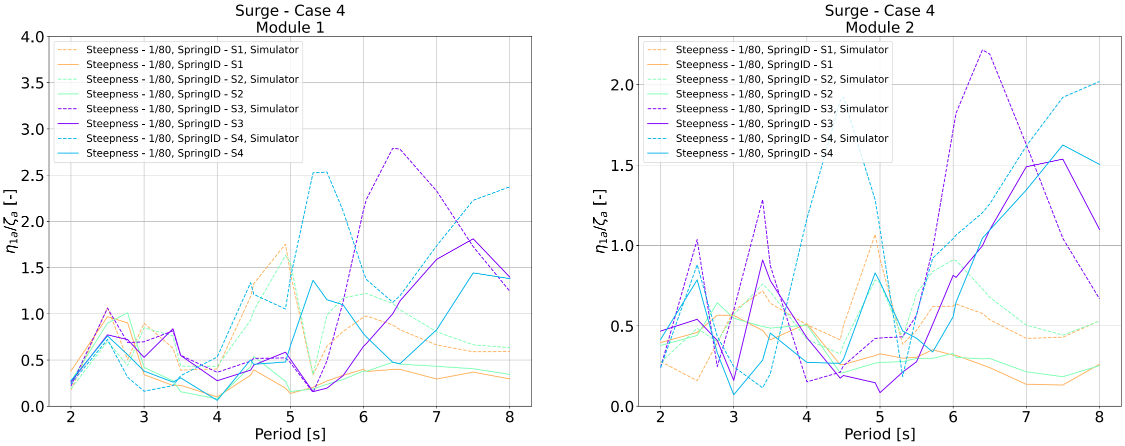

(a) RAO in surge for Module 1

(b) RAO in surge for Module 2

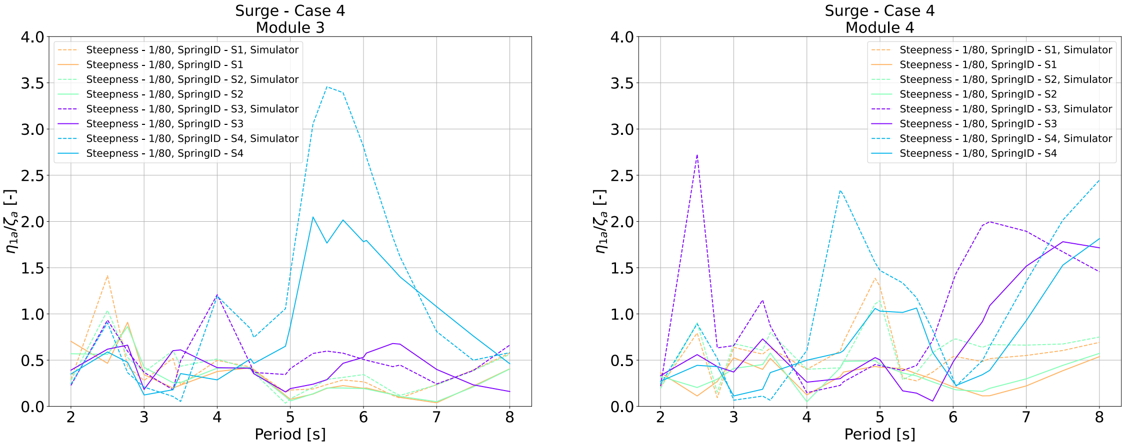

(c) RAO in surge for Module 3

(d) RAO in surge for Module 5

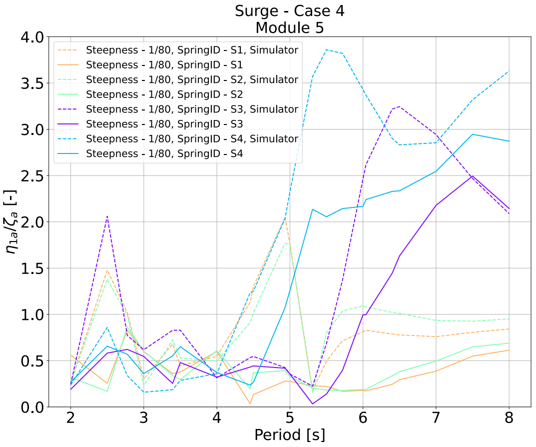

(e) RAO in surge for Module 5

Figure 6.18: RAO in surge for the individual modules in Case 4.

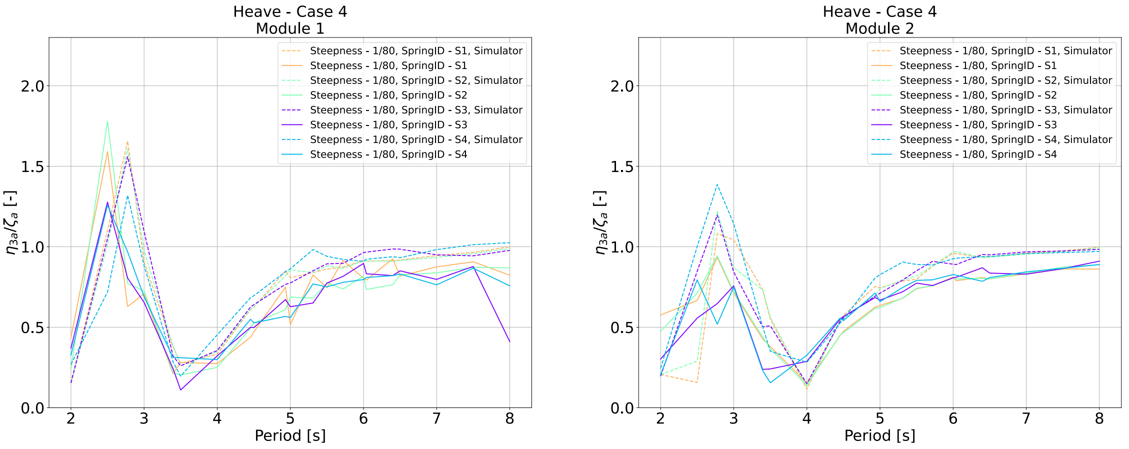

(a) RAO in heave for Module 1

(b) RAO in heave for Module 2

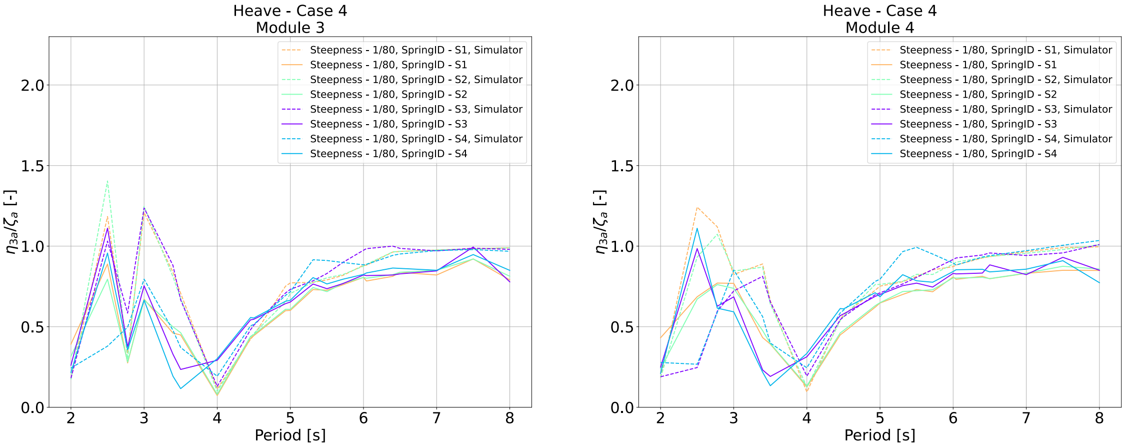

(c) RAO in heave for Module 3

(d) RAO in heave for Module 5

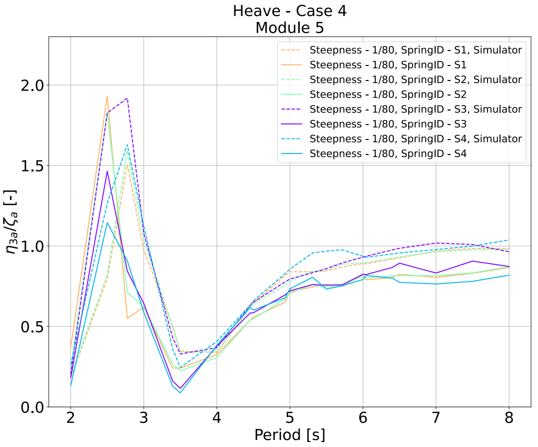

(e) RAO in heave for Module 5

In Figure 6.20, the force in the connectors is presented for Case 4. In general, the trend of the RAO is similar for the simulator and the experimental data. As seen for the surge motion, the simulator overestimates the peak response. This is especially the case when the stiffer connectors are used. However, as observed in Case 3, there seems to be a constant deviation between the simulation and the experiment.

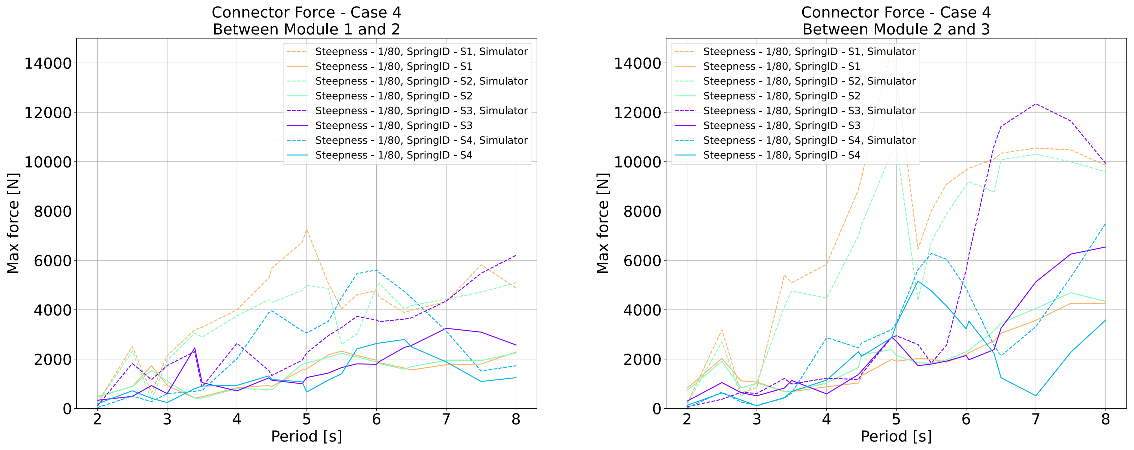

(a) Force between Module 1 and Module 2

(b) Force between Module 2 and Module 3

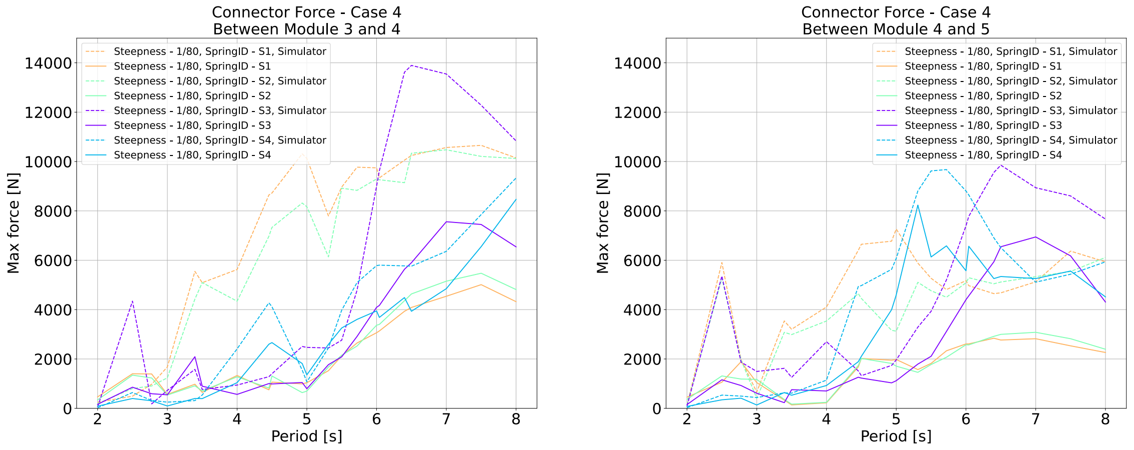

(c) Force between Module 3 and Module 4

(d) Force between Module 4 and Module 5

Figure 6.20: Comparison between the connector forces from simulation and experiment in Case 4.

6.7 Force Comparison and Eigenperiods

Based on the presented results of the connector forces, it has been observed that there are significant differences between the simulations and the experimental findings in certain cases. The excitation and drag forces are the only external forces acting on the module in the simulator. In the experiment, it is more complex. In Figure 6.21, an FFT analysis of the connectors in Case 4 for the experimental data is performed.

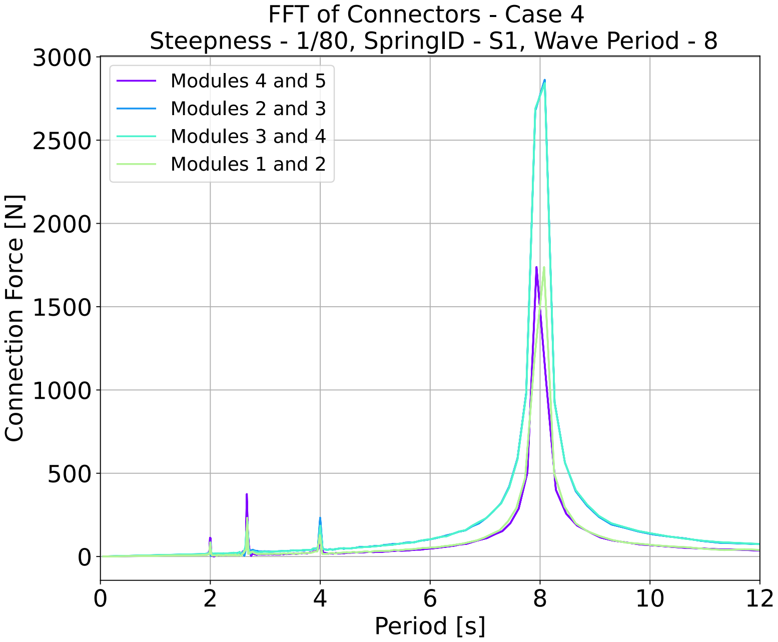

Figure 6.21: FFT analysis of the connectors in Case 4 of the experimental data.

The analysis shows that the largest force occurs with a period that coincides with the wave period. There are minor contributions at the periods, 4, 2.7, and 2 seconds. These correspond to the force's 2ω, 3ω, and 4ω components in the frequency domain. Where $\omega = 2\pi/(T = 8s)$ in this case. In Reiten (2022), multiple experiments were conducted where a rectangular pontoon was placed in the wake of another. He discovered that the 2ω component dominates the difference in force between two modules after each other. The study compares the force with the KC number, and the second harmonic force increases with increasing the KC number. He also comments that for a larger system, with multiple pontoons in a chaotic condition, consisting wake shedding from several cylinders will occur. It would then be believed that this effect will affect the last connectors the most. However, from Figure 6.21, the connection force between Modules 2 and 3 is the largest for the 2ω component. How much the wake from the pontoon will affect the next module depends on the distance between them. It is hard to conclude around these forces, as many other variables could affect the results.

Based on the observations from the FFT analysis of the experimental data, an FFT was taken of the connector force between modules 3 and 4 and modules 4 and 5 from the numerical data. These results are presented in Figure 6.22.

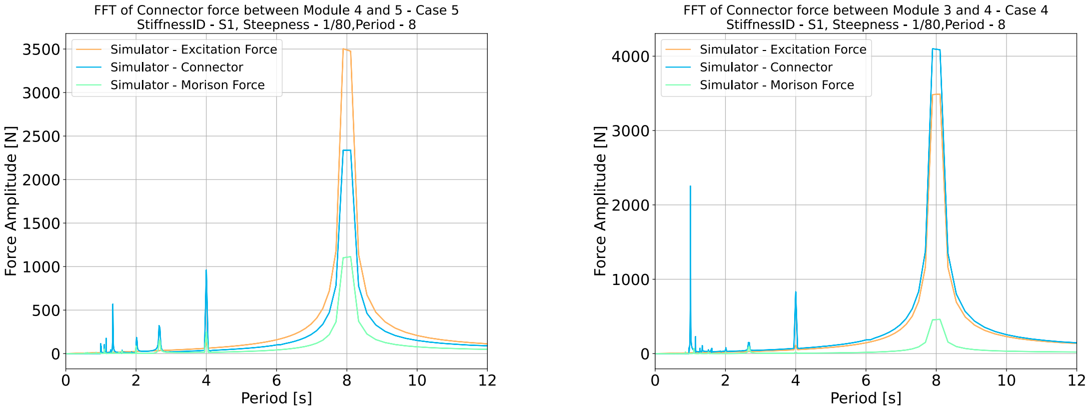

Figure 6.22: An FFT spectrum of the connector between Module 4 and 5, and between Module 3 and 4. For both cases, the wave period is 8 seconds, with $\epsilon = 1/80$ and spring S1

The FFT of the numerical results shows that there exist higher frequencies. The excitation force is expected only to have the first harmonic period. But it can be seen force has a very small contribution from higher frequency components. Further, the connector force and Morison force can be seen to have frequency components higher than 4ω. For the connector force, these components contribute massively to the total force in the system. It is suspected that these connector forces are induced by the drag force. The drag force is affected by the velocity, which varies during the simulations. Therefore, the force might get a relatively large difference between each time step. Which results in higher frequency components, that further affect the connector force.

For both the simulations and the experimental data, it is expected that the eigenfrequencies of the system will affect the forces and motions of the system. By performing an MDOF analysis of the system, an undamped and uncoupled eigenperiod for Case 4 could be obtained. The eigenperiods have been calculated for the different connector stiffness with respect to surge. The is set to be the same as in the simulation. The resulting eigenperiods are presented in Table 6.1.

Table 6.1: Analytical calculated eigenperiods for Case 4

	S1	S2	S3	S4	Unit
$T_{n,1}$	19.34	19.41	19.91	21.52	[s]
$T_{n,2}$	6.51	6.80	8.35	10.73	[s]
$T_{n,3}$	3.75	3.95	5.13	7.29	[s]
$T_{n,4}$	2.78	2.94	3.87	5.67	[s]
$T_{n,5}$	2.38	2.52	3.34	5.07	[s]

From the table, it is observed that the lower periods in Figure 6.21, are close to some of the eigenperiods calculated with the MDOF method. A review of the presented surge motions, it will be observed that some of the peaks in surge response coincide with these eigenperiods. It is strongly believed that these eigenfrequencies affect the connector force and are the main reason for the lower periods observed.

6.8 Introduction of Control Logic

Based on the results from the experiments and the simulations, a control logic has been proposed. The task is to change to an optimal stiffness, for a given sea state. Here the logic uses the results from the validations cases in surge. The forces in the x-directions are another choice, or even the pitch and the heave motion could be used. However, with the connector used in this experiment, there was little effect on the heave and pitch motions. With a more complex logic, the best connection stiffness could have been decided by a weighing function between the forces and surge motion.

Here, the control logic is limited to Case 2, with wave steepness $\epsilon = 1/80$. The waves are also only propagating in the x-direction, so the motion in sway, roll, and yaw is not further investigated at this stage. In the future, there should be a large focus on the correlation between multiple modules and networks with 2x2 size or even 10x10. The surge, heave, and pitch motion, combined with the connection force, is examined to determine which stiffness best suits the different wave periods.

6.8.1 Switching Logic

To control the module's motion, it is necessary to know when to switch and what to switch to. Therefore, the surge motion of the two modules in Case 2 has been compared Figure 6.23a. The solid line presents Module 1, while Module 2 is the dashed line. At the wave periods before 4.5 seconds, the behavior is very similar for the two modules. After the peak at 4.5 seconds, the second module maintains a large response for increasing wave periods. At the same time, the first module decreases first before it increases afterward. This means Module 1 benefits from the softer spring. With the other springs, they move with the same response. The Connection Force presented in Figure 6.23b, is similar to the response for surge. Before 3.5 seconds, the force is less with softer connections, while after 3.5 seconds, it gets the opposite. F20 is a good choice between 3.5 and 4.5 seconds, while the two stiffest, F10 and F11, are more suitable for larger periods.

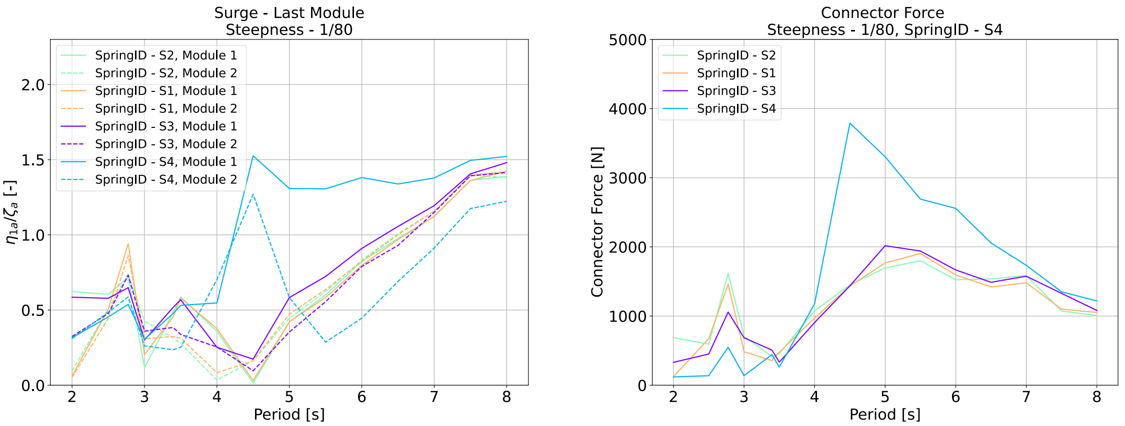

(a) RAO comparison between Module 1 and Module 2 in Case 2.

(b) RAO of Connection Force between Module 1 and Module 2 in Case 2.

Figure 6.23: RAO of surge and Connection Force for Module 1 and Module 2 in Case 2.

Choosing the most suitable connection stiffness would be more straightforward, depending on the force. However, for the motions, the response could, as explained, be the opposite for the two modules. For example, choosing a stiffness based on Module 1s surge motion would give higher motions for Module 2 and higher connection force between them. At the lower periods, below 4 seconds, the force slightly exceeds 1500 N in the worst case. The study on finding control logic is constrained by the limited experimental testing results, as only four spring stiffnesses were tested. An extensive study on finding the most optimal stiffness using the simulator has been proposed by Sølvberg (2023) in his Master Thesis. However, even by finding the optimal stiffness, it is not guaranteed always to benefit the response in the surge, heave, and pitch while reducing the forces in the connections.

To check if the switching works, a new simulation with the control logic implemented was performed. Using the surge RAO of Module 2, the best stiffness is found dependent on the wave period. The simulation had an initial wave period of 7.5 seconds, and after 600 seconds it was changed to a wave period of 3.5 seconds. Every 25 seconds, the control logic stores the surge motions. By applying an FFT on the signal, it determined the signal's period. If the last two checks have the same period, it is assumed that the wave period has changed and is stabilized. The result of this process is presented in Figure 6.24. Where a time series of the two modules' surge motion is presented with and without the control logic. It also shows a time series of the connector force and its active stiffness. After 600 seconds, the changing wave period is evident, and the control switches the stiffness after 820 seconds, leading to reduced motion.

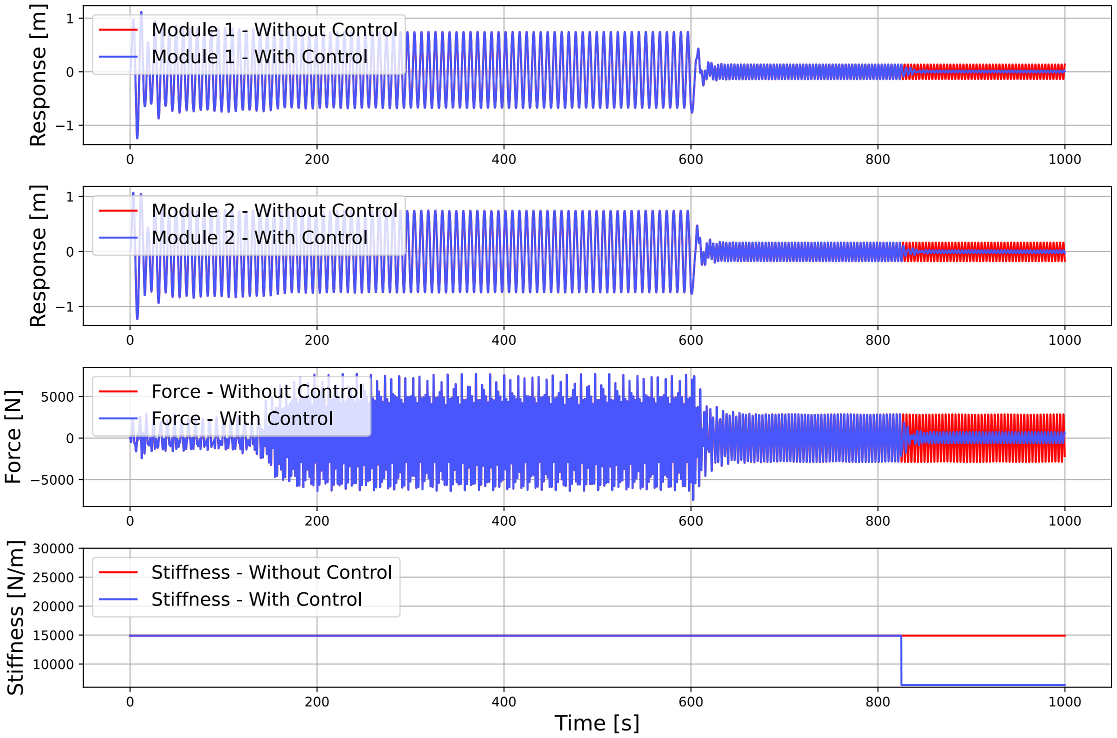

Figure 6.24: Comparison between when the control logic is active and when it's not.

Chapter 7

Conclusion and Further Work

7.1 Conclusion

In this thesis, the goal has been to evaluate if different connector stiffness could affect the response of a multi-module structure. To figure this out, a numerical model was developed to simulate the response. Further, was an experiment conducted, to obtain data on the module's motion with flexible connectors. This was done by using four different springs with different stiffness. Based on the results obtained, it appears that adjusting the stiffness can impact the motion of the module.

The four different spring stiffnesses were also used in the numerical model. The response obtained from the simulations was compared with the experimental data. Results show that the simulator is capable to simulate the same behavior as was observed in the experiment. Although the response is generally reliable, there are some issues with overestimation. Additionally, it was observed that there is a consistent difference between the connector force in the simulation and the experiment. It is believed that tuning could improve the accuracy of the results. However, there were proven to be some unwanted high-frequency force components, that cannot be neglected without further investigation.

The experiment has been proven to give valuable information for further development of both the simulator and future experiments. The knowledge about what range the connector's stiffness should operate in was not known before. The starting point in the simulator was way off, which was anyhow hard to know beforehand. The results have proven that different connector stiffness affects the module's motion and force in the connector. This means an adaptive controller should be developed depending on the sea states.

An example of a control logic that switches between different stiffnesses based on the wave period is presented. The results show that by changing to the more optimal stiffness, the module's motion, and connector force improves.

7.2 Further Work

7.2.1 Further Work for Experiment

The data retrieved from the experiment gave valuable data that could be used to improve the simulator and knowledge about multi-modular structures. In future work, several improvements could be performed. The connector in this thesis was developed under a tight schedule, leading to multiple improvements. In future experiments, creating a base on the modules to which the connector can be attached is recommended. A rigid base to connect the connector to will decrease the uncertainties if the modules are not aligned.

Next, a connector with vertical stiffness components can further reduce the heave and pitch response. Further, possibly using a load cell that measures the load cell in three axes would benefit the results.

In this thesis, only regular wave tests were performed. To analyze the behavior of the connectors and the effects the stiffness has on the motions, an irregular wave test would give valuable data. The wavemaker in Lilletanken also limited the regular waves, so extensive wave tests should be performed with higher wave periods. Further testing where the modules expand in two directions, such as 2x2 and 3x3 grids. This would provide valuable data that could be compared with the simulations. Here it is also recommended to perform wave tests with different wave headings on the incoming waves. This does also demand that a connector is developed to handle force in multiple directions.

Finally, it should be noted that the mooring system used in the experiment had certain limitations due to the scaling and equipment available. Additionally, some of the eigenfrequencies were found to be in the same range as the incoming wave frequency, which is not considered to be ideal. An extensive study to optimize the mooring system should be performed, as it is believed the mooring system has a big impact on the modules. In future experiments, the possibility of Cable-Driven Parallel Robots (CDPR) should be explored. By using the CDPR, it becomes feasible to numerically implement a mooring system with precise application of forces and moments.

7.2.2 Further Work for Simulator

In this thesis the idea of a control logic is introduced, and an example is shown to exemplify how it could work. However, the simulator needs improvement to conduct such sea-state changes properly. It is also suggested that the best stiffness should depend on multiple factors, and not just the surge response of one module. This would probably demand that the factors are weighted with respect to the most critical factor.

As the simulator is now, only regular waves can be used. To improve the simulator, it should be able to perform irregular waves as well. Combining this with the control logic, it would be possible to get an idea of how well a multi-modular system could behave. To improve the responses of the simulator, damping should be added. As for now potential theory is used, where viscous damping is neglected.

Bibliography

Bachynski, E., Kristiansen, T., Larsen, C. & Myrhaug, D. (2019), *TMR 4182 Marine dynamics*, Department of Marine Technology at NTNU.

Bar-Eli, K. (1984), ‘Coupling of chemical oscillators’, *J. Phys. Chem.* **88**, 3616–3622.

Bishop, J. (n.d.), ‘7.2.2-odes: Stiff systems’. Last visited 2022-11-25.
URL: *https://www.youtube.com/watch?v=KS_6mxdzQws&ab_channel=JacobBishop*

Butcher, J. (n.d.), ‘Explicit runge-kutta methods’. Last visited 2022-12-11.
URL: *https://en.wikipedia.org/wiki/Runge%E2%80%93Kutta_methods#Explicit_Runge.E2.80.93Kutta_methods*

Chen, X., Li, S. & Xu, Y. (2020), ‘Connectors of vlfs’, *Encyclopedia of Ocean Engineering* pp. 1–7.

Ding, R., Zhang, H., Liu, C., Xu, D., Shi, Q., Liu, J., Zou, W. & Wu, Y. (2022), ‘Connector configuration effect on the dynamic characteristics of multi-modular floating structure’, *Journal of Ocean Engineering and Science* .
URL: *https://www.sciencedirect.com/science/article/pii/S2468013322002352*

Fu, S., Moan, T., Chen, X. & Cui, W. (2007), ‘Hydroelastic analysis of flexible floating interconnected structures’, *Ocean Engineering* **34**, 1516–1531.

Hespanha, J. P., Liberzon, D. & Morse, A. (2003), ‘Hysteresis-based switching algorithms for supervisory control of uncertain systems’, *Automatica* **39**(2), 263–272.
URL: *https://www.sciencedirect.com/science/article/pii/S0005109802002418*

Jiang, D., Tan, K., Wang, C. & Dai, J. (2021), ‘Research and development in connector systems for very large floating structures’, *Ocean Engineering* **88**, 1–22.

Lamas Pardo, M., Iglesias, G. & Carral, L. (2015), ‘A review of very large floating structures (vlfs) for coastal and offshore uses’, *Ocean Engineering* **Volume 109**, 675 – 690.

Lincoln, B. & Armstrong, E. (1934), ‘Floating airports’.
URL: *https://web.archive.org/web/20090522010353/http://blog.modernmechanix.com/2008/03/30/float*
airports-on-link-continents/

Offshore-Energy (n.d.), ‘Solarduck’s offshore floating solar array aces lir notf tests’. Last visited 2022-11-04.
URL: *https://www.offshore-energy.biz/solarducks-offshore-floating-solar-array-aces-lir-notf-tests/*

Onsrud, M. (2019), ‘An experimental study on the wave-induced vertical response of an articulated multi-module floating solar island’, MasterThesis.

Pedersen, E. & Engja, H. (2014), ‘Mathematical modelling and simulation of physical systems/lecture notes in tmr4275’.

Pettersen, B. (2020), *Marin teknikk 3 - Hydrodynamikk*, Akademika.

Reiten, H. (2022), 'Two-dimensional numerical and experimental investigation of hydrodynamic forces and wake interaction between two or more square cylinders in large-amplitude oscillatory flow', MasterThesis.

Riggs, H., Ertekin, R. & Mills, T. (1999), 'Impact of stiffness on the response of a multimodule mobile offshore base', *International Journal of Offshore and Polar Engineering* **9**, 126–133.

Shi, Q., Zhang, H., Xu, D., Qi, E., Tian, C., Ding, J., Wu, Y., Lu, Y. & Li, Z. (2018), 'Experimental validation of network modeling method on a three-modular floating platform model', *Coastal Engineering* **137**, 92–102.
URL: *https://www.sciencedirect.com/science/article/pii/S0378383917302429*

Steen, S. (2014), 'Experimental methods in marine hydrodynamics'. Lecture notes in TMR18.

Suzuki, H. (2005), 'Overview of megafloat: Concept, design criteria, analysis, and design', *Marine Structures* **18**(2), 111–132. Very Large Floating Structures.
URL: *https://www.sciencedirect.com/science/article/pii/S0951833905000407*

Suzuki, H., Riggs, H., Fujikubo, M., Shugar, T., Seto, H., Yasuzawa, Y., Bhattacharya, B., Hudson, D. & Shin, H. (2007), 'Very large floating structures', *Proceedings of the International Conference on Offshore Mechanics and Arctic Engineering - OMAE* **2**, paper OMAE2007–29758.

Sølvberg, S. (2023), 'Optimal design of connectors for floating multi-modular strucures - an application for floating solar energy harvest', Master Thesis.

Sørensen, A. (2018), 'Marine cybernetics/lecture notes'.

Xia, S., Qi, E., Xu, D., Hu, J. & Wu, Y. (2016), 'On retaining a multi-module floating structure in an amplitude death state', *Ocean Engineering* **121**, 134–142.

Xia, S., Zhang, H., Wen, Y. & Xu, D. (2022), 'Vibration control of multi-modular vlfs in random sea based on stiffness-adjustable connectors', *Applied Sciences* **12**, 1–21.

Xu, D. L., Zhang, H. C., C, L., Qi, E. R., Hu, J. J. & Wu, Y. S. (2014), *On Study of Nonlinear Network Dynamics of Flexibly Connected Multi-Module Very Large Floating Structures*, pp. 1805–1814.
URL: *https://ascelibrary.org/doi/abs/10.1061/9780784413609.181*

Xu, D., Zhang, H. C., Xia, S., Lu, C., Qi, E., Tian, C. & Wu, Y. (2015), 'Nonlinear network modeling of multi-module floating structures with arbitrary flexible connections', *Journal of Fluids and Structures* **59**, 270–284.

Zhang, H., Xu, D., Lu, C., Qi, E., Hu, J. & Wu, Y. (2014), 'Amplitude death of a multi-module floating airport', *Nonlinear Dynamics* **79**.

Zhang, H., Xu, D., Lu, C., Xia, S., Qi, E., Hu, J. & Wu, Y. (2015), 'Network dynamic stability of floating airport based on amplitude death', *Ocean Engineering* **104**, 129–139.
URL: *https://www.sciencedirect.com/science/article/pii/S0029801815001845*

Appendix

Experimental Connectors

StiffnessID	Model scale stiffness tension [N/m]	Model scale stiffness compression [N/m]	Full-scale stiffness tension [N/m]	Full-scale stiffness compression [N/m]	Length [mm]	Position
F10.1	66.31	80.05	26524	32020	60.1	Left: 1 and 2
F10.2	66.32	81.72	26528	32688	60.3	Right: 1 and 2
F10.3	65.53	81.75	26212	32700	58.5	Left: 2 and 3
F10.4	65.7	68.64	26280	27456	60.6	Right: 2 and 3
F10.5	65.91	80.56	26364	32224	62.2	Left: 3 and 4
F10.6	66.13	86.44	26452	34576	61.2	Right: 3 and 4
F10.7	63.87	68.18	25548	27272	63.4	Left: 4 and 5
F10.8	65.4	78.78	26160	31512	63.7	Right: 4 and 5
Average	**65.65**	**78.27**	**26259**	**31306**	**61.25**	
F11.1	71.65	78.56	28660	31424	68.8	Left: 1 and 2
F11.2	72.07	85.1	28828	34040	61.9	Left: 4 and 5
F11.3	76.2	84.17	30480	33668	67.3	Left: 3 and 4
F11.4	74.09	69.36	29636	27744	63	Right: 3 and 4
F11.5	72.31	79.02	28924	31608	68.6	Right: 1 and 2
F11.6	73.09	67.41	29236	26964	65.4	Right: 2 and 3
F11.7	73.77	68.944	29508	27577.6	63.3	Left: 2 and 3
F11.8	73.45	74.31	29380	29724	69.3	Right: 4 and 5
Average	**73.33**	**75.86**	**29332**	**30344**	**66.0**	
F20.1	37.19	52.09	14876	20836	67	Right: 2 and 3
F20.2	37.39	63.97	14956	25588	61.7	Left: 4 and 5
F20.3	37.41	49.77	14964	19908	63.1	Right: 1 and 2
F20.4	37.46	48.09	14984	19236	63.1	Left: 1 and 2
F20.5	37.55	61.29	15020	24516	67	Left: 2 and 3
F20.6	37.78	53.21	15112	21284	65	Right: 4 and 5
F20.7	36.42	48.24	14568	19296	68.3	Right: 3 and 4
F20.8	36.77	61.5	14708	24600	67	Left: 3 and 4
Average	**37.25**	**54.77**	**14899**	**21908**	**65.3**	
F31.2	15.66	15.53	6264	6212	67.3	Right: 1 and 2
F31.3	15.77	18.83	6308	7532	70.7	
F31.4	15.61	16.55	6244	6620	67.8	Left: 1 and 2
F31.6	16.07	16.43	6428	6572	63.5	Right: 2 and 3
F31.7	16.21	15.64	6484	6256	65	Left: 2 and 3
F31.8	16.36	17.16	6544	6864	62.2	Left: 4 and 5
F31.9	16.79	17.24	6716	6896	61	Right: 4 and 5
F31.10	15.73	16.62	6292	6648	61.9	Right: 3 and 4
F31.11	15.37	17.09	6148	6836	67	Left: 3 and 4
Average	**15.95**	**16.79**	**6381**	**6715**	**65.2**	

StiffnessID	Model scale stiffness tension [N/m]	Model scale stiffness compression [N/m]	Full-scale stiffness tension [N/m]	Full-scale stiffness compression [N/m]	Length [mm]	Position

Table 1: Full overview of produced springs and their corresponding length, compression, and tension stiffness.

Experiment Test Results

C Sway Results

First Module Response

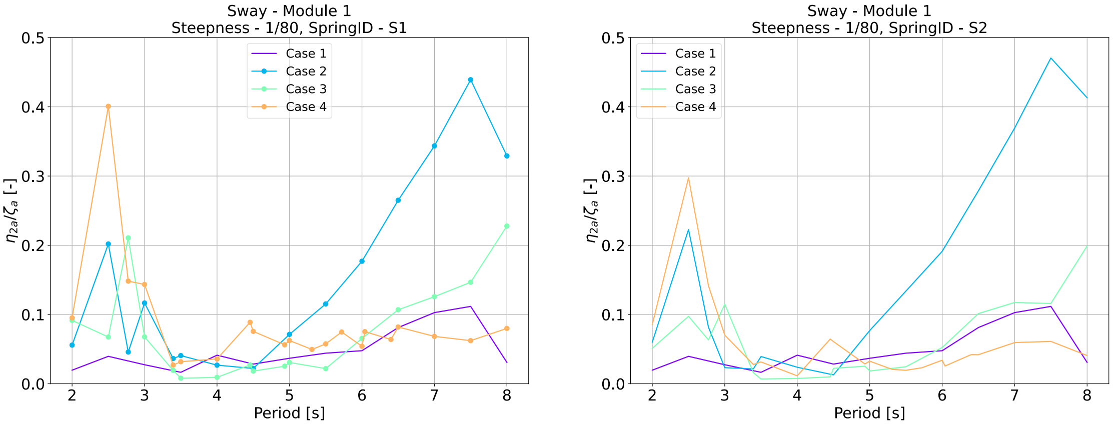

(a) RAO in sway for the first module with wave steepness $\epsilon = 1/80$, SpringID S1 for all cases, except Case 1

(b) RAO in sway for the first module with wave steepness $\epsilon = 1/80$, SpringID S2 for all cases, except Case 1

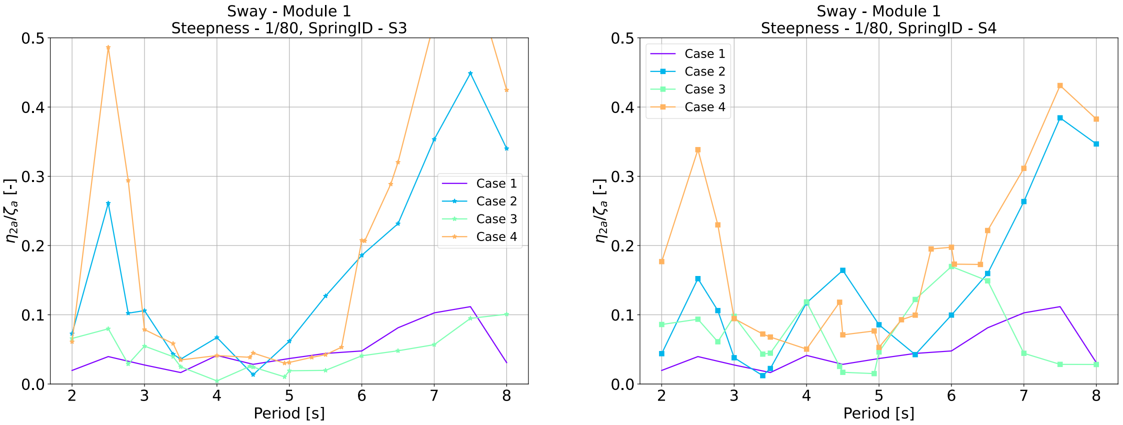

(c) RAO in sway for the first module with wave steepness $\epsilon = 1/80$, SpringID S3 for all cases, except Case 1

(d) RAO in sway for the first module with wave steepness $\epsilon = 1/80$, SpringID S4 for all cases, except Case 1

Figure 1: RAO in sway

Middle Modules Response

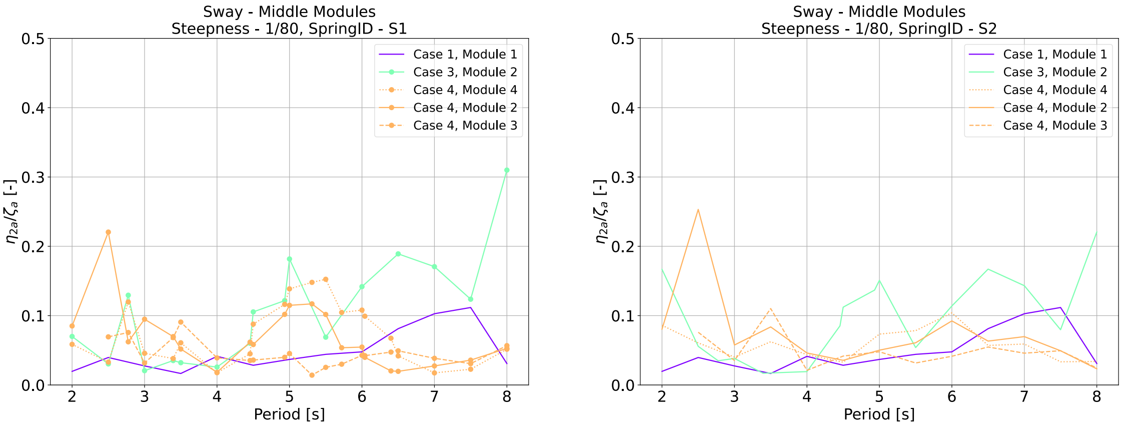

(a) RAO in sway for the middle modules with wave steepness $\epsilon = 1/80$, SpringID S1 for all cases, except Case 1

(b) RAO in sway for the middle modules with wave steepness $\epsilon = 1/80$, SpringID S2 for all cases, except Case 1

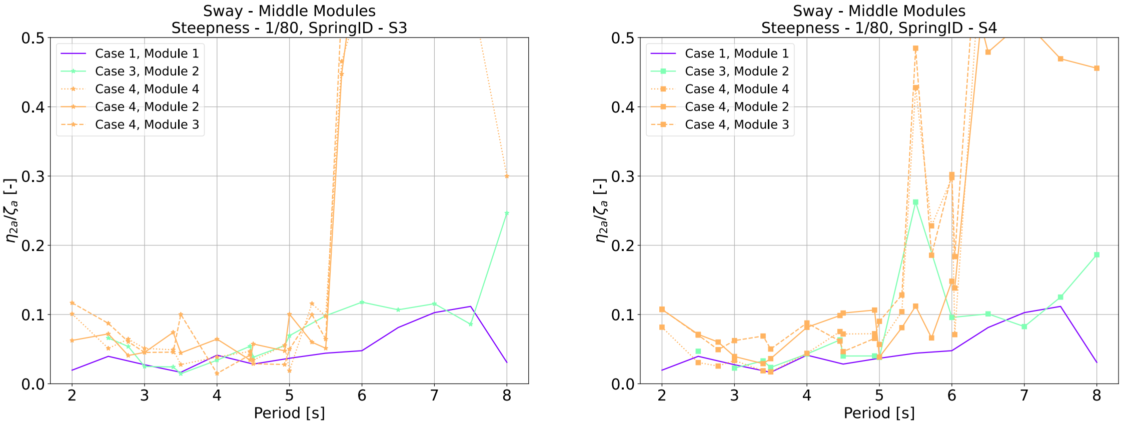

(c) RAO in sway for the middle modules with wave steepness $\epsilon = 1/80$, SpringID S3 for all cases, except Case 1

(d) RAO in sway for the middle modules with wave steepness $\epsilon = 1/80$, SpringID S4 for all cases, except Case 1

Figure 2: RAO in sway

Last Module Response

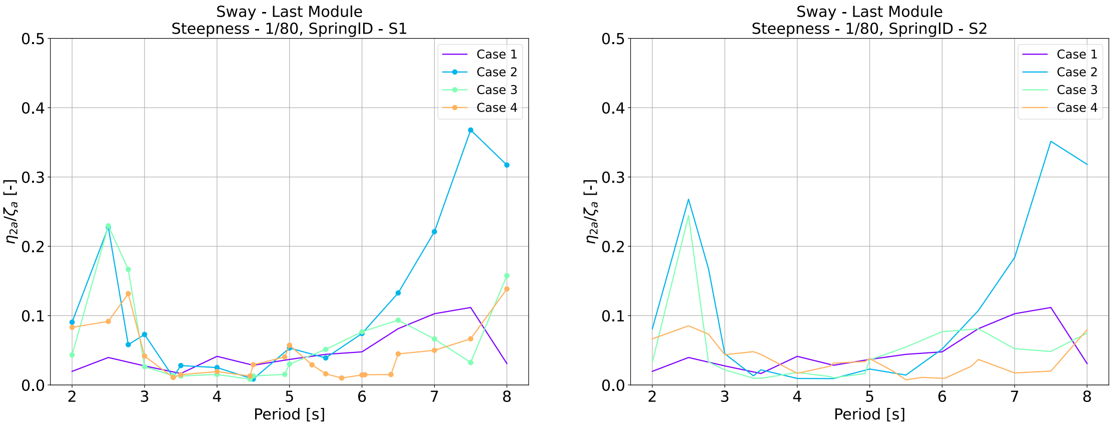

(a) RAO in sway for the last module with wave steepness $\epsilon = 1/80$, SpringID S1 for all cases, except Case 1

(b) RAO in sway for the last module with wave steepness $\epsilon = 1/80$, SpringID S2 for all cases, except Case 1

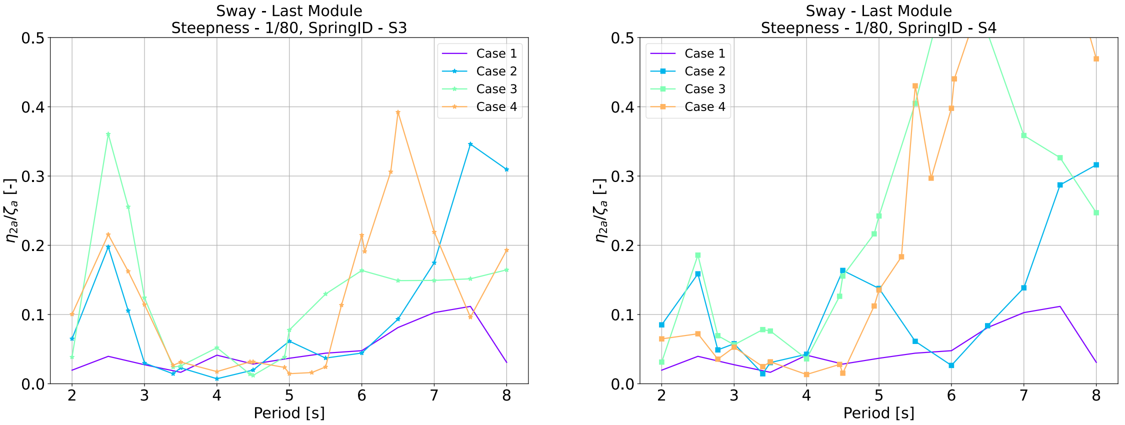

(c) RAO in sway for the last module with wave steepness $\epsilon = 1/80$, SpringID S3 for all cases, except Case 1

(d) RAO in sway for the last module with wave steepness $\epsilon = 1/80$, SpringID S4 for all cases, except Case 1

Figure 3: RAO in sway for the last module in Case 1, 2, 3, and 4.

D Heave Results

First Module Response

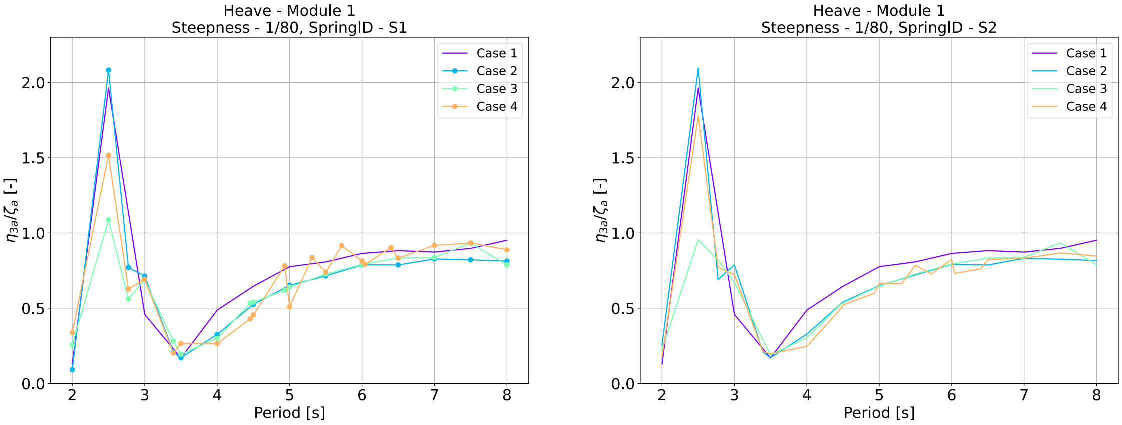

(a) RAO in heave for the first module with wave steepness $\epsilon = 1/80$, SpringID S1 for all cases, except Case 1

(b) RAO in heave for the first module with wave steepness $\epsilon = 1/80$, SpringID S2 for all cases, except Case 1

Figure 4: RAO in Heave

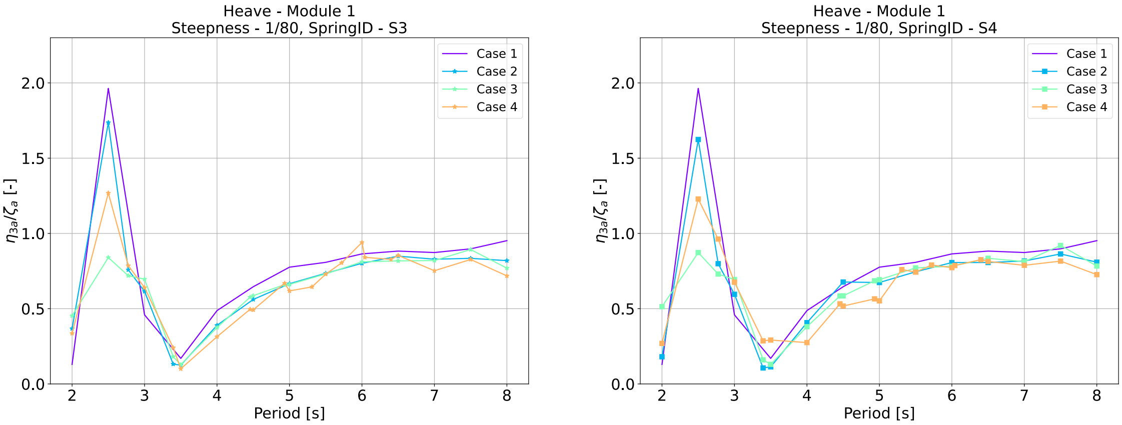

(c) RAO in heave for the first module with wave steepness $\epsilon = 1/80$, SpringID S3 for all cases, except Case 1

(d) RAO in heave for the first module with wave steepness $\epsilon = 1/80$, SpringID S4 for all cases, except Case 1

Figure 4: RAO in Heave

Middle Modules Response

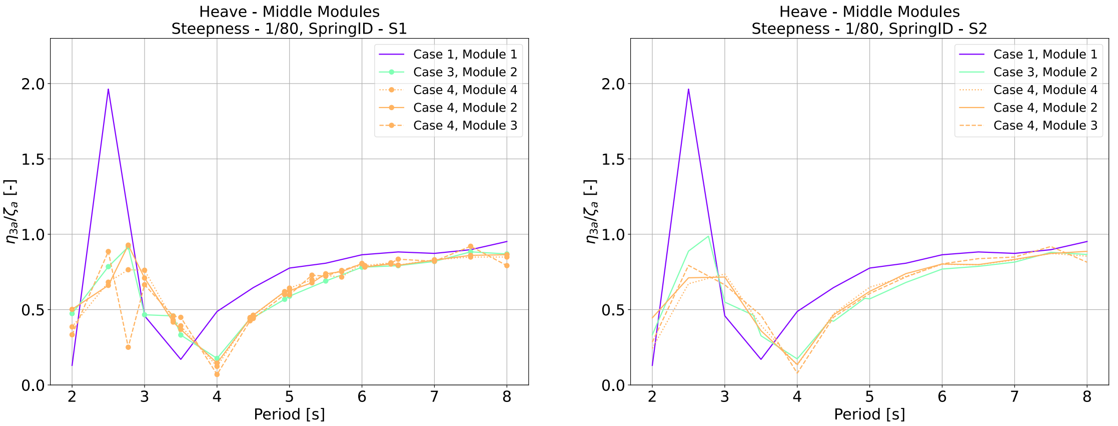

(a) RAO in heave for the middle modules with wave steepness $\epsilon = 1/80$, SpringID S1 for all cases, except Case 1

(b) RAO in heave for the middle modules with wave steepness $\epsilon = 1/80$, SpringID S2 for all cases, except Case 1

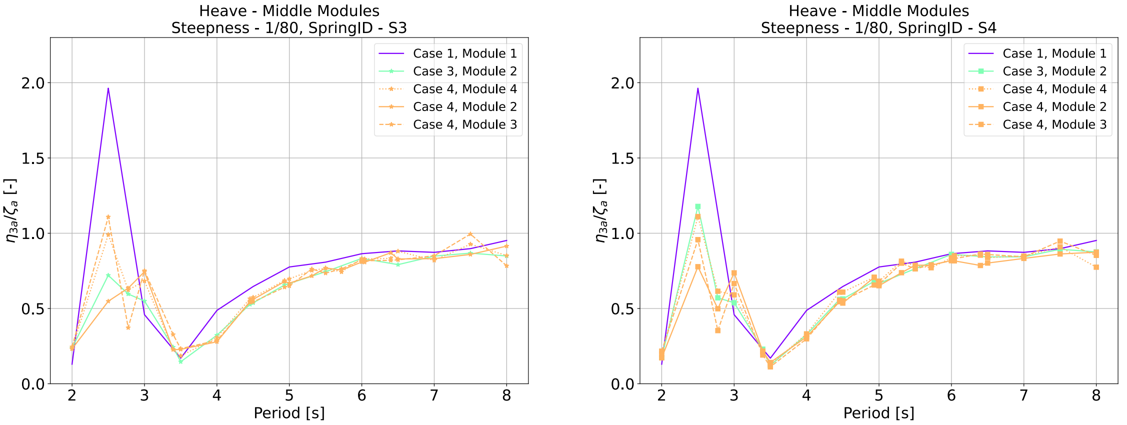

(c) RAO in heave for the middle modules with wave steepness $\epsilon = 1/80$, SpringID S3 for all cases, except Case 1

(d) RAO in heave for the middle modules with wave steepness $\epsilon = 1/80$, SpringID S4 for all cases, except Case 1

Figure 5: RAO in Heave

Last Module Response

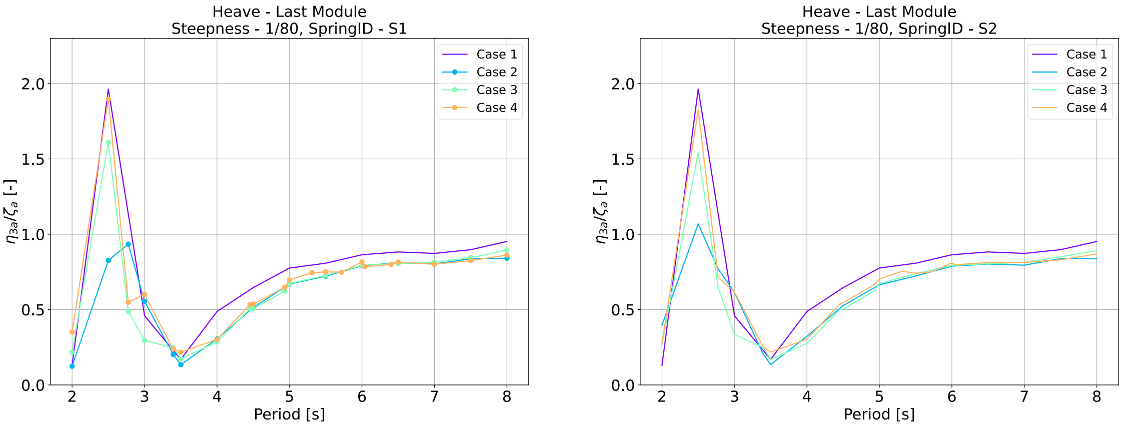

(a) RAO in heave for the last module with wave steepness $\epsilon = 1/80$, SpringID S1 for all cases, except Case 1

(b) RAO in heave for the middle modules with wave steepness $\epsilon = 1/80$, SpringID S2 for all cases, except Case 1

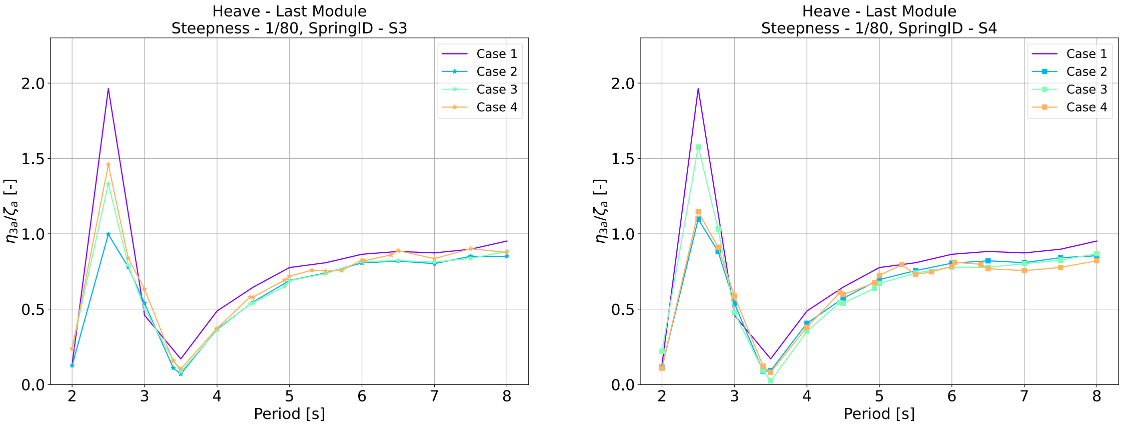

(c) RAO in heave for the middle modules with wave steepness $\epsilon = 1/80$, SpringID S3 for all cases, except Case 1

(d) RAO in heave for the middle modules with wave steepness $\epsilon = 1/80$, SpringID S4 for all cases, except Case 1

Figure 6: RAO in Heave

E Roll Results

First Module Response

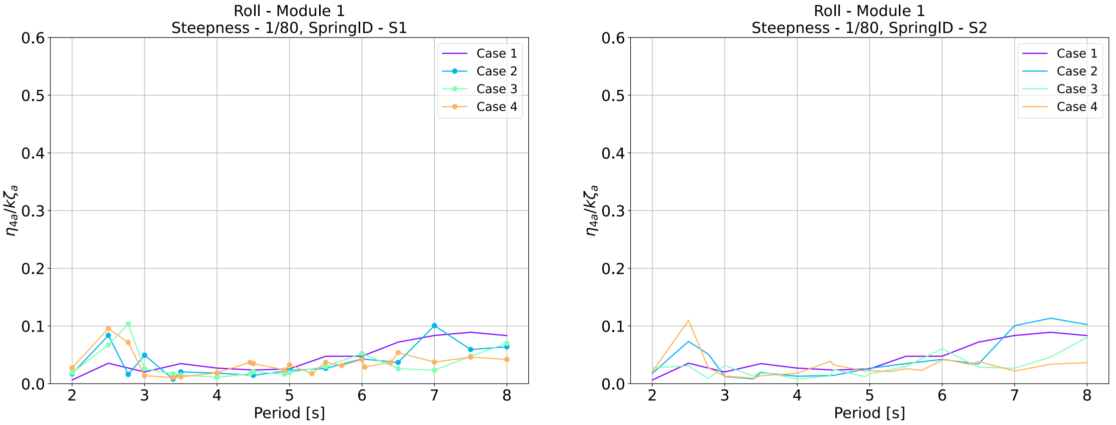

(a) RAO in roll for the first module with wave steepness ϵ = 1/80, SpringID S1 for all cases, except Case 1

(b) RAO in roll for the first module with wave steepness ϵ = 1/80, SpringID S2 for all cases, except Case 1

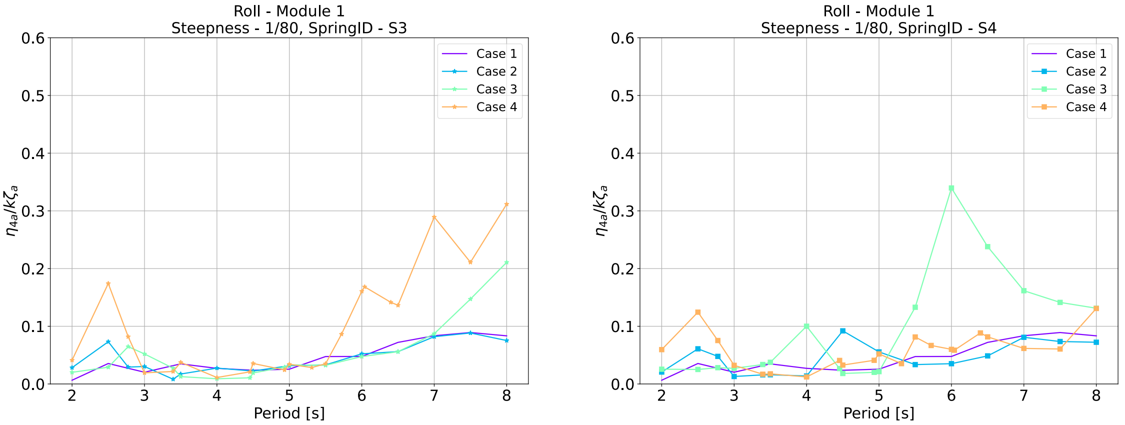

(c) RAO in roll for the first module with wave steepness ϵ = 1/80, SpringID S3 for all cases, except Case 1

(d) RAO in roll for the first module with wave steepness ϵ = 1/80, SpringID S4 for all cases, except Case 1

Figure 7: RAO in roll

Middle Modules Response

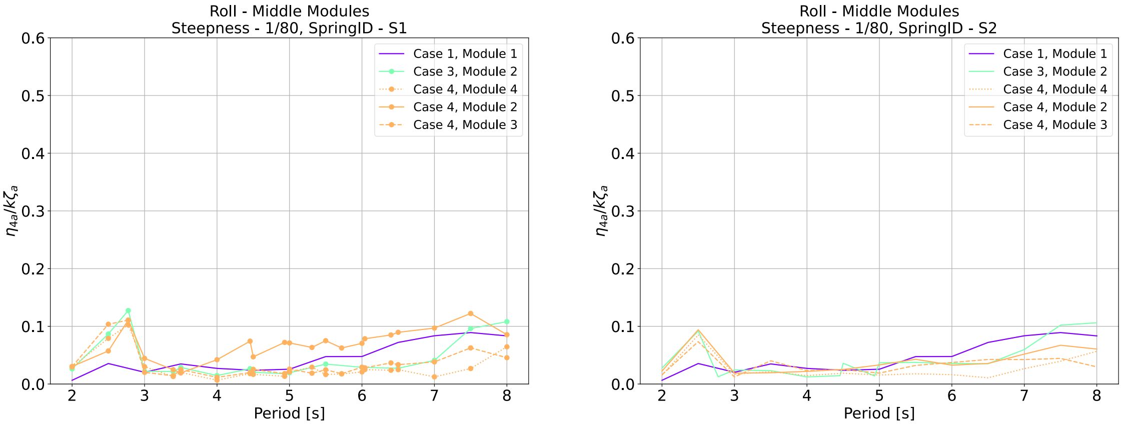

(a) RAO in roll for the middle modules with wave steepness $\epsilon = 1/80$, SpringID S1 for all cases, except Case 1

(b) RAO in roll for the middle modules with wave steepness $\epsilon = 1/80$, SpringID S2 for all cases, except Case 1

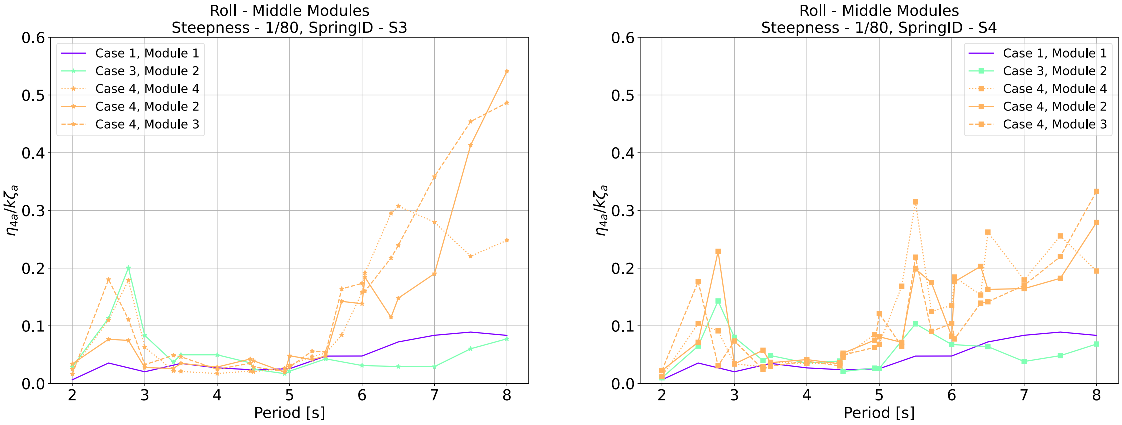

(c) RAO in roll for the middle modules with wave steepness $\epsilon = 1/80$, SpringID S3 for all cases, except Case 1

(d) RAO in roll for the middle modules with wave steepness $\epsilon = 1/80$, SpringID S4 for all cases, except Case 1

Figure 8: RAO in roll

Last Module Response

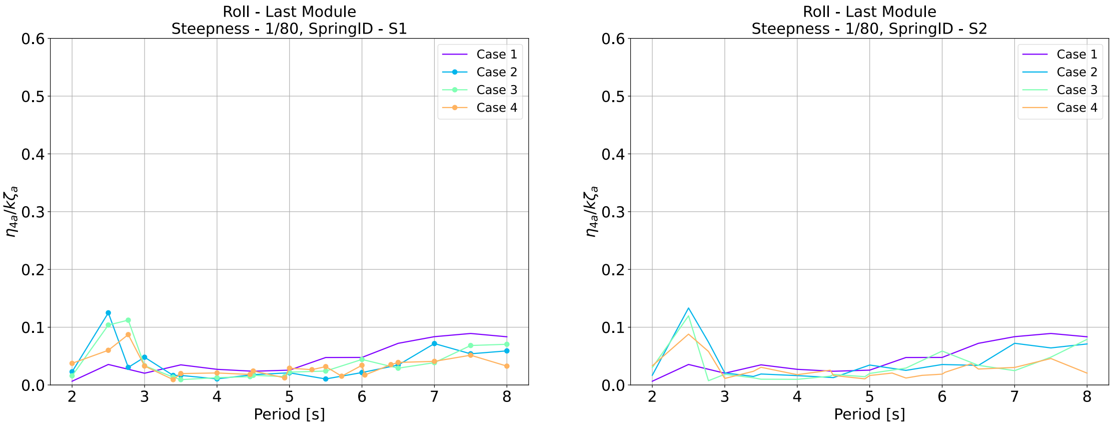

(a) RAO in roll for the last module with wave steepness $\epsilon = 1/80$, SpringID S1 for all cases, except Case 1

(b) RAO in roll for the last module with wave steepness $\epsilon = 1/80$, SpringID S2 for all cases, except Case 1

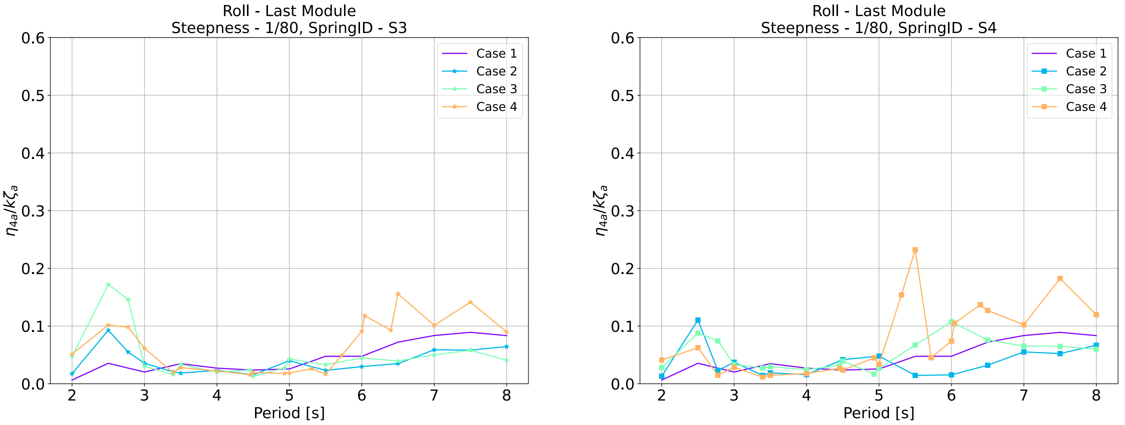

(c) RAO in roll for the last module with wave steepness $\epsilon = 1/80$, SpringID S3 for all cases, except Case 1

(d) RAO in roll for the last module with wave steepness $\epsilon = 1/80$, SpringID S4 for all cases, except Case 1

Figure 9: RAO in roll for the last module in Case 1, 2, 3, and 4.

F Pitch Results

First Module Response

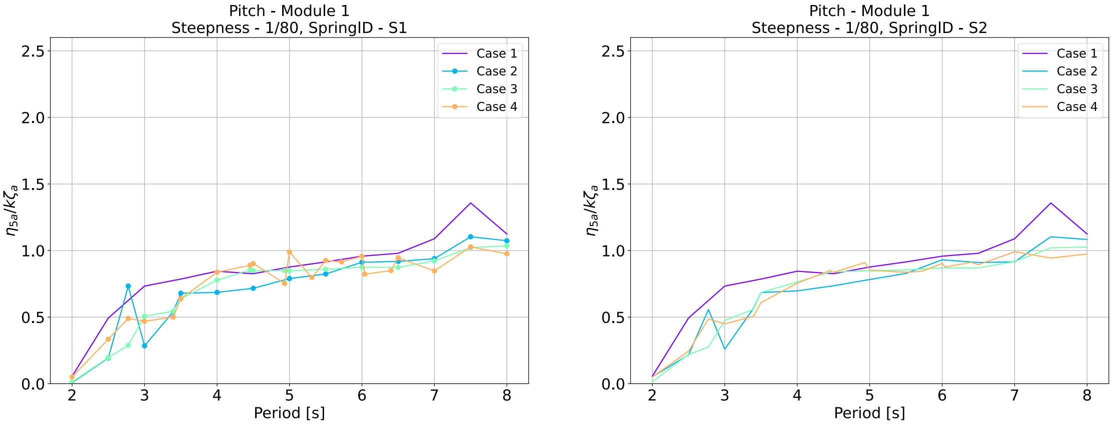

(a) RAO in pitch for the first module with wave steepness $\epsilon = 1/80$, SpringID S1 for all cases, except Case 1

(b) RAO in pitch for the first module with wave steepness $\epsilon = 1/80$, SpringID S2 for all cases, except Case 1

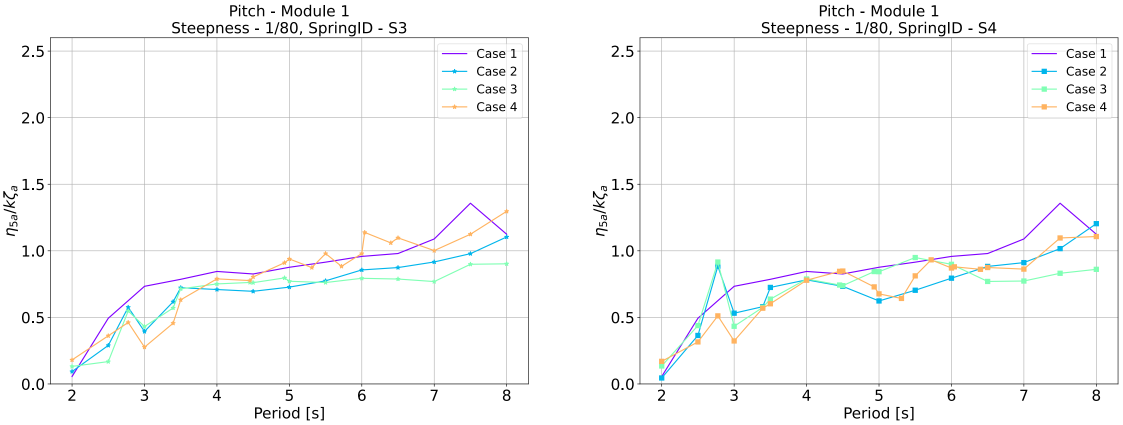

(c) RAO in pitch for the first module with wave steepness $\epsilon = 1/80$, SpringID S3 for all cases, except Case 1

(d) RAO in pitch for the first module with wave steepness $\epsilon = 1/80$, SpringID S4 for all cases, except Case 1

Figure 10: RAO in Pitch

Middle Modules Response

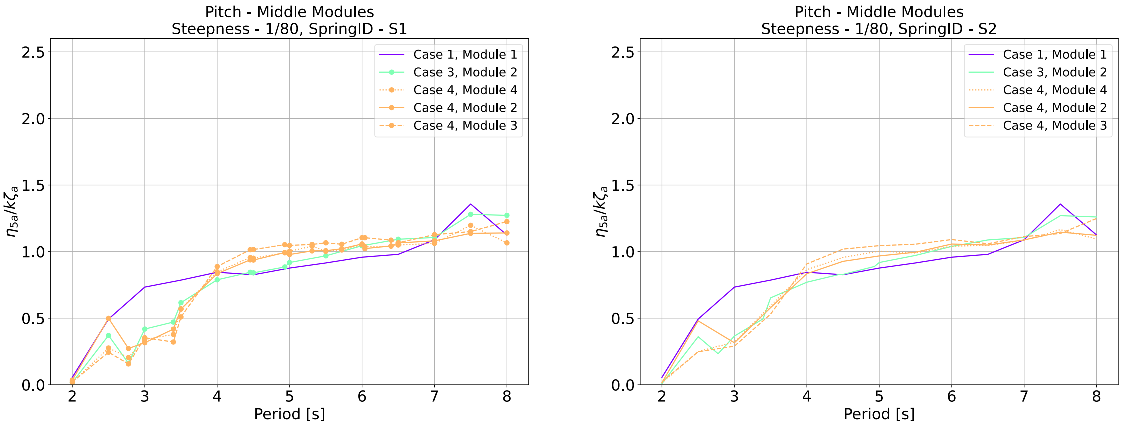

(a) RAO in pitch for the middle modules with wave steepness $\epsilon = 1/80$, SpringID S1 for all cases, except Case 1

(b) RAO in pitch for the middle modules with wave steepness $\epsilon = 1/80$, SpringID S2 for all cases, except Case 1

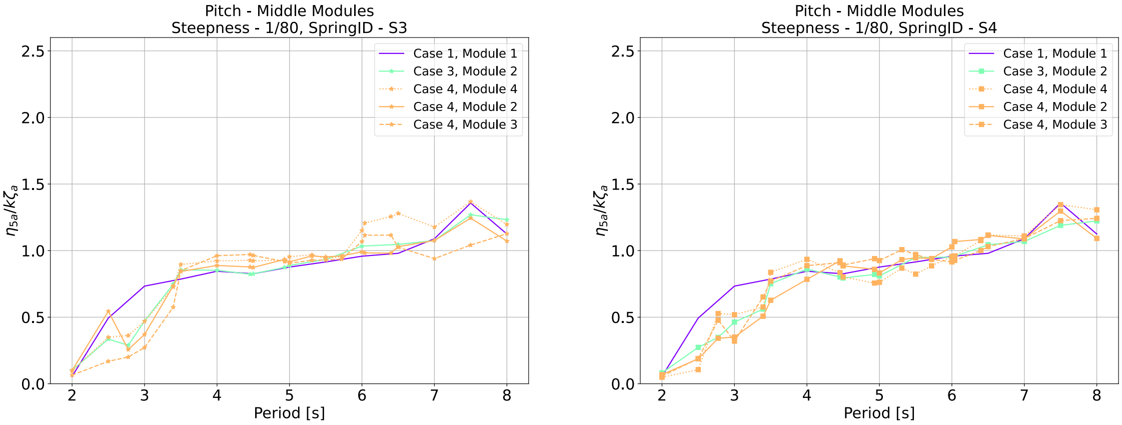

(c) RAO in pitch for the middle modules with wave steepness $\epsilon = 1/80$, SpringID S3 for all cases, except Case 1

(d) RAO in pitch for the middle modules with wave steepness $\epsilon = 1/80$, SpringID S4 for all cases, except Case 1

Figure 11: RAO in Pitch

Last Module Response

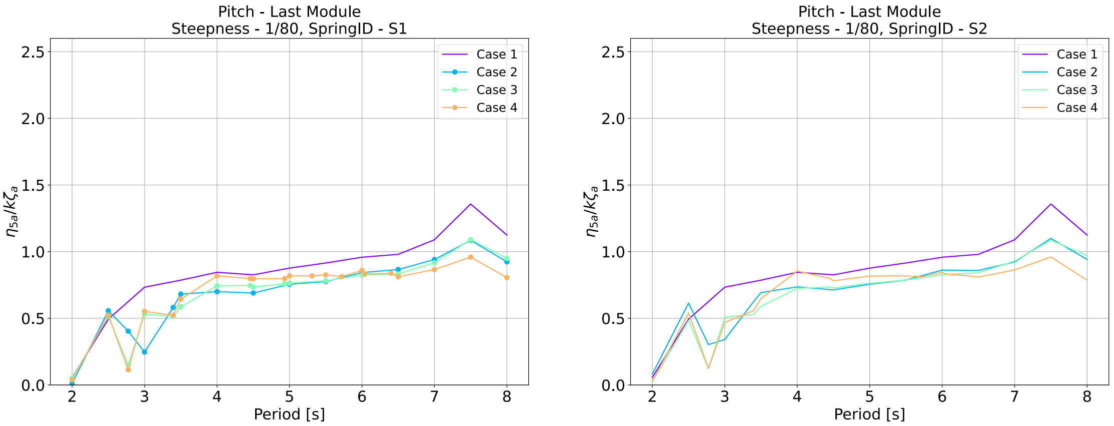

(a) RAO in pitch for the last module with wave steepness $\epsilon = 1/80$, SpringID S1 for all cases, except Case 1

(b) RAO in pitch for the last module with wave steepness $\epsilon = 1/80$, SpringID S2 for all cases, except Case 1

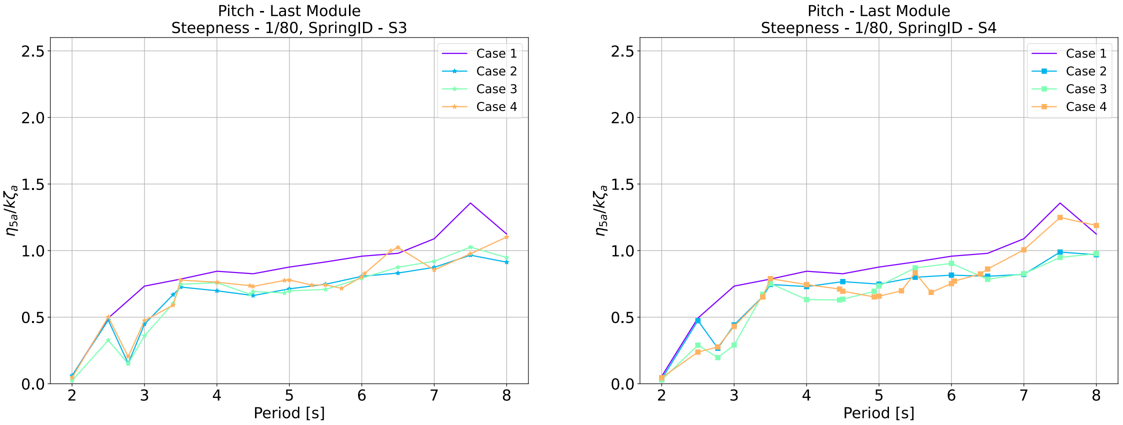

(c) RAO in pitch for the last module with wave steepness $\epsilon = 1/80$, SpringID S3 for all cases, except Case 1

(d) RAO in pitch for the last module with wave steepness $\epsilon = 1/80$, SpringID S4 for all cases, except Case 1

Figure 12: RAO in Pitch for the last module in Case 1, 2, 3, and 4.

G Yaw Results

First Module Response

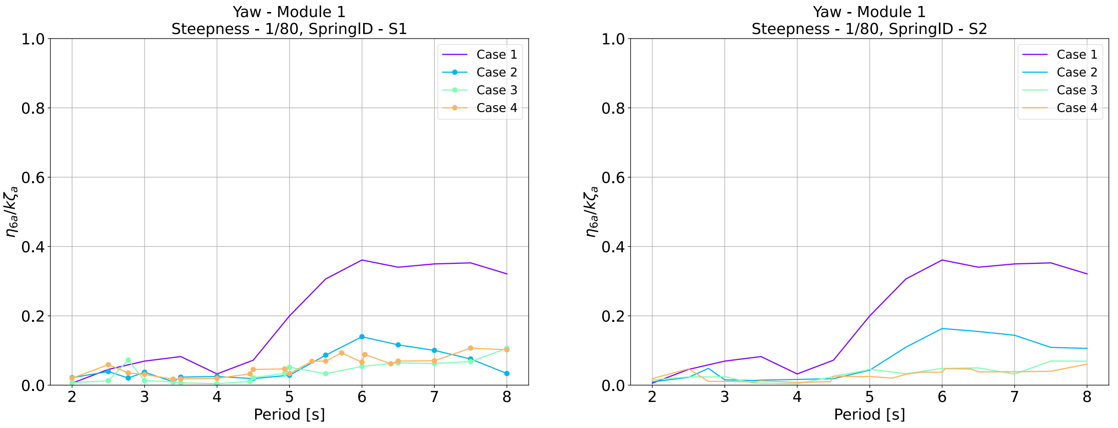

(a) RAO in yaw for the first module with wave steepness $\epsilon = 1/80$, SpringID S1 for all cases, except Case 1

(b) RAO in yaw for the first module with wave steepness $\epsilon = 1/80$, SpringID S2 for all cases, except Case 1

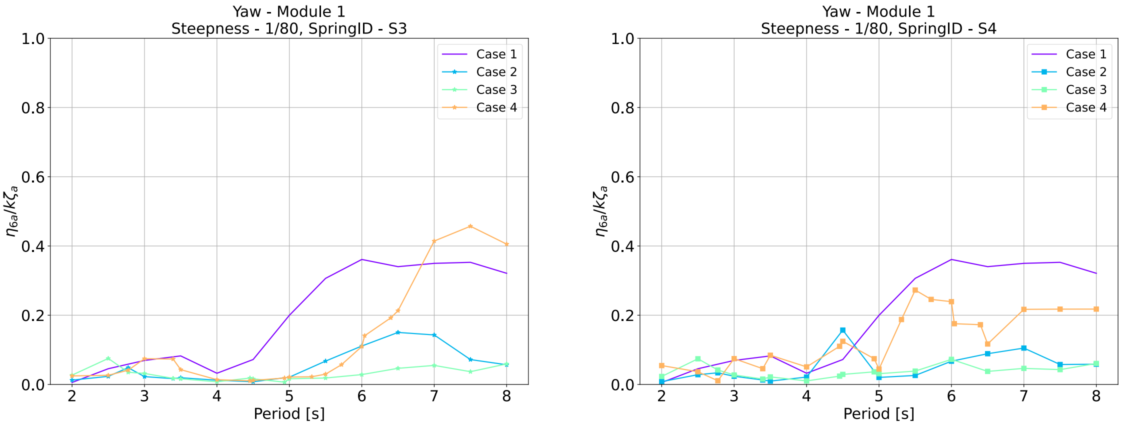

(c) RAO in yaw for the first module with wave steepness $\epsilon = 1/80$, SpringID S3 for all cases, except Case 1

(d) RAO in yaw for the first module with wave steepness $\epsilon = 1/80$, SpringID S4 for all cases, except Case 1

Figure 13: RAO in yaw

Middle Modules Response

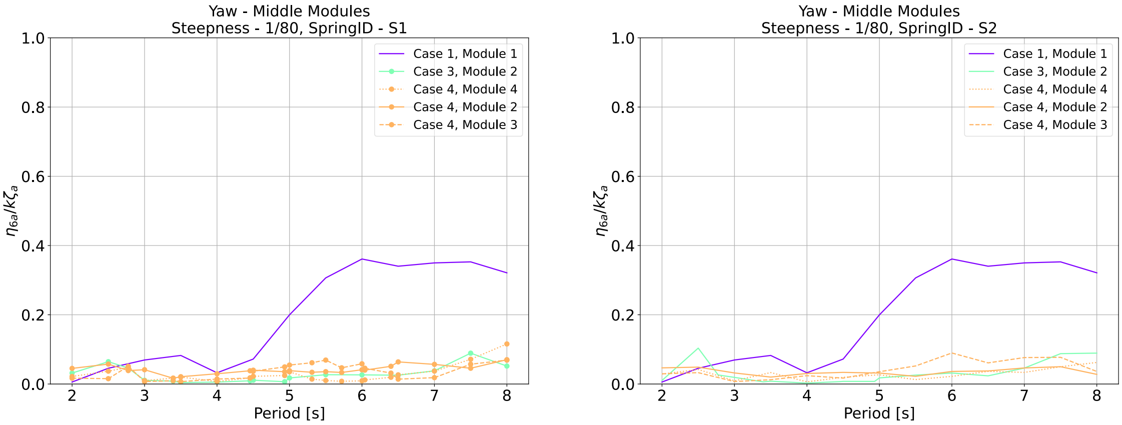

(a) RAO in yaw for the middle modules with wave steepness $\epsilon = 1/80$, SpringID S1 for all cases, except Case 1

(b) RAO in yaw for the middle modules with wave steepness $\epsilon = 1/80$, SpringID S2 for all cases, except Case 1

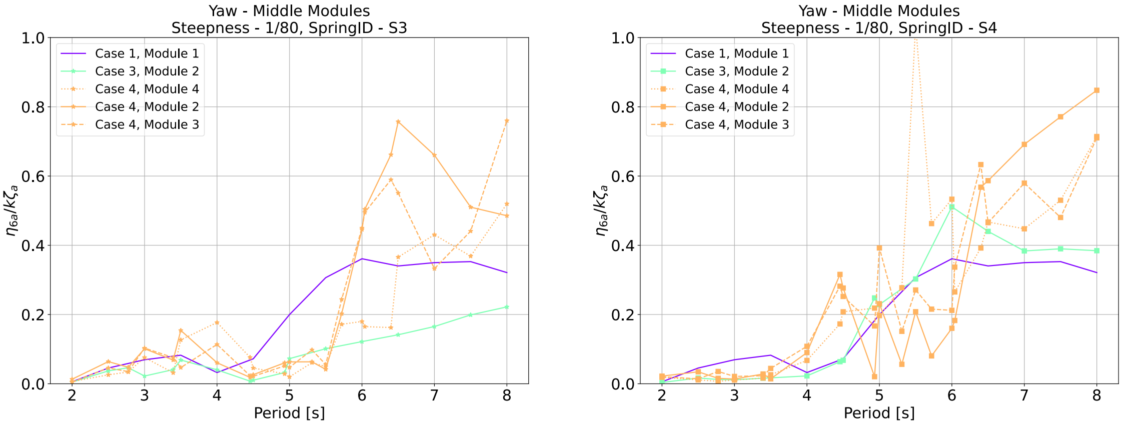

(c) RAO in yaw for the middle modules with wave steepness $\epsilon = 1/80$, SpringID S3 for all cases, except Case 1

(d) RAO in yaw for the middle modules with wave steepness $\epsilon = 1/80$, SpringID S4 for all cases, except Case 1

Figure 14: RAO in yaw

Last Module Response

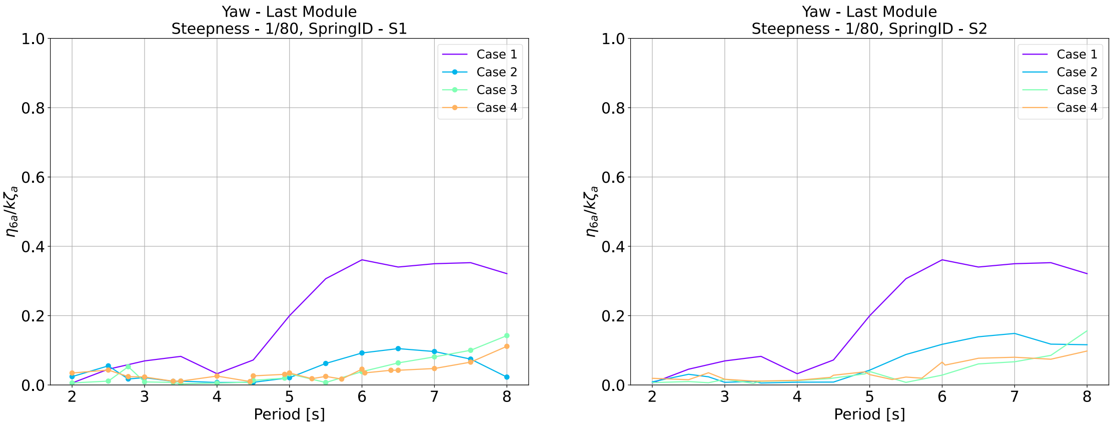

(a) RAO in yaw for the last module with wave steepness $\epsilon = 1/80$, SpringID S1 for all cases, except Case 1

(b) RAO in yaw for the last module with wave steepness $\epsilon = 1/80$, SpringID S2 for all cases, except Case 1

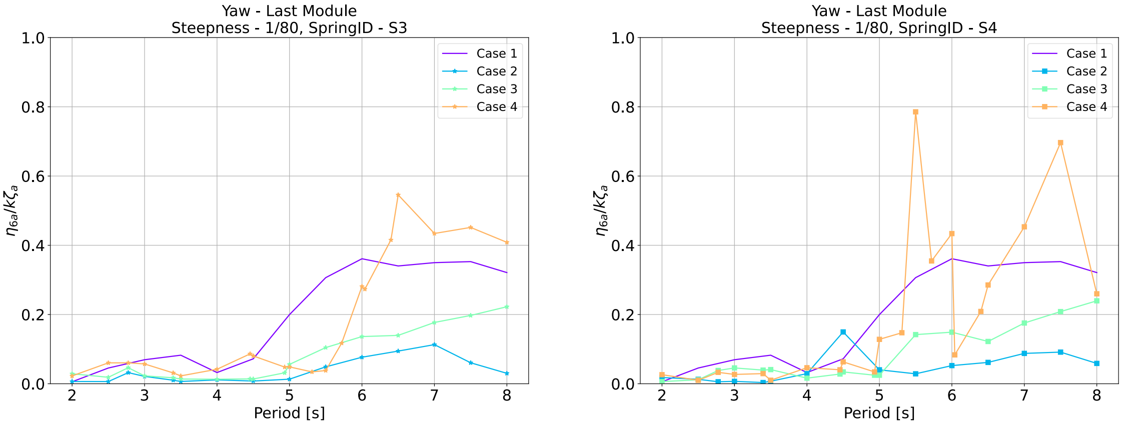

(c) RAO in yaw for the last module with wave steepness $\epsilon = 1/80$, SpringID S3 for all cases, except Case 1

(d) RAO in yaw for the last module with wave steepness $\epsilon = 1/80$, SpringID S4 for all cases, except Case 1

Figure 15: RAO in yaw for the last module in Case 1, 2, 3, and 4.

Pitch Validation for Case 3 and 4

H Pitch for Case 3

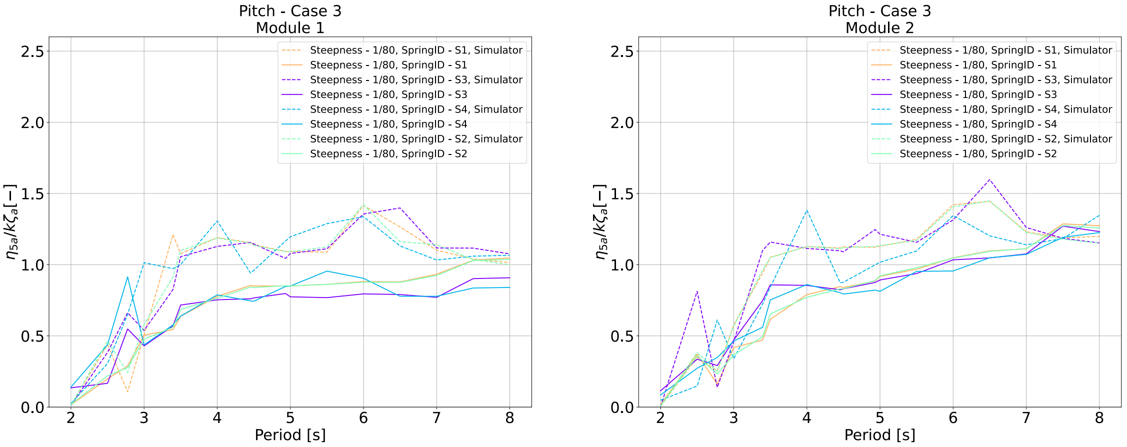

(a) RAO in pitch for Module 1 (b) RAO in pitch for Module 2

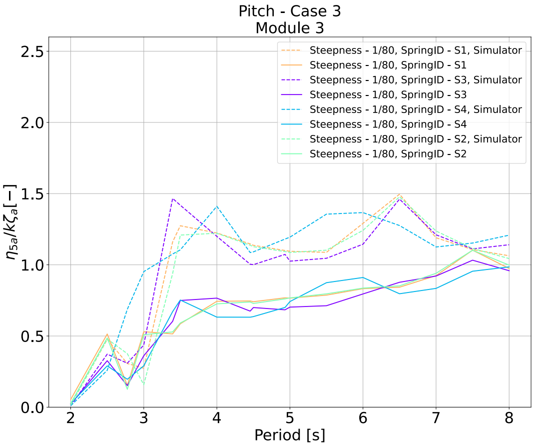

(c) RAO in pitch for Module 3

Figure 16: Pitch results for Case 3

I Pitch for Case 4

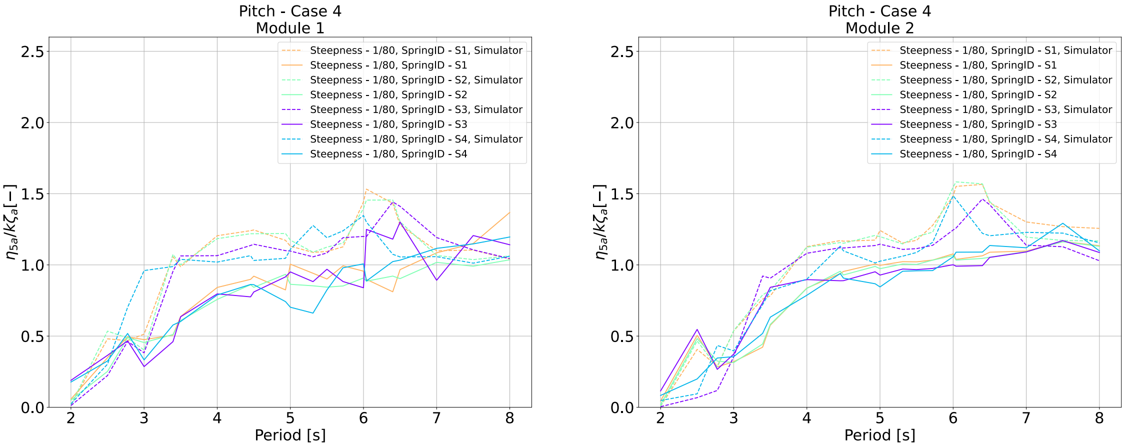

(a) RAO in pitch for Module 1

(b) RAO in pitch for Module 2

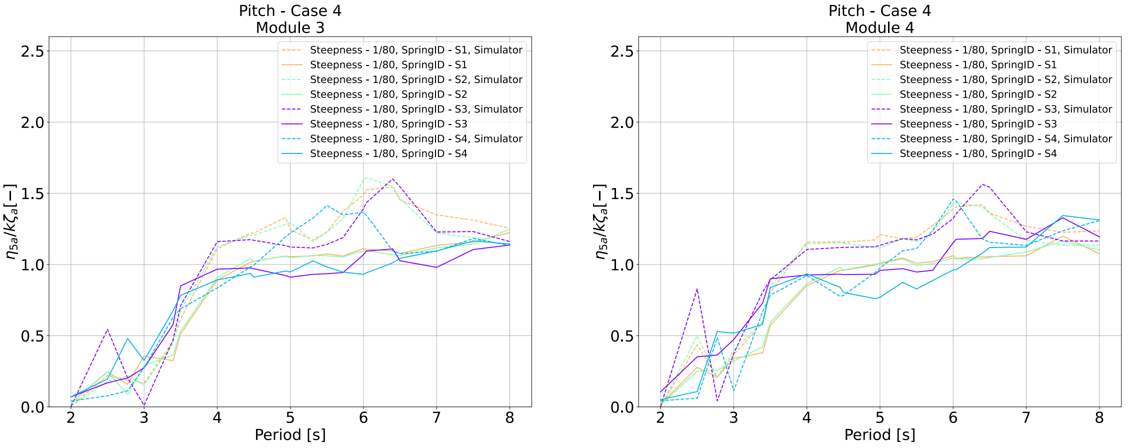

(c) RAO in pitch for Module 3

(d) RAO in pitch for Module 5

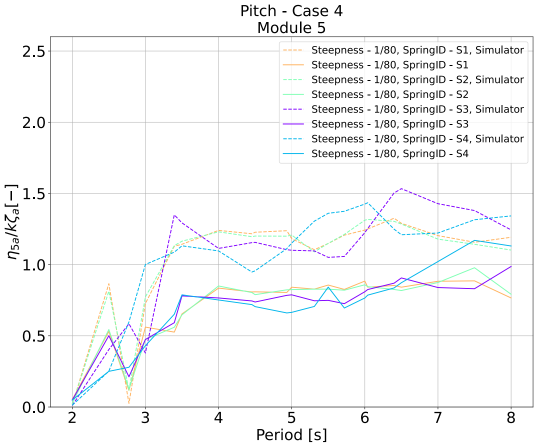

(e) RAO in pitch for Module 5

Figure 17: Pitch results for Case 4

NTNU

Norwegian University of
Science and Technology